

WL-TR-92-2105

AD-A262 747

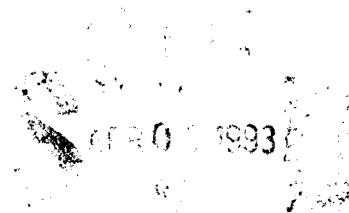


ADVANCED THERMALLY-STABLE, COAL-DERIVED, JET
FUELS DEVELOPMENT PROGRAM ANNUAL REPORT
EXPERIMENT SYSTEM AND MODEL DEVELOPMENT



Elmer Klavetter
Steve Martin
Wayne Trott
Tim O'Hern
Gerald Nelson
David Tallant

Sandia National Laboratories
Albuquerque, NM 87185



February 1993

ANNUAL REPORT FOR THE PERIOD JULY 1991 - SEPTEMBER 1992

APPROVED FOR PUBLIC RELEASE; DISTRIBUTION IS UNLIMITED

AERO PROPULSION AND POWER DIRECTORATE
WRIGHT LABORATORY
AIR FORCE MATERIEL COMMAND
WRIGHT-PATTERSON, AFB OH 45433-7103

93 4 05 078

93-07102

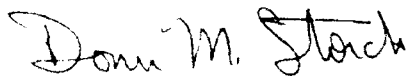


Notice

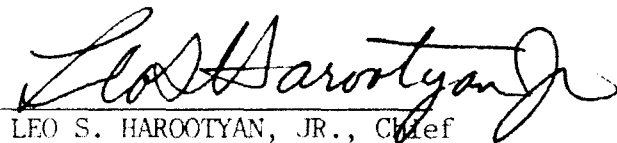
When Government drawings, specifications, or other data are used for any purpose other than in connection with a definitely Government-related procurement, the United States Government incurs no responsibility or any obligation whatsoever. The fact that the government may have formulated or in any way supplied the said drawings, specifications, or other data, is not to be regarded by implication, or otherwise in any manner construed, as licensing the holder, or any other person or corporation; or as conveying any rights or permission to manufacture, use, or sell any patented invention that may in any way be related thereto.

This report is releasable to the National Technical Information Service (NTIS). At NTIS, it will be available to the general public, including foreign nations.

This technical report has been reviewed and is approved for publication.



DONN M. STORCH, Major, USAF
Program Manager
Fuels and Lubrication Division
Aero Propulsion and Power Directorate



LEO S. HAROOTYAN, JR., Chief
Fuels and Lubrication Division
Aero Propulsion and Power Directorate

If your address has changed, if you wish to be removed from our mailing list, or if the addressee is no longer employed by your organization please notify WL/POS, WPAFB, OH 45433-7103 to help us maintain a current mailing list.

Copies of this report should not be returned unless return is required by security considerations, contractual obligations, or notice on a specified document.

REPORT DOCUMENTATION PAGE			Form Approved OMB No. 0704-0188	
<small>1. This report is the property of the U.S. Government and is loaned to your organization; it and its contents are not to be distributed outside your organization. 2. This report is not to be reproduced, stored in a retrieval system, or transmitted, in any form or by any means, electronic, mechanical, photocopying, recording, or by any information storage and retrieval system, without the prior written permission of the U.S. Government. 3. This report is not to be used for advertising or promotional purposes, for creating new collective works, or for resale.</small>				
1. AGENCY USE ONLY (Leave blank)	2. REPORT DATE February 1993	3. REPORT TYPE AND DATES COVERED Interim-July 91-Sept. 92		
4. TITLE AND SUBTITLE Advanced Thermally-Stable, Coal-Derived Jet Fuels Development Program Annual Report Experiment System and Model Development			5. FUNDING NUMBERS C:M1PRFY1455-91N-0638 PE: 62203F PR: 3048 TA: 05 WU: 87	
6. AUTHOR(S) Sandia National Laboratories Albuquerque, NM 87185				
7. PERFORMING ORGANIZATION NAME(S) AND ADDRESS(ES) Donn Storch, Major, USAF AERO Propulsion & Power Directorate Wright Laboratory Wright Patterson AFB OH 45433-6563			8. PERFORMING ORGANIZATION REPORT NUMBER WL-TR-92-2105	
9. SPONSORING/MONITORING AGENCY NAME(S) AND ADDRESS(ES)			10. SPONSORING/MONITORING AGENCY REPORT NUMBER	
11. SUPPLEMENTARY NOTES				
12a. DISTRIBUTION AVAILABILITY STATEMENT Approved for public release; distribution is unlimited.			12b. DISTRIBUTION CODE	
13. ABSTRACT (Maximum 200 words) A program entitled "Thermally-Stable Jet Fuels Development" was initiated in FY89 by the U.S. Air Force, Aero Propulsion and Power Directorate, working jointly with the Department of Energy, Pittsburgh Energy Technology Center. Thermal stability of aviation fuels is of concern because of the potential operation problems arising from fuel degradation under thermal stress conditions. Sandia National Laboratories has been conducting efforts to develop instrumentation for monitoring characteristics of jet fuel degradation and solids deposition and develop models of those mechanisms from the data acquired using that instrumentation. This report describes the instrumentation development, data acquisition, and model parameter determination. Analysis of solid deposits is also described.				
14. SUBJECT TERMS Degradation, Instrumentation, Laser Diagnostics, Mass Sensor, Particle Formation			15. NUMBER OF PAGES	
			16. PRICE CODE	
17. SECURITY CLASSIFICATION OF REPORT UNCLASSIFIED	18. SECURITY CLASSIFICATION OF THIS PAGE UNCLASSIFIED	19. SECURITY CLASSIFICATION OF ABSTRACT UNCLASSIFIED	20. LIMITATION OF ABSTRACT UC	

LIST OF FIGURES

	<u>Page</u>
1. Arrhenius plot yielding activation energies for two different samples of JP-8 fuel.	4
2. Measured viscosity values from the QCM system compared with literature values for a JP-8 fuel.	6
3. Schematic of the second-generation QCM system.	7
4. Schematic of the QCM system stainless-steel test fixture to contain the quartz crystal microbalance suspended in a jet fuel sample.	8
5. Control panel layout for the QCM data acquisition programs in a IBM-compatible Windows operating environment.	11
6. Typical data acquired by the QCM system on mass accumulation versus time; data showed for JP-8 degradation at 180°C with a 50 psi oxygen overpressure.	13
7. Arrhenius plot for JP-8 fuel, 50 psi oxygen overpressure, using the second-generation QCM system.	15
8. Schematic layout of PCS system for studies of heated jet fuels.	17
9. Measured correlation function for four Jet A-1 samples heated to different temperatures. PCS was performed at room temperature. The correlation is weak for the sample heated to 120°C, but becomes well-defined as samples are taken to higher temperatures. The sample time per channel for the 120°C sample was 3×10^{-5} seconds; for the other samples the sample time per channel was 1×10^{-4} seconds.	18
10. Temperature measurements at various points in the 3.8 cm quartz cube during heating of Jet A-1 fuel. Thermocouple locations are noted on legend.	21
11. Temperature measurements at various points in the 3.8 cm quartz cube during heating of Jet A-1 fuel with new temperature controller. Thermocouple locations are noted on legend.	22

LIST OF FIGURES (cont.)

	<u>Page</u>
12. Mie intensity parameters versus scattering angle for HeNe laser source and particle diameters corresponding to available polystyrene standard spheres. Asterisks represent experimentally determined intensities normalized to the calculated value at a scattering angle of 90 degrees.	25
13. Mie intensity parameters versus scattering angle for Argon ion laser source and particle diameters corresponding to available polystyrene standard spheres.	26
14. Measured particle size distributions for three Jet A-1 samples heated to different temperatures. PCS was performed at room temperature. Particle size distributions determined using CONTIN analysis routine.	28
15. Real-time measurements of particle size distributions during 150°C heating of Jet A-1. Particle size distributions determined using CONTIN analysis routine.	29
16. Real-time measurements of mean particle size during 160°C heating of Jet A-1. Particle size determined using CONTIN analysis routine.	32
17. Scattering intensity (normalized to the maximum value) as a function of test time for Jet A-1 samples heated to 150°C and 160°C.	33
18. Calculated scattering intensity (at 90° scattering angle) as a function of particle diameter for various particle refractive indices. Illuminating wavelength is 632.8 nm. Computations made using modified version of the program CALLBH (Bohren and Huffman, 1983).	34
19. Mean particle diameter (as determined by PCS) versus thermal stress temperature. Solid triangles represent data obtained in quartz sample cell. Solid circles correspond to data obtained in cylindrical test cell. Vertical bars indicate the width (one standard deviation) of the particle size distribution as determined by the CONTIN analysis routine.	36
20. Optical photographs of the phase transition region from a) 9/91-2; b) 9/91-9; and c) 9/91-6.	39
21. Solids deposit in an afterburner augmenter arm.	40

LIST OF FIGURES (cont.)

	<u>Page</u>
22. Typical wall temperature and carbon profile along a test tube.	41
23. Sulfur peak height plotted as a function of distance along test tubes a) 9/91-6 and b) 9/91-2. The wall temperature is shown for comparison.	42
24. SEM and SEM/EDA spectra from the phase transition region of tube 9/91-2 (low sulfur fuel, 18-hour test).	44
25. SEM and SEM/EDA spectra from the phase transition region of tube 9/91-6 (high sulfur fuel, 18-hour test).	45
26. SEM and SEM/EDA spectra from the high temperature (1000°F) region of tube 9/91-6 (high sulfur fuel, 18-hour test).	46
27. SEM and SEM/EDA spectra from the phase transition region of tube 9/91-9 (high sulfur fuel, 6-hour test).	47
28. SEM and SEM/EDA spectra from the high temperature (1000°F) region of tube 9/91-9 (high sulfur fuel, 6-hour test).	48
29. Auger spectrum from the high temperature (1000°F) region of tube 9/91-6 (high sulfur fuel, 18-hour test) showing the presence of S and O in addition to C.	49
30. Plot of the S and O content as a function of position in the high temperature (1000°F) region of tube 9/91-6 (high sulfur fuel, 18-hour test).	50
31. Photograph of the deposit around an asperity in an afterburner augments.	52
32. SEM photographs of aspirates on the surface of the stainless steel tubes used in the present tests. The aspirates are Cr and Si rich.	53
33. Steady-state temperature profiles for tubes 9/91-2, 9/91-6 and 9/91-9 as provided by WPAFB.	54
34. Blue-excited (457.9nm) fluorescence spectrum, including Raman bands, at 4" along Side A of tube 9/91-2.	55

LIST OF FIGURES (cont.)

	<u>Page</u>
35. Green-excited (514.5nm) Raman-format spectrum, with background fluorescence removed, at 4" along Side A of tube 9/91-2.	56
36. Blue-excited (457.9nm) fluorescence spectra, including Raman bands, at 0" to 6" along Side A of tube 9/91-2.	58
37. Blue-excited (457.9nm) fluorescence spectra, including Raman bands, at 6" to 18" along Side A of tube 9/91-2.	59
38. Blue-excited (457.9nm) fluorescence spectra, including Raman bands, at 0" to 6" along Side A of tube 9/91-6.	60
39. Blue-excited (457.9nm) fluorescence spectra, including Raman bands, at 6" to 18" along Side A of tube 9/91-6.	61
40. Green-excited (514.5nm) fluorescence spectra, including Raman bands, at 0" to 6" along Side A of tube 9/91-9.	62
41. Steady-state wall temperatures (°F) and deposition masses (μg) as a function of distance along tube 9/91-3, as provided by WPAFB.	63
42. Green-excited (514.5nm) Raman-format spectra, with background fluorescence removed, at 0" to 6" along Side A of tube 9/91-2.	65
43. Green-excited (514.5nm) Raman-format spectra, with background fluorescence removed, at 6" to 18" along Side A of tube 9/91-2.	66
44. Green-excited (514.5nm) Raman-format spectra, with background fluorescence removed, at 0" to 6" along Side A of tube 9/91-6.	67
45. Green-excited (514.5nm) Raman-format spectra, with background fluorescence removed, at 6" to 18" along Side A of tube 9/91-6.	68
46. Green-excited (514.5nm) Raman-format spectra, with background fluorescence removed, at 0" to 6" along Side A of tube 9/91-9.	69

LIST OF FIGURES

	<u>Page</u>
47. Green-excited (514.5nm) Raman-format spectrum, with background fluorescence removed, at 8" along Side A of tube 9/91-6, showing a Raman band due to the (oxidized) tube wall at 669cm^{-1} , in addition to carbon Raman bands at 1100cm^{-1} to 1700cm^{-1} .	71
48. Green-excited (514.5nm) Raman-format spectrum, with background fluorescence removed, at 2" along Side A of tube 9/91-6, showing Raman bands due to sulfur-containing species at 288cm^{-1} and 436cm^{-1} , in addition to carbon Raman bands at 1100cm^{-1} to 1700cm^{-1} .	72
49. Green-excited (514.5nm) Raman-format spectra, with background fluorescence removed, at 12" along Side A of tubes 9/91-2 and 9/91-6, comparing carbon Raman bands deposited from a low-sulfur fuel (9/91-2) and a high-sulfur fuel (9/91-6).	73
50. Auger depth profiles of deposits on quartz microbalances after 1-1/2 hour and 4 hours, respectively.	75
51. Auger depth profiles of the deposit on a quartz microbalance for JP-8 at 200°C .	76
52. Auger depth profiles for a 500 \AA SiO_2 standard and a 550 \AA photoresist standard.	78

LIST OF TABLES

	<u>Page</u>
1. Summary of QCM Measurements of JP-8 Jet Fuel Degradation Using the Original QCM-JFTS.	3
2. Summary of QCM Measurements of Jet Fuel Degradaton Using the New QCM-JFTS.	14

FOREWORD

In May 1989, the Fuels Branch of the Aero Propulsion Directorate at Wright-Patterson Air Force Base, Ohio, commenced an investigation to develop advanced, thermally stable jet fuels as well as physical and computer models that could simulate the thermal degradation of those fuels under operational conditions. Funding was provided to the Department of Energy (DOE) Pittsburgh Energy Technology Center (PETC) to administer this effort. This report details efforts of Sandia National Laboratories (SNL), a prime contractor to DOE (DOE Contract Number DE-AC04-76DP00789). Development and testing of diagnostic instrumentation systems and analyses of jet fuel liquids and formed solids are described. Mr. William E. Harrison III was the Air Force Program Manager, Mr. Swenam Lee, Mr. Mike Baird, and Mr. Shelby Rogers were the DOE/PETC Program Managers, and Dr. Howard Stephens was the SNL Program Manager.

ACKNOWLEDGEMENTS

This Project was jointly supported by the U.S. Department of Energy, Pittsburgh Energy Technology Center (PETC) and the Aero Propulsion and Power Directorate, Wright-Patterson AFB OH. This work was supported by the U.S. Department of Energy at Sandia National Laboratories under contract DE-AC04-76DP00789. The authors wish to express their appreciation to Messrs. S. Lee, M. Baird, and S. Rogers (PETC) and Mr. W. E. Harrison III and Dr. W. M. Roquemore (Aero Propulsion and Power Directorate) for their support of this effort. The authors would also like to acknowledge H. P. Stephens (Sandia National Laboratories) for their technical support.

1. INTRODUCTION

Thermal stability of aviation fuels is of concern because of the potential operational problems arising from fuel degradation under thermal stress conditions. Hydrocarbon fuels in contact with heated metallic surfaces form insoluble, carbonaceous deposits that can foul nozzles, manifolds, filters, injectors, and heat exchangers. Temperatures in current aircraft reach approximately 163°C (325°F); temperatures in future aircraft are expected to be much higher. The methods of dissipating the large heat loads will be one of the key factors in determining the capabilities of future aircraft. The use of heat exchangers in which the fuel is used as the primary or secondary coolant appears to be an effective way of dissipating heat. While currently used jet fuels are thermally stable within present aircraft operational limits, the anticipated increases in the thermal loading applied to fuel systems of high-performance aircraft have prompted the development of advanced, thermally stable aviation fuels and methods to predict the stability of these fuels under varying operating conditions.

Sandia National Laboratories, Albuquerque, is conducting efforts to (1) develop instrumentation for monitoring parameters important to the analysis of fuel thermal stability and (2) acquire data related to fuel thermal stability and develop mathematical models for fuel thermal degradation and solid deposition under given operating conditions. This report discusses instrumentation and apparatus developed and used to measure parameter values associated with the formation and deposition of solids from decomposition of hydrocarbon jet fuels. Results of initial tests and model parameters are presented.

2. SYSTEM DEVELOPMENT AND TESTING

Two systems have been developed for monitoring characteristics of fuel thermal stability and are described in this section. The first system uses a quartz crystal microbalance device to quantitatively make *in situ* measurements of mass deposition on a heated metal surface. The second is a light-scattering technique that makes *in situ* measurements of particle size distributions occurring in the fuel as it thermally degrades. Additional liquid-phase and solid-phase characterization studies were performed and results are presented.

A. QUARTZ CRYSTAL MICROBALANCE MASS SENSOR

In the past year we have worked with two jet fuel test systems to monitor the deposition rate of fuel degradation by-products onto surfaces at elevated temperatures. Both systems use a quartz crystal microbalance (QCM) that can be operated submerged in jet fuel to provide a very sensitive real-time measurement of surface mass accumulation. The first system, developed last year, uses a network analyzer to provide a swept-frequency measurement of the QCM response. From this measurement, mass accumulation and properties of the contacting liquid can be determined. While this system performs adequately, it suffers from three drawbacks that would prohibit widespread use: (1) it requires an expensive (~\$30,000) network analyzer, (2) it requires an involved data-fitting procedure to extract the desired mass accumulation information, and (3) the lack of a sealed chamber leads to loss of fuel (through volatilization) that limits the test duration. The second test system, developed over the past year, uses an RF oscillator circuit to drive the QCM at its resonant frequency. This oscillator circuit replaces the network analyzer required in the first system, providing considerable cost savings and simplification in the extraction of mass accumulation information. In addition, the new test system uses a modified pressure reactor to house the QCM sensor and fuel sample, preventing fuel volatilization and allowing measurements to be made with oxygen overpressures.

In this report, we first describe a number of measurements made on JP-8 fuel using the original test system, including (1) mass deposition rates at temperatures between 160 and 200°C, (2) the extraction of activation energies for thermal degradation, and (3) measurement of jet fuel viscosity as a function of temperature. We then describe the new QCM jet fuel test system (QCM-JFTS) and measurements of JP-8 and Jet-A fuel degradation made with this system. We also briefly describe efforts to transfer the QCM-JFTS technology to program participants, including the Pratt & Whitney Fuels and Lubrication Group to support evaluation of jet fuel additives.

1. Mass Deposition Rates

The QCM can be suspended in jet fuel and operated effectively to monitor the accumulation of solids onto the device surfaces. Table 1 lists the mass deposition rates measured using the original test system at several temperatures between 160 and 200°C with two different batches of JP-8 jet fuel. An Arrhenius plot of this data, displaying the natural logarithm of the deposition rate vs. $1000/T$, is shown in Figure 1. It is interesting to note that the two fuel samples are offset on the Arrhenius plot, indicating a different frequency factor in the rate constant. The two data sets have essentially the same slope, however, indicating good agreement in the activation energies: 23.0 vs. 24.7 kcal/mole. These activation energies are consistent with those experimentally obtained (5-44 kcal/mole) from deposition tests from other researchers (see Hazlett, 1991).

Table 1. Summary of QCM Measurements of JP-8 Jet Fuel Degradation Using the Original QCM-JFTS.

JP-8 Batch No.	Temperature (°C)	$1000/T$ (K^{-1})	Deposition Rate ($ng/cm^2 \cdot min$)	\log_e (Deposition rate)	Activation Energy (kcal/mole)
1	160	2.309	20	3.00	23.0
	175	2.231	54	3.99	
	190	2.159	112	4.72	
2	167	2.272	11	2.40	24.7
	182	2.197	26	3.26	
	200	2.113	79	4.37	

2. Measurement of the Temperature Dependence of JP-8 Viscosity

The original QCM-JFTS was used to measure the temperature dependence of the viscosity of JP-8 jet fuel. Due to the interaction of the oscillating device surface with a contacting fluid, electrical measurements can be used to extract the product of density and viscosity of the fluid. Using this data, together with tabulated values for the temperature dependence of JP-8 fuel density, allows determination of fuel viscosity vs. temperature.

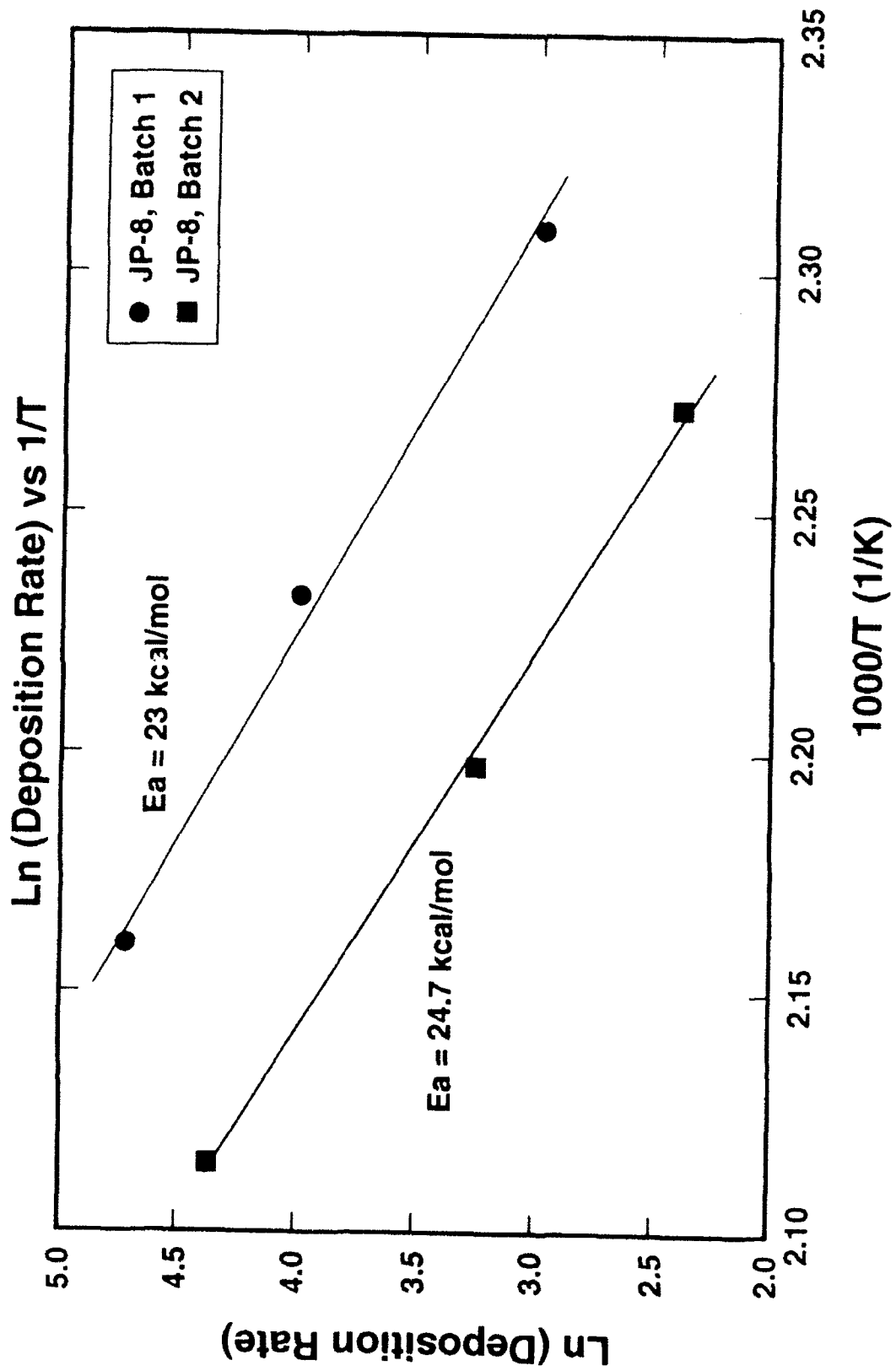


Figure 1 Arrhenius plot yielding activation energies for two different samples of JP-8 fuel

Figure 2 shows the temperature dependence of JP-8 jet fuel viscosity determined from QCM measurements. These measurements are compared with literature values (CRC, 1988) for JP-8 fuel viscosity. We note fairly good agreement between the literature values, at temperatures where they are available, and those extracted from QCM measurements. It is interesting to note, moreover, that JP-8 viscosity does not decrease monotonically with temperature, but shows a peculiar, but reproducible, increase in viscosity with temperature near 140°C. This is the temperature regime where the PCS technique has indicated that particle formation begins. Particle formation may cause an increase in fluid viscosity that is measurable by the QCM. More work needs to be done to ascertain the connection between particle formation, jet fuel viscosity, and the onset of mass deposition. The onset of this nonmonotonic viscous behavior could be valuable with regard to predicting jet fuel stability.

3. New Jet Fuel Test System

A goal of the program is to develop a bench-top instrument for monitoring jet fuel degradation in real time and at high temperatures. This will allow other laboratories to characterize new jet fuels and to evaluate the effect of a variety of parameters related to fuel thermal stability, including the effect of fuel additives. Because the surface of the QCM can be coated with different metals, the suspected catalytic effect of certain metals in promoting jet fuel degradation can also be investigated.

In the past year we assembled a "second generation" QCM jet fuel test apparatus, shown schematically in Figure 3. The apparatus includes a QCM test fixture to contain the QCM suspended in a jet fuel sample, an oscillator to drive the QCM, a frequency counter and digital voltmeter to monitor the oscillator outputs, a temperature controller to maintain fixture temperature, a scanning thermometer to read fuel temperature, a gas flow meter (when flowing gas), and a personal computer (PC) to acquire and display sensor data.

The QCM test fixture houses the QCM sensor suspended in a sample of jet fuel, allowing mass accumulation to be measured at elevated temperatures and with oxygen overpressures. The fixture, shown schematically in Figure 4, consists of a stainless steel pressure vessel (Parr Instrument Co.) custom modified to allow an RF electrical feedthrough to be mounted in the lid. Hermetically-sealed SMA feedthroughs were welded into the center of the lid, to which is attached a QCM clamp. This clamp holds the edge of a QCM, making electrical contact to the electrodes. The lid of the test fixture also contains feedthroughs for an oxygen inlet and vent tube, a pressure gauge, a pressure relief valve, and a thermocouple. The lid seals to the body of the vessel with a Teflon gasket and clamps, allowing oxygen overpressures of up to 1000 psi to be maintained during the test. The QCM test fixture is mounted in a band heater, allowing test

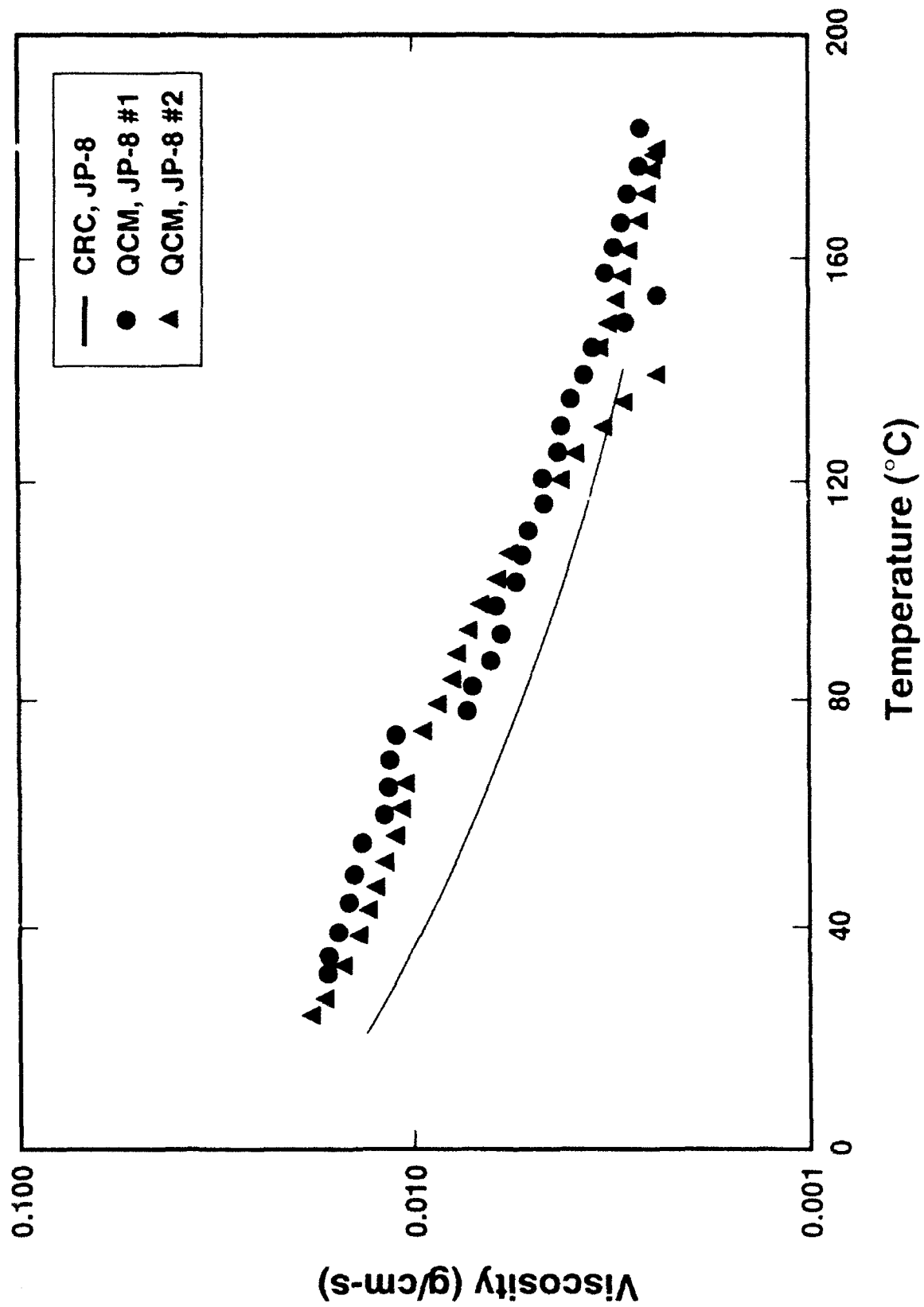


Figure 2 Measured viscosity values from the QCM system compared with literature values for a JP-8 fuel

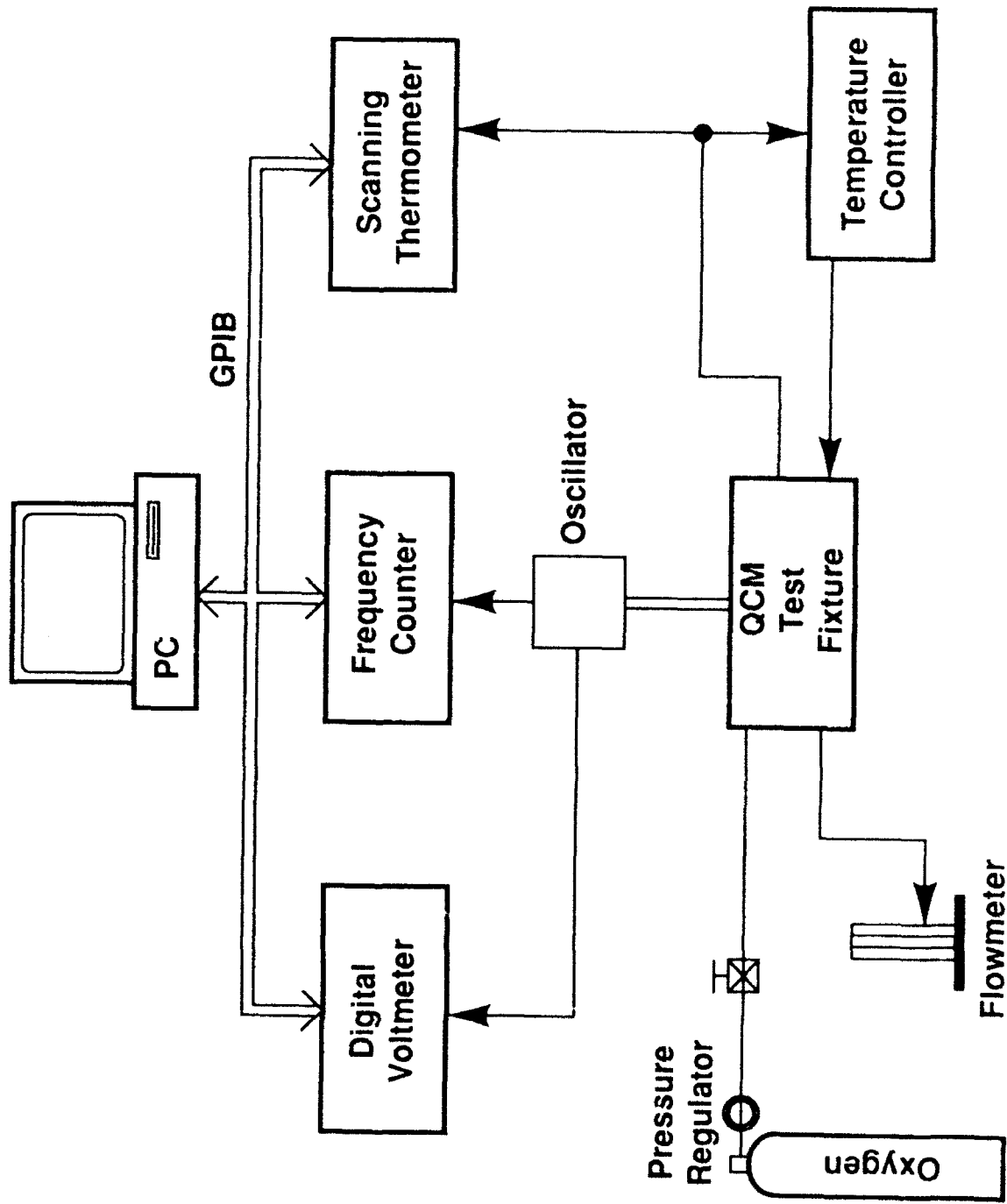


Figure 3 Schematic of the second-generation QCM system

QCM Test Fixture (Modified Bomb Calorimeter)

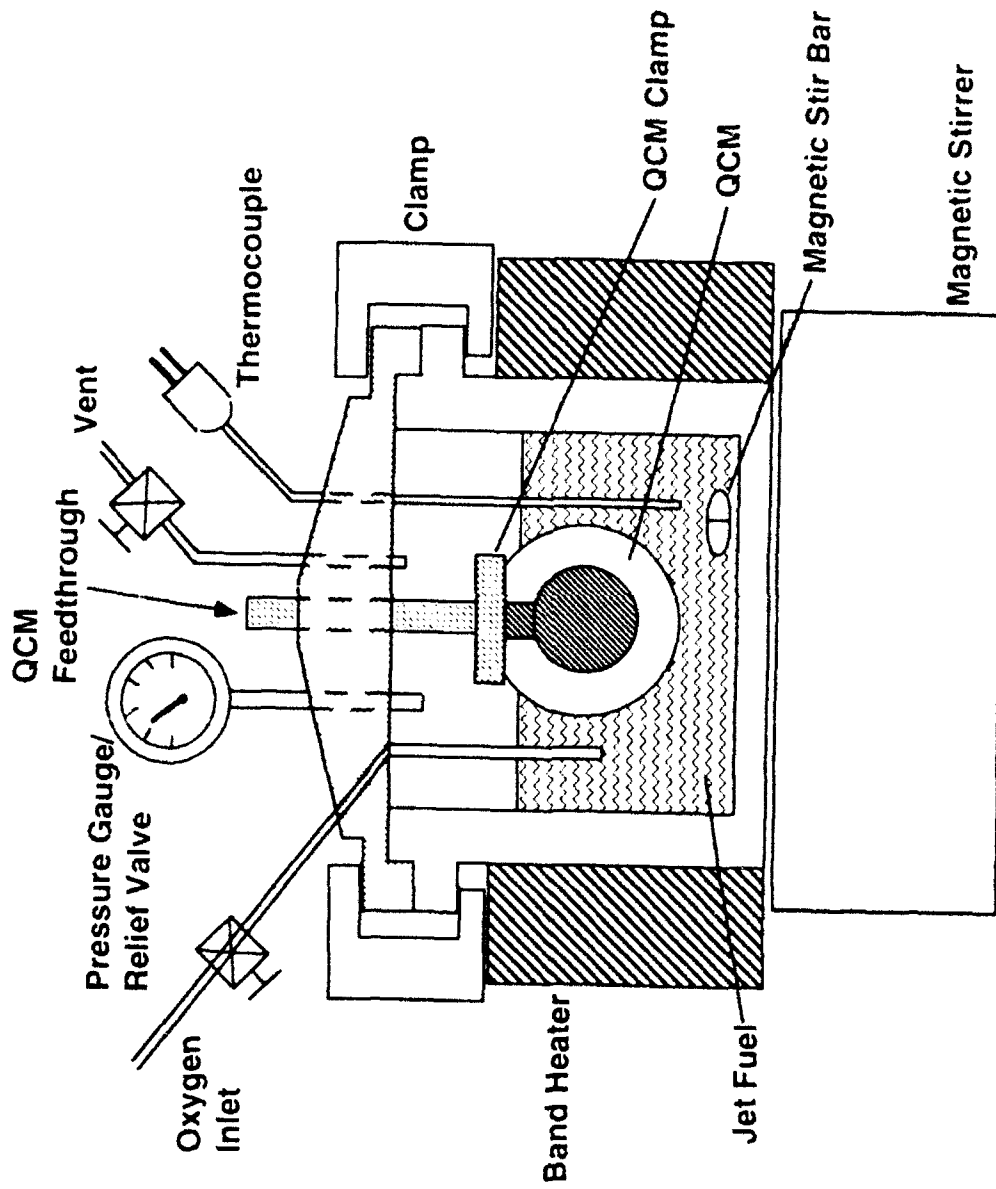


Figure 4 Schematic of the QCM system stainless-steel test fixture to contain the quartz crystal microbalance suspended in a jet fuel sample

temperatures up to 300°C to be achieved. In addition, the unit is suspended by a clamp stand above a magnetic stirrer, allowing the fuel sample to be mixed during the test, maintaining a uniform temperature and oxygen concentration

A key component of the second generation QCM-JFTS is an oscillator circuit that drives the quartz resonator suspended in jet fuel. This circuit uses the impedance variations inherent in the QCM resonant response to track the resonance frequency of the sensor. Due to the severe operating environment, commercial oscillators proved inadequate. Consequently an oscillator was custom-designed for this application. The oscillator board is unique in providing both a frequency and amplitude output: frequency changes indicate mass accumulation while amplitude indicates crystal damping. (A patent disclosure has been filed.) The polymeric nature of the fuel degradation by-products leads to both responses. The oscillator circuit is potted in epoxy for ruggedness and better temperature stability.

The oscillator frequency output is read by a frequency counter (HP model 5384A) and input to the PC as an indicator of mass accumulation. The gate time of the counter is controlled by the computer and varies from 0.1 s to 10 s. There is a trade-off between the precision and rate at which frequency data can be acquired. Consequently, at high data rates (e.g., 1-sec interval) a short gate time is used (0.1 s), resulting in lower frequency resolution (1 Hz). At lower data rates (e.g., 30-sec intervals), a longer gate time is used (10 sec), resulting in higher frequency resolution (0.01 Hz). The mass density ρ_s (mass/area) accumulated on each crystal face is related to the change in resonant frequency Δf (measured at constant temperature) by:

$$\rho_s = - c_m \Delta f / f_o^2 \quad (1)$$

where $c_m = 2.210 \times 10^{11}$ g/cm²-s and f_o is the original resonant frequency of the device (~5 MHz).

Interpreting frequency changes in terms of mass accumulation according to Eq. 1 will be erroneous if the fuel and crystal temperatures are varying, since fuel viscosity will vary with temperature and contribute a frequency change also. In addition, the resonant frequency of the crystal itself has some slight temperature dependence. Consequently, the acquisition of frequency data should begin only after the fuel sample has stabilized at the test temperature.

The amplitude output of the oscillator is a dc voltage that is read by a digital voltmeter and input to the PC. This voltage increases with crystal damping and is proportional to the motional resistance (R) of the crystal. Monitoring the crystal damping is useful for several reasons. Crystal damping is proportional to the square root of the liquid density-viscosity product. While fuel density does not

vary appreciably with temperature, fuel viscosity decreases significantly with temperature and can thus be monitored with the amplitude output of the oscillator. Secondly, as fuel degradation by-products accumulate on the crystal, the viscoelastic nature of these deposits leads to crystal damping in excess of that contributed by contact with the fuel. Thus, changes in the amplitude output serves as a secondary indicator of deposit thickness. The relationship between the damping output and deposit thickness, however, does not appear to be as straightforward as between frequency output and deposit thickness. Thirdly, the amplitude output is a useful diagnostic indicator: faulty electrical contact between the QCM and clamp, for example, is reflected in an intermittent or anomalously high damping output.

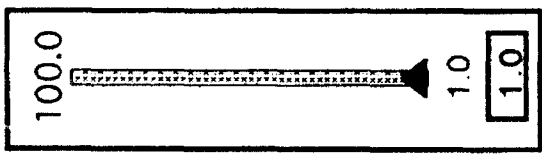
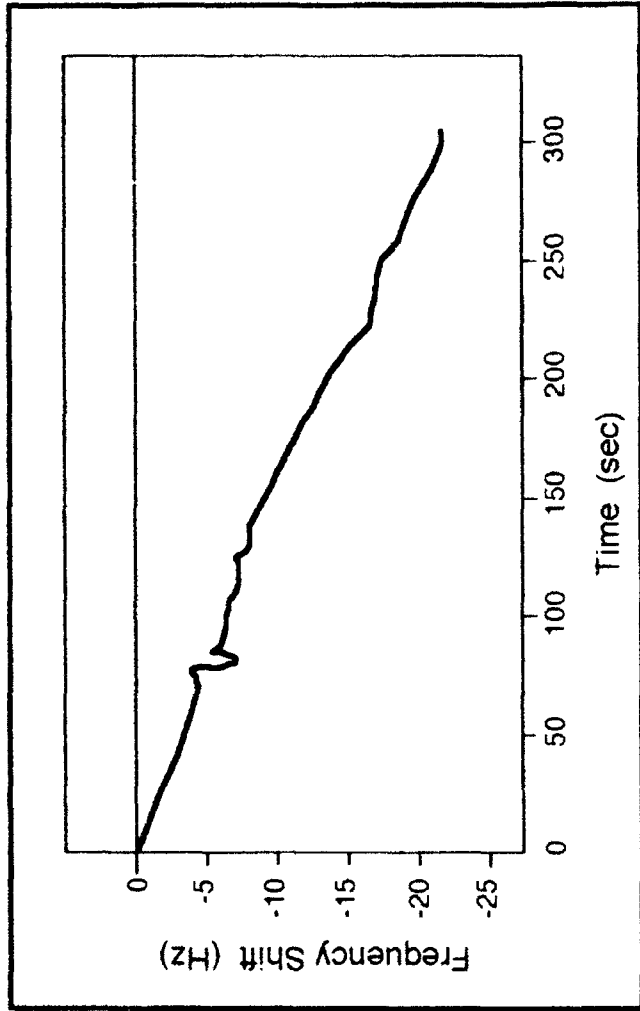
A temperature controller (Parr model 4842) reads the thermocouple in contact with jet fuel and controls current flow to the band heater in order to maintain the jet fuel at a constant test temperature. When the fuel is magnetically stirred, the temperature controller requires about 50 minutes to reach 180°C and stabilize, maintaining fuel temperature to within 0.1°C of the target temperature. Efforts are being made to reduce this heat-up time.

A scanning thermometer also reads the thermocouple contacting the jet fuel and sends this information to the PC. This temperature information is recorded by the PC and can be used to indicate when the test temperature has been reached, triggering the acquisition of data from the frequency counter and digital voltmeter

A personal computer acquires data during the test, displaying it in real time and storing it for later use. The computer can be any IBM AT-compatible computer capable of running Windows 3.1 and DOS 5.0 and supporting a mouse. The PC communicates with the digital voltmeter, frequency counter, and scanning thermometer via a parallel interface bus (GPIB).

A user-friendly program running in a windows environment displays a "control panel" (Figure 5) for controlling the test and monitoring the data in real time. The program is a Sandia proprietary program written in the *HP Instrument Basic for Windows* program environment. The user controls the test via a panel that includes "buttons" that are mouse-selectable, including (1) Start Run, (2) Cancel Run, (3) Save Data, (4) Set Temp, and (5) Auto Store. "Set Temp" allows the user to set the center and range of temperatures displayed. It also allows the user to select the option of acquiring data only when the fuel temperature is within 0.1°C of the target temperature. "Save Data" allows the user to save the acquired data at any time during the run. The data stored consist of an array including (1) time, (2) temperature, (3) oscillator frequency, (4) oscillator amplitude, and (5) mass accumulation (determined from the frequency change referenced to the start of the run according to Eq. 1). These data are stored in ASCII format (with a comma used as delimiter) in a filename of the user's choice.

Sensor Monitor



Data Interval

- Start Run
- Cancel Run
- Save Data
- Set Temp
- Auto Store

Data Point	285
Run Time (s)	305
Mass ($\mu\text{g}/\text{cm}^2$)	0.0

Damping	2.0
Temperature ($^{\circ}\text{C}$)	22.0

Figure 5. Control panel layout for the QCM data acquisition programs in a IBM-compatible Windows operating environment

The data can be retrieved later by a commercially available software package (e.g., Sigmaplot or Excel) for plotting and regression. The panel also includes a "slider" input that is mouse-activated to permit the user to set the data acquisition rate between 1.7 and 100 s. The data rate selected automatically changes the gate time of the frequency counter to obtain the best frequency resolution, as discussed above.

Panel displays include (1) a "strip chart" display of frequency changes (referenced to the start of the run) vs. data point number, (2) a "meter" display of crystal damping, (3) a "meter" display of temperature, and (4) a window display of data point number, elapsed time, and mass accumulation (in $\mu\text{g}/\text{cm}^2$).

To date, tests with the new jet fuel test system have been performed using the following procedure:

- (1) A 60 ml sample of jet fuel is placed in the clean test fixture.
- (2) A clean -inch diameter QCM (Maxtek) is placed in the QCM clamp and the lid is clamped onto the chamber.
- (3) Oxygen is bubbled through the jet fuel for 20 minutes at room temperature to saturate the fuel with oxygen (optional).
- (4) The outlet valve to the chamber is closed and the chamber is pressurized with oxygen to 50 psi.
- (5) The temperature controller is set to the desired test temperature.
- (6) When the fuel temperature reaches the test temperature the "Start Run" program button is selected and data acquisition begins.
- (7) The data rate is set on the slider to 15 sec; "Temp Set" is selected and the center temperature is set to the test temperature; span temperature is set to 5 deg.
- (8) After 2 hours of data acquisition, "Save Data" is selected; the disk drive and filename are entered for data storage. If the number of data points reaches 499 beforehand, the program will stop and request this information for data storage. Alternatively, the "Auto Store" button can be selected beforehand to supply this information and data will be stored automatically at 499 points.
- (9) The temperature controller is turned off and chamber allowed to cool; chamber pressure is then vented before opening. Data are retrieved with a plotting/regression program; fitting the mass vs. time data yields a mass accumulation rate.

The operating parameters (such as temperature, pressure, atmosphere, data collection rate) used in this procedure can be easily changed as desired.

The mass accumulation data acquired with JP-8 at 180°C with a 50 psi oxygen overpressure are shown in Figure 6. Fitting the data yields a mass accumulation

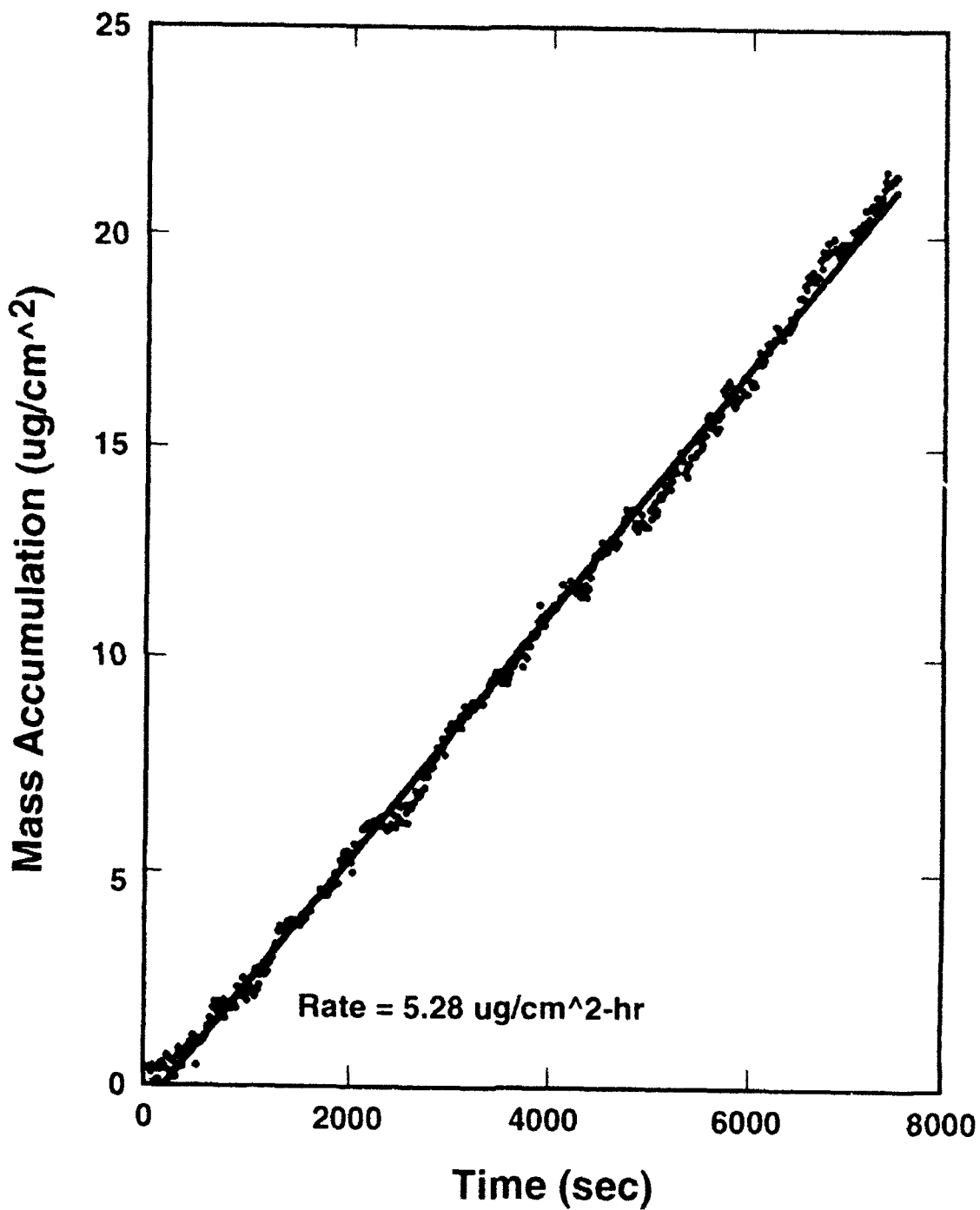


Figure 6. Typical data acquired by the QCM system on mass accumulation versus time; data showed for JP-8 degradation at 180°C with a 50 psi oxygen overpressure.

rate of $5.28 \mu\text{g}/\text{cm}^2\text{-hr}$. We note very little fluctuation in the data about the best-fit line. Data collection is generally initiated after the temperature has stabilized at the set-point temperature. With the present instrument configuration, where the set-point temperature can be maintained within approximately 0.5°C , mass accumulation rates as low as approximately $0.3 \mu\text{g}/\text{cm}^2\text{-hr}$ can be measured. Table 2 lists mass accumulation rates measured with the new jet fuel test system for JP-8 and Jet-A fuels at several temperatures, all at 50 psi oxygen overpressures, under stirred fuel conditions.

Table 2. Summary of QCM Measurements of Jet Fuel Degradation Using the New QCM-JFTS.

Fuel	Temperature ($^\circ\text{C}$)	$1000/T$ (K^{-1})	Deposition Rate ($\text{ng}/\text{cm}^2\text{-min}$)	\log_e (Deposition rate)	Activation Energy (kcal/mole)
JP-8	160	2.309	19.2	2.955	24.2
	170	2.257	41.1	3.716	
	180	2.208	88	4.477	
	200	2.114	208	5.338	
Jet-A	160	2.309	15.6	2.750	27.8
	170	2.257	21.9	3.085	
	180	2.208	48.7	3.886	
	200	2.114	219	5.389	

Figure 7 shows an Arrhenius plot of the deposition rate vs. the reciprocal temperature of the run for JP-8 fuel. The activation energy extracted from this plot, 24.4 kcal/mol , is in good agreement with estimates obtained using the original JFTS (Table 1) for JP-8: 23.0 and 24.7 kcal/mol .

In conclusion, the new QCM-JFTS is a user-friendly apparatus allowing rapid evaluation of jet fuel samples through the measurement of nanogram to microgram quantities of deposits on a surface.

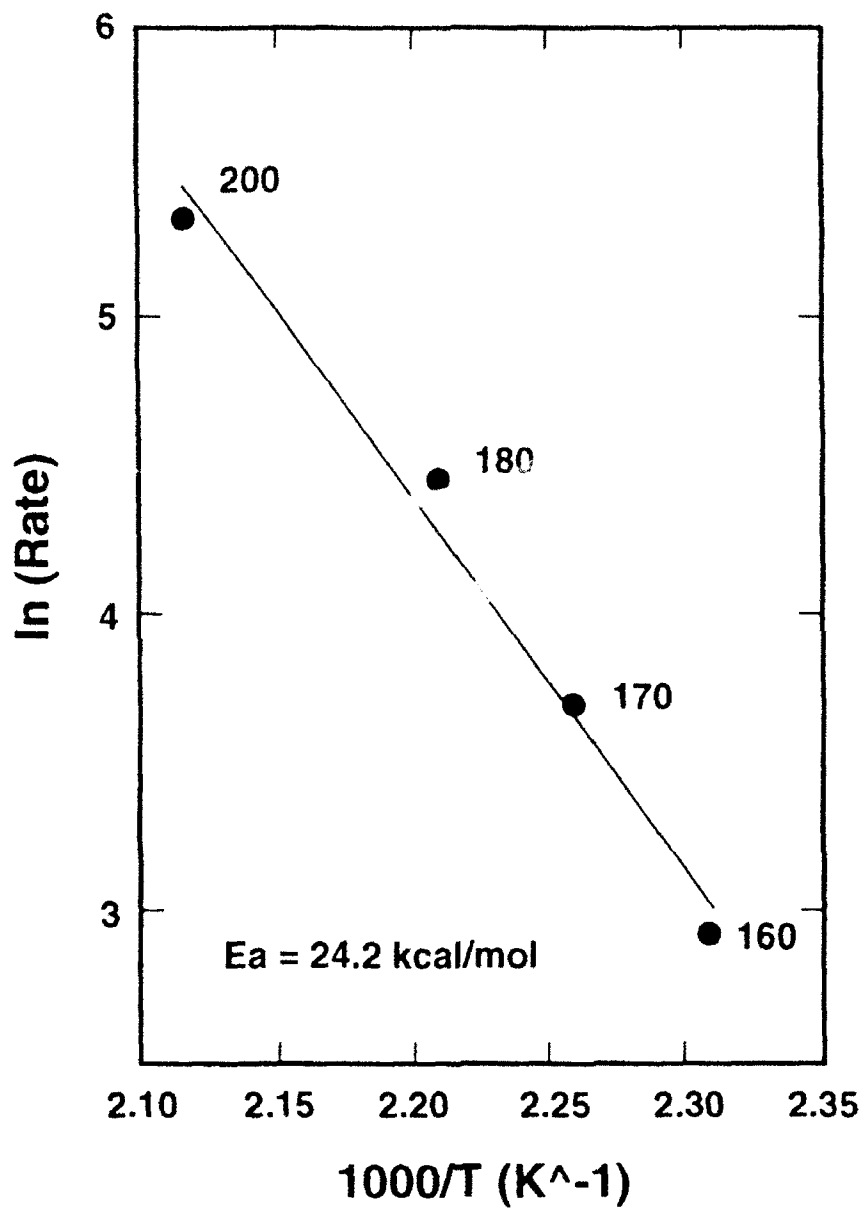


Figure 7 Arrhenius plot for JP-8 fuel, 50 psi oxygen overpressure, using the second-generation QCM system.

4. Technology Transfer of the QCM Mass Sensor

A visit to Pratt & Whitney Fuels and Lubrication Group was made in August 1992, by Elmer Klavetter and Steve Martin of Sandia National Laboratories to set up a QCM-based jet fuel test system. We have provided Tedd Biddle with plans for the test fixture and the apparatus associated with the complete test system. We have also supplied the HPIB interface board, the oscillator, and the custom computer program that acquires QCM data and extracts the accumulated mass density.

Additionally, we have supplied Wright Laboratory and their contractors with the system design, the list of equipment required for the system, and the plans for the test fixture. We anticipate setting up systems at Wright Laboratory shortly.

B. PHOTON CORRELATION SPECTROSCOPY SYSTEM

1. System Improvements

A noninvasive dynamic light scattering technique, photon correlation spectroscopy (PCS), has been applied to examine the formation of submicron diameter particles in thermally stressed JP-8 and Jet A-1 fuels. Early results of this work have been documented in Trott et al., 1992. Of the few techniques available for measurement of submicron diameter particles suspended in a liquid (Weiner, 1984), PCS may be the most suitable for noninvasive, *in situ* measurement of the small particles generated in jet fuel thermal stability tests. PCS is a laser-based technique for measurement of particle diffusion coefficients, which are then used to determine particle hydrodynamic diameters in the range 3 nm to several microns. *In situ* measurements are needed to ensure that particle measurements are made at the desired thermal stress temperature and exposure time and to eliminate particle settling effects. The capability of PCS for accurate sizing of small particles is particularly important since much of the relevant fuel degradation chemistry apparently occurs in a regime where particle diameters are generally less than a few hundred nm (Bolshakov, 1974).

PCS requires only a relatively simple optical setup, as shown in Figure 8. Detailed discussions of PCS instrumentation and data reduction methods are available (Oliver, 1974; Berne and Pecora, 1976; Weiner, 1984). PCS uses a digital autocorrelation technique to measure the time-dependent intensity of the scattered light signal caused by Brownian motion of particles in an illuminated sample (Klavetter et al., 1992; Trott et al., 1992). Figure 9 presents examples of autocorrelation functions collected during thermally stressed Jet A-1 experiments. The channel number plotted in Figure 9 is a measure of the autocorrelation delay time. In general, unstressed fuel samples exhibit no correlation, indicating that very few particles are present. As the fuel is heated, at some temperature a weak

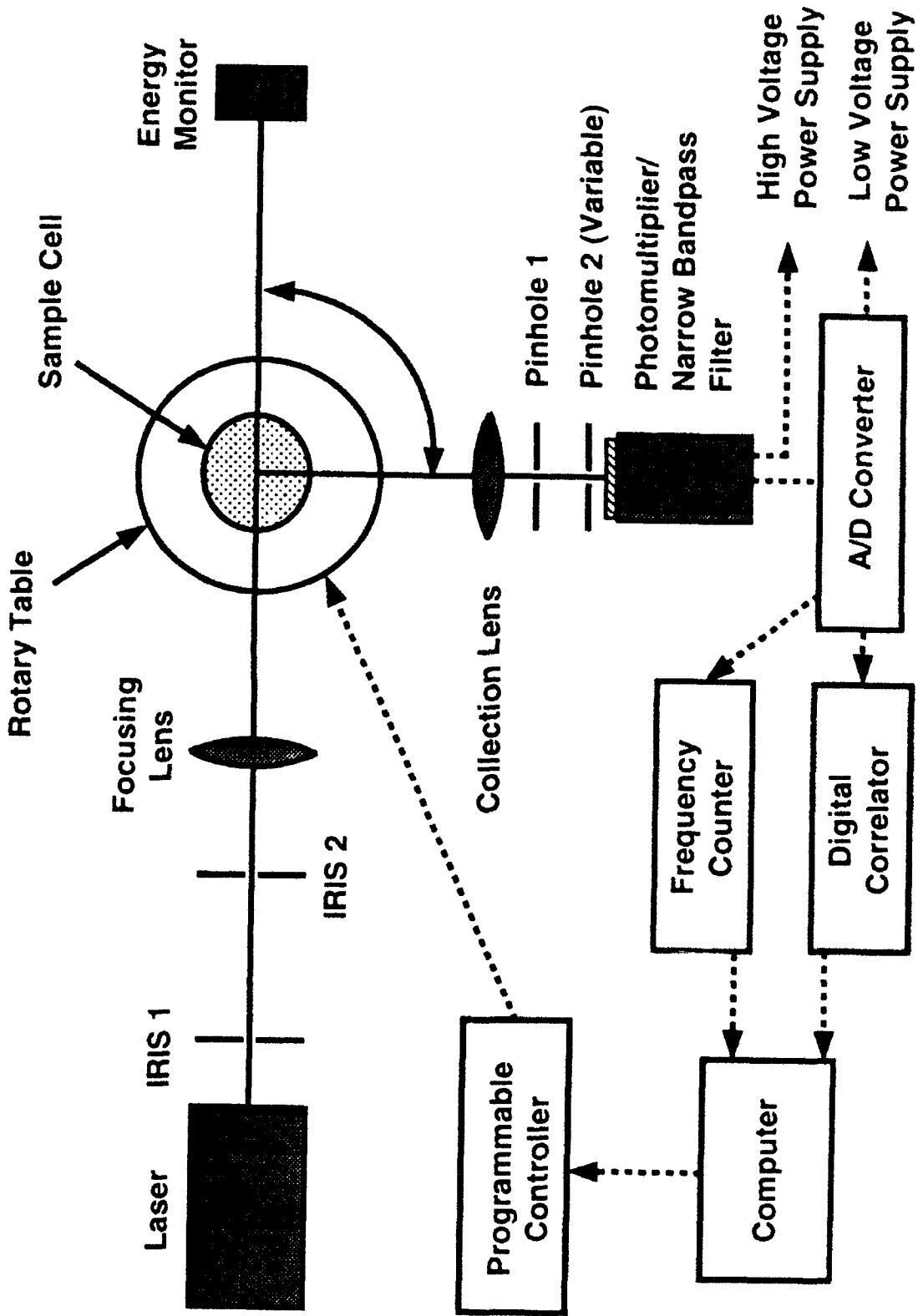


Figure 8 Schematic layout of PCS system for studies of heated jet fuels

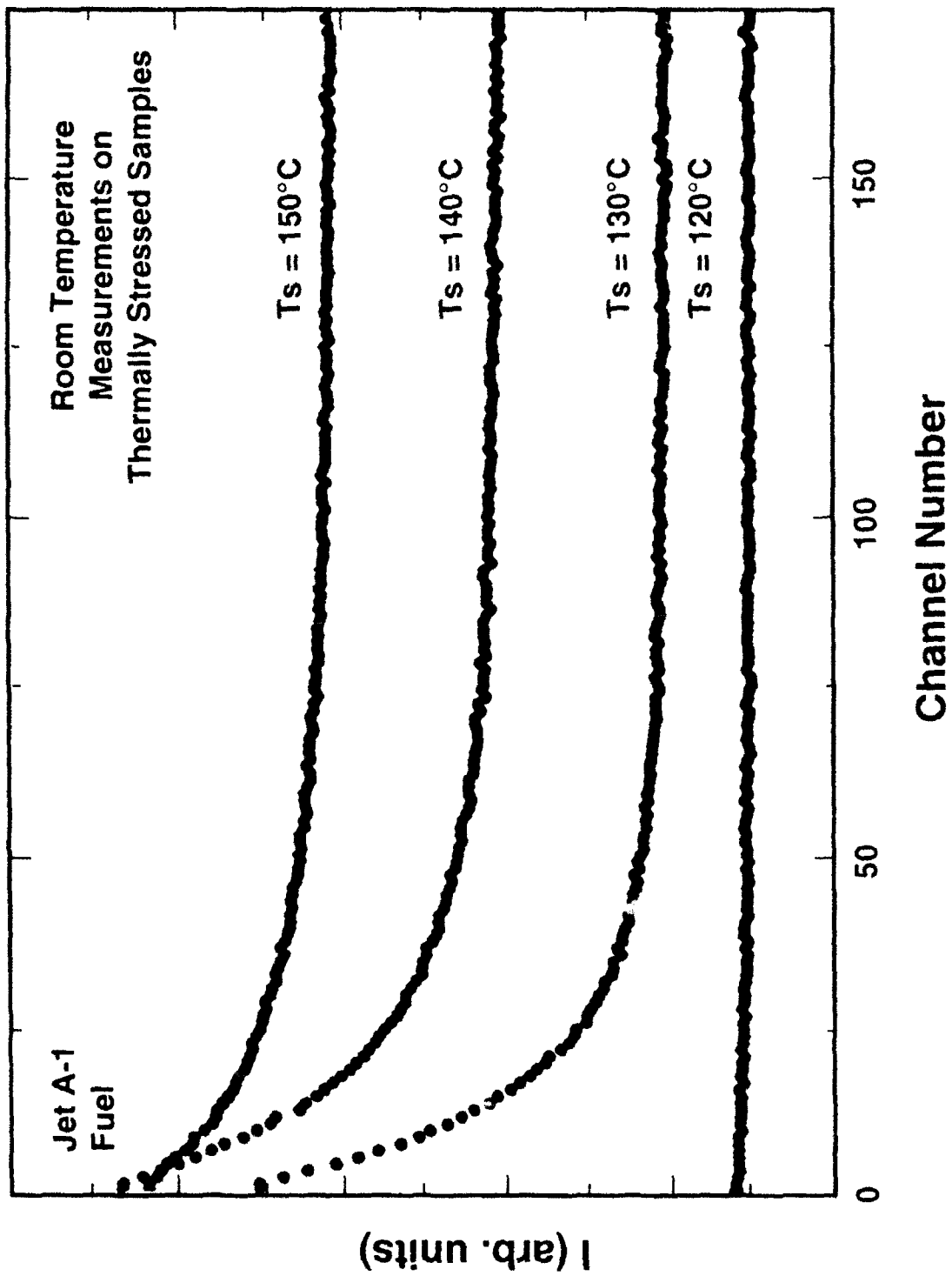


Figure 9. Measured correlation function for four Jet A-1 samples heated to different temperatures. PCS was performed at room temperature. The correlation is weak for the sample heated to 120°C, but becomes well-defined as samples are taken to higher temperatures. The sample time per channel for the 120°C sample was 3×10^5 seconds, for the other samples the sample time per channel was 1×10^4 seconds.

correlation becomes evident, as shown in the 120°C sample in Figure 9. The figure shows that at higher fuel stress temperatures the correlation becomes more well-defined, and simpler to analyze with the software routines described below. A Langley-Ford LFI 1096 digital correlator is used in these experiments. A portion of the scattered light signal is also sent to a frequency counter to provide a continuous display of the intensity of the scattered light signal (proportional to particle size and concentration) and to ensure that the total photon count rate is maintained below 10 MHz (Weiner, 1984). Although nearly all PCS measurements presented in this report were made at a fixed 90 degree scattering angle, the capability for multiangle scattering measurements is available. This capability is required for complete determination of complex particle size distributions (Bott, 1987).

Data analysis options include first and second cumulants analysis of the correlation waveform with the AN01 option on the LFI 1096 digital correlator, which directly yield the mean diameter of a simple monomodal particle distribution. For full determination of the more complex particle size distributions expected, additional analysis routines are available (Russo et al., 1988) including CORAN (a 1st to 3rd order cumulants analysis routine for data screening and summation), MARLIN (a discrete exponential fitting program), EXSAMP (a rapid, smoothed algorithm for Laplace inversion of the first order autocorrelation function), and the CONTIN Laplace inversion routine.

To validate and characterize the performance of the PCS system, monodisperse and bimodal samples of polystyrene spheres have been examined (Klavetter et al., 1992). Accurate particle sizing in the 20-500 nm diameter range was obtained, and sizing errors due to sample convection were negligible over the range 20-85°C. The calibration particles are routinely used to optimize choices of the sample volume-defining pinholes and the collection optics, and for verification of PCS system performance in measurement of particles of similar diameter to those obtained in thermal stress tests.

Temperature Uniformity

Early PCS tests on heated jet fuel suggested that incipient particle formation can occur at temperatures as low as 110°C, and that substantial changes in the mean particle size occur over ranges of only 10-20°C (Trott et al., 1992). These results also demonstrated that temperature nonuniformities in the test cell can be a source of difficulty in interpreting the data. The sample cell/heater device used in these early PCS tests consisted of cylindrical copper shells that fit tightly over the top and bottom of a 25 ml cylindrical glass sample cell, leaving a small gap in the middle for optical access to the fuel. Heating tapes were wound tightly around the copper shells. These tapes were controlled by a thermocouple feedback unit which could be set to maintain the fuel at a desired temperature. Thermocouples were positioned to determine temperatures at two locations in the fuel samples,

one close to the PCS measurement location and one at the upper fuel surface. These measurements demonstrated that significant temperature gradients were established in the samples when heating with this apparatus. For example, for nominal center temperatures of 120°C and 150°C, the maximum temperatures (near the upper surface) were determined to be 138°C and 183°C, respectively. In this device, the observed mean particle diameters (as determined by PCS) appear to correlate primarily with particle formation occurring in the hottest part of the sample (see following discussion). In some cases, a bimodal distribution of particle sizes was observed, reflecting slow formation of small particles in the bulk fluid in addition to concurrent and facile generation of large particles in the higher temperature regions near the surface.

Much improved temperature uniformity has been obtained with a device that consists of a cubical quartz sample cell (3.8 cm length) that is heated by completely enclosing it in a copper clamshell heater. Heating coils are wound through the copper walls of the clamshell and a thermocouple readout/controller unit is used to bring the temperature up to the setpoint. Four sides of the clamshell contain small windows for optical access to the fuel. The liquid volume is approximately 50 ml. Figure 10 displays temperature histories measured during a 150°C test on Jet A-1 using five thermocouples positioned in and around the 3.8 cm quartz cube. Four thermocouples were located inside the fuel at the bottom, top, side and center (near the PCS measurement location) of the quartz cube, respectively. The fifth thermocouple was located in the gap between the cell and the copper clamshell walls. After 60 minutes, temperatures within the fuel approached the maximum value of 150°C and agreed to within 1.5°C. The relatively high degree of temperature uniformity in tests with this sample cell/heater device is presumed to be due to fairly strong convective flows within the cell. These uniform conditions permit far more definitive PCS and static light scattering measurements.

Heating Rate and Control

In order to increase the heating rate and control, a new programmable Eurotherm PID temperature controller was installed. With careful programming of this controller, it is possible to avoid temperature "overshoot" in a fuel sample as well as achieve acceptable uniformity. Only a few heating tests are required to establish the optimal parameters to bring a sample to a given temperature. These parameters have been determined for test temperatures in the range 130-160°C. Sample-to-sample variations in heating rates are negligible. Figure 11 shows temperature measurements at various points in the test cell during a 150 °C Jet A-1 heating test. The fuel reaches the setpoint temperature in about 20 minutes, and is maintained at temperature to within 1%. For the 3.8 cm cube, the temperature uniformity throughout the cell is excellent, as shown in Figure 11.

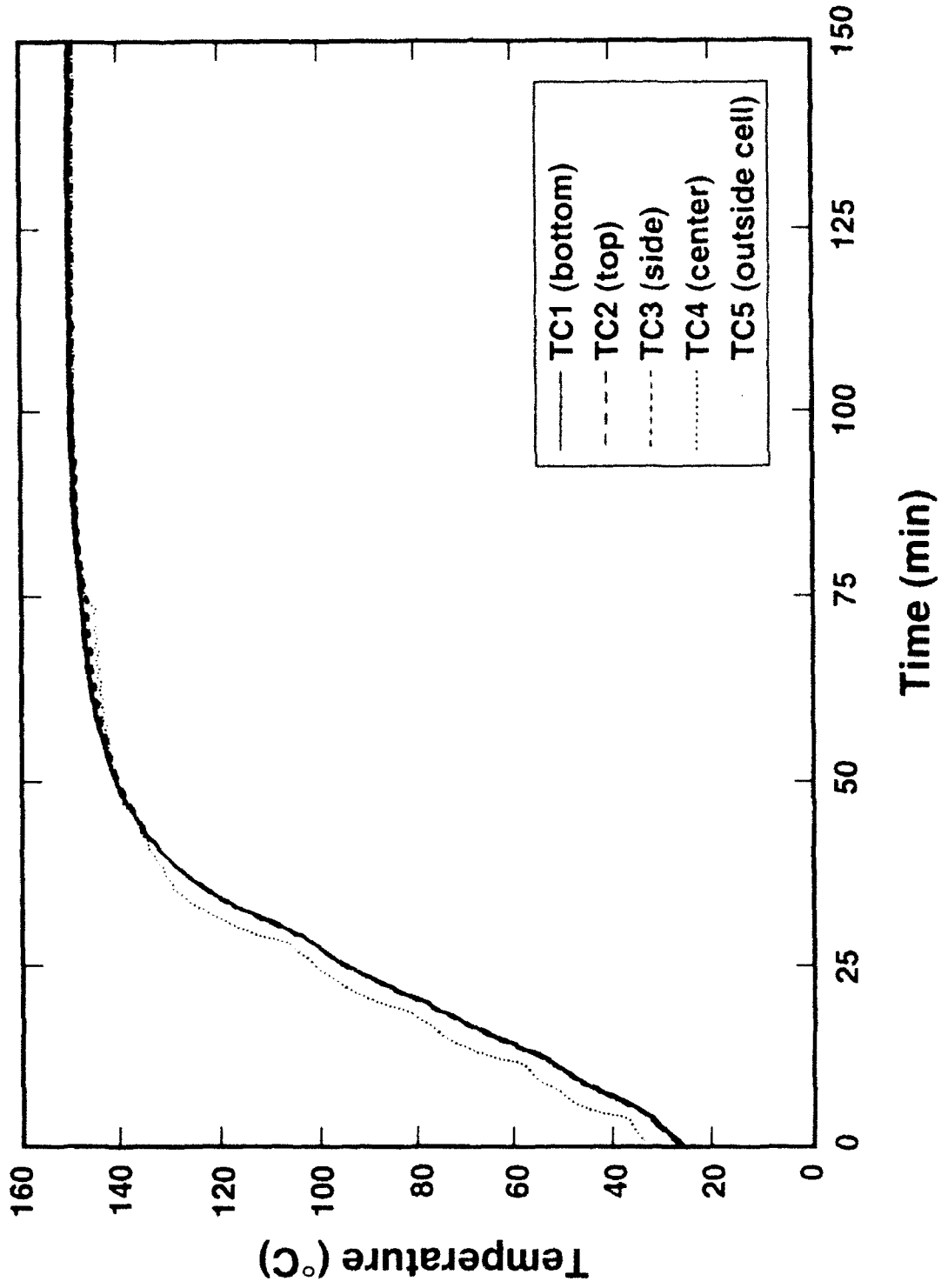


Figure 10 Temperature measurements at various points in the 3.8 cm quartz cube during heating of Jet A-1 fuel. Thermocouple locations are noted on legend

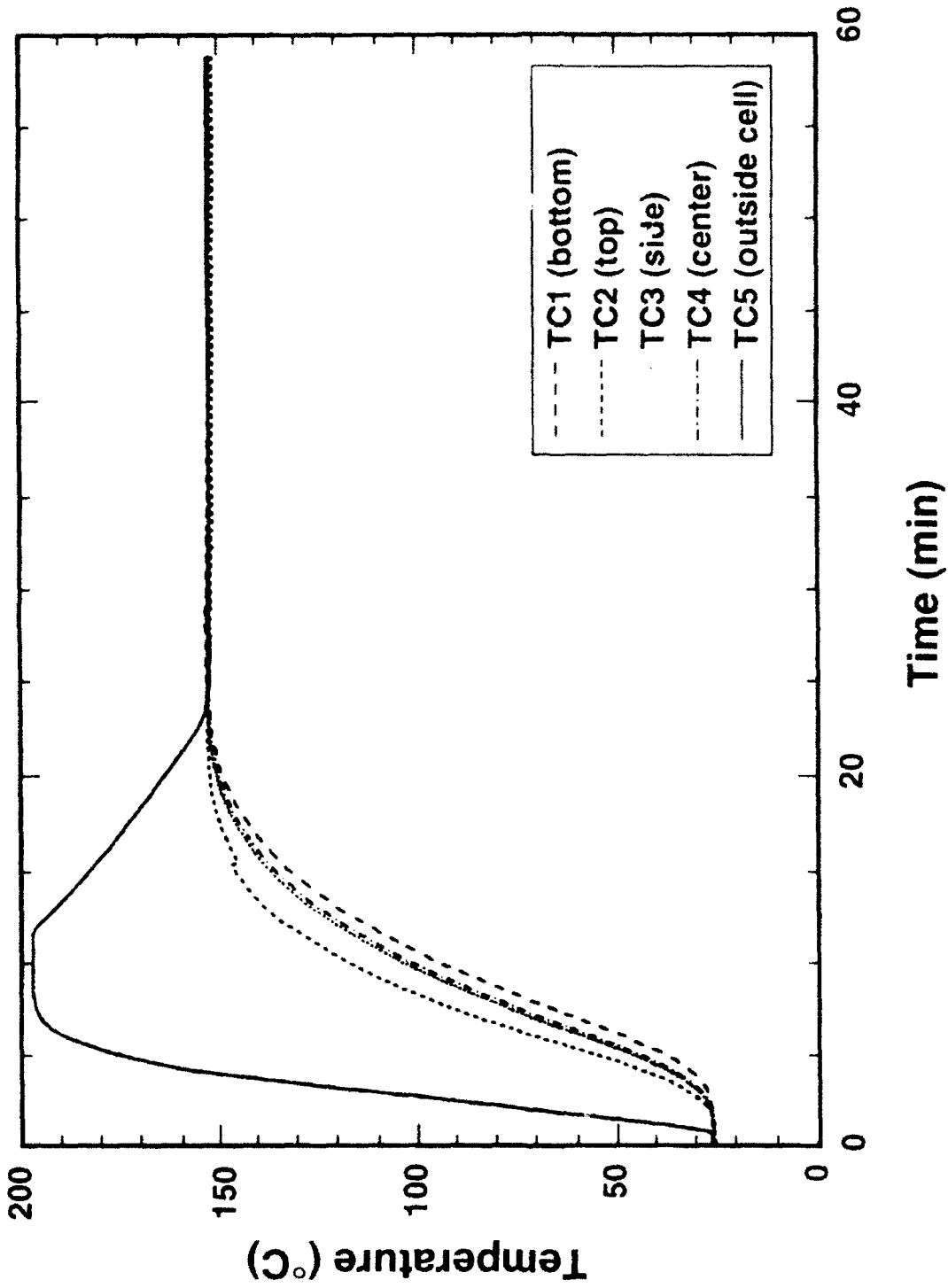


Figure 11 Temperature measurements at various points in the 3.8 cm quartz cube during heating of Jet A-1 fuel with new temperature controller. Thermocouple locations are noted on legend

Temperature Flow Visualization

A selection of photochromic cholesteric liquid crystal beads encapsulated in plastic has been obtained (Hallcrest Products, Parsley, 1991). Such beads are expected to be of value in visualizing the temperature uniformity throughout the entire heated volume, unlike thermocouple measurements which can give only point temperatures at a few locations in the field. The light scattering properties of the liquid crystal beads change when they are exposed to different temperatures, changing the wavelength of white light reflected from the beads. The beads tested start out with a clear appearance, change to reflect red at some fixed temperature (the red start temperature), then change to reflect light of increasingly shorter wavelength as the temperature is increased through the active range of the crystal (color play bandwidth). Preliminary heating tests have been performed with 10-15 and 50-100 micron beads, with fairly low active temperatures (red start temperature of 29°C, color play bandwidth of 4°C). These tests have shown that the beads are useful for visualization of full temperature fields and their time evolution, but have shown that the observed color is strongly angle dependent, so a fixed viewing angle must be chosen carefully. Although the commercially available beads have fairly low red start temperatures for fuel heating experiments (normally less than 115°C), they should be very useful for establishing the uniformity of various heating cells and techniques.

Improvements to PCS Software

A new PCS control program has been written and implemented. This program makes PCS measurements and data analysis much more "user friendly" by providing three basic new features. First, the program performs an automatic initialization of the Langley Ford LFI 1096 correlator with the most commonly used test parameters and sets it up for computer control. Second, it allows the PCS operator to set up the correlator to acquire multiple data runs with an operator-specified number of runs and acquisition times. Finally, it provides menu-driven access to all of the existing data analysis routines.

2. Mie Scattering Computations/Experiments

In order to enhance the capability of our dedicated photon correlation spectroscopy (PCS) system and to aid in the interpretation of the data, we have added a Mie scattering program to the available set of dynamic light scattering analysis software. The Mie scattering routine provides insight in selection of optimal scattering angles and source wavelengths for analysis of various distributions of particle sizes. Moreover, this program will be useful for evaluation of detection sensitivity of the PCS apparatus as a function of particle diameter and in adapting the PCS system to static light scattering measurements on larger

particles (>300 nm diameter). The Mie scattering routine is a simple adaptation of the FORTRAN routine "CALLBH" described in Bohren and Huffman, 1983. The program computes Mie intensity parameters versus scattering angle for a given sphere (particle) refractive index, medium refractive index, sphere radius, and free space wavelength of the optical source. We have modified the routine to allow keyboard input of wavelength, sphere radius, and number of angles.

Relative scattering intensities versus angle have been calculated for "Nanosphere" polystyrene particle standards (Duke Scientific, Palo Alto, CA) in the diameter range of 20-500 nm. Results are shown in Figure 12 (for a HeNe laser source at 632.8 nm) and Figure 13 (for an argon ion laser at 514.5 nm). In comparing results at different wavelengths, the scattered intensity (for perpendicular polarization), $I_1(\theta)$, is expressed by:

$$I_1(\theta) = I_0 \lambda^2 i_1 / (4\pi^2 R^2) \quad (2)$$

where I_0 is the incident intensity, λ is the source wavelength, i_1 is the Mie intensity (relative scattering) parameter, θ is the scattering angle, and R is the distance from the scattering volume. These calculations illustrate the well-known $d^6\lambda^4$ behavior of scattering intensity as a function of particle diameter, d , in the Rayleigh regime ($d < 70$ nm) as well as the complex dependence of scattering intensity vs. θ for larger particles ($d > 100$ nm).

Figure 12 includes observed intensities of scattered light as a function of θ for a solution containing 496 nm "Nanospheres" normalized to the calculated value at $\theta = 90^\circ$. For these preliminary measurements, no attempt was made to account for background scattering or to control the accuracy of the scattering angle to better than 1° . In view of these limitations, the experimental data are in good agreement with the calculated angular dependence of scattering intensity.

3. Jet Fuel Testing with Photon Correlation Spectroscopy

The continuing goal of these experiments is to determine the temperature and exposure time dependence of particle formation mechanisms. Thus far, tests have been performed in oxidative atmospheres to promote particle formation and growth. The fuels examined have been specification-grade JP-8 and Jet A-1 (POSF-2747). The Jet A-1 had an atypically high JFTOT breakpoint temperature of 330°C . The breakpoint temperature for the JP-8 was approximately 270°C . Unfiltered JP-8 and Jet A-1 fuels were both found to contain sufficient numbers of dust particles to complicate acquisition of the correlation function at small scattering intensities. With filtration, nearly dust-free samples can be generated; however, the possible effects of this sample preparation step on the overall particle formation process (during heating) have not yet been fully characterized. For most *in situ* tests reported here, fuel samples were prepared by filtering each sample through 10-micron Teflon filters,

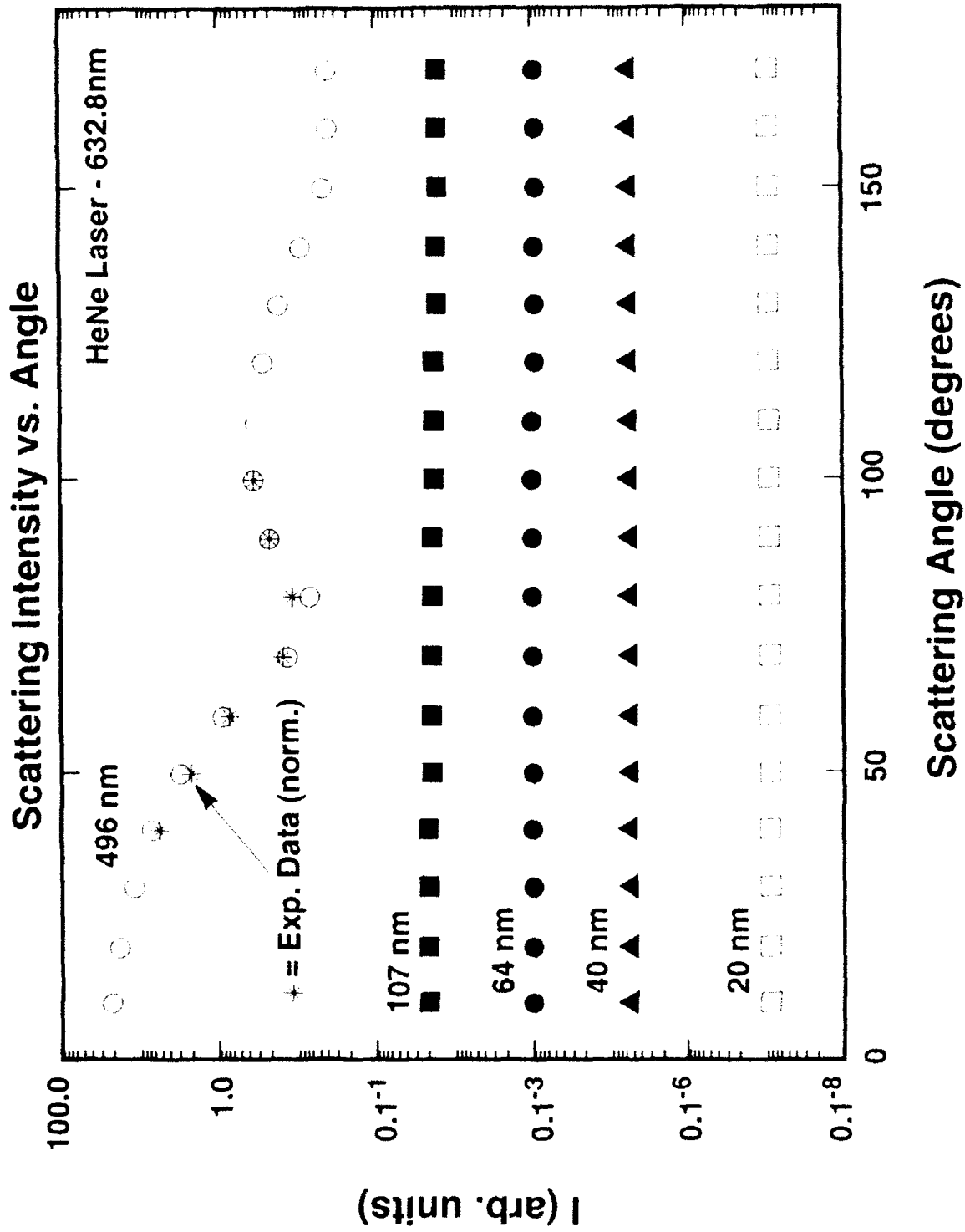


Figure 12 Mie intensity parameters versus scattering angle for HeNe laser source and particle diameters corresponding to available polystyrene standard spheres. Asterisks represent experimentally determined intensities normalized to the calculated value at a scattering angle of 90 degrees

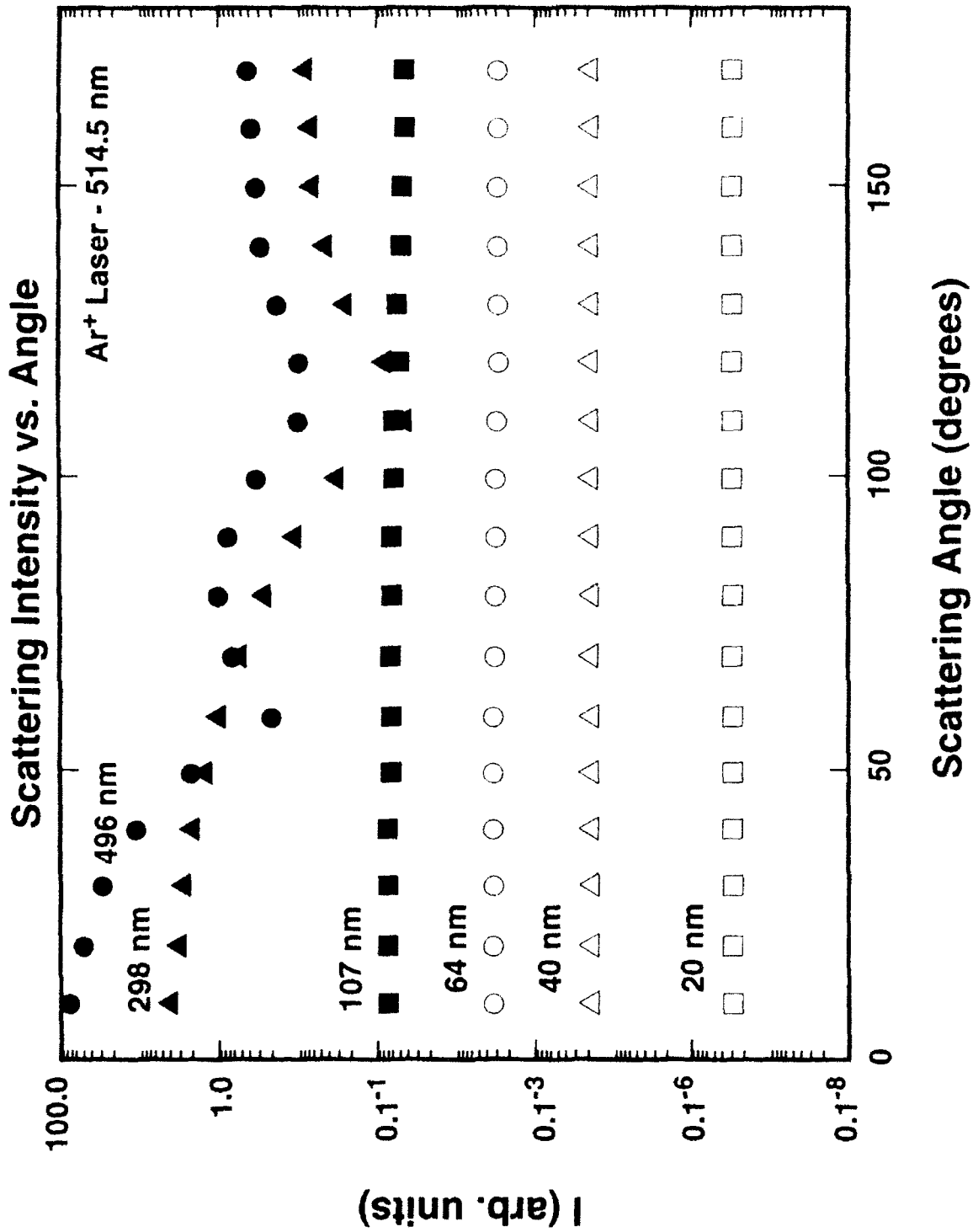


Figure 13. Mie intensity parameters versus scattering angle for Argon ion laser source and particle diameters corresponding to available polystyrene standard spheres

then bubbling oxygen through the sample for 15 minutes. Recently, we have performed PCS tests on samples prepared by filtering through a much finer filter (0.2 micron). As indicated below, preliminary experimental results suggest that the filtering step does affect the onset of particle formation in the heated fuel. All tests have been performed at atmospheric pressure.

In real-time, *in situ* studies of heated fuels, two principal effects have been monitored as a function of temperature: (1) changes in the intensity of scattered laser light and (2) the evolution of the autocorrelation function. At temperatures as low as 80°C, a significant increase in the intensity of scattered light has been observed. Very large gains in signal intensity have been seen at temperatures approaching 150°C. Typically, at least some of the enhanced scattering intensity is "permanent," i.e., it persists when the fuel cools to room temperature. This effect occurs in conjunction with particle formation in the sample and deserves more detailed analysis.

As discussed previously, two test cells have been used during these tests: a 25-ml cylindrical vial (with fairly large temperature gradients) and a 3.8-cm cube (much better temperature uniformity). In the cylindrical cell, *in situ* measurements on the Jet A-1 fuel were performed by heating samples to center temperatures in the range of 90-150°C and maintaining them near the nominal value for 4 hours. Temperatures at the surface layer were consistently monitored as well. Under these experimental conditions, the scattering signal observed in real time appeared to be primarily influenced by particle formation processes occurring in the vicinity of the hotter surface layer. In addition, the surface layer processes were evidently a major factor in subsequent room temperature measurements on the thermally stressed fuel. Repeated PCS measurements under these conditions indicated that consistent values could be obtained.

Although the temperature gradients that were present during the heating tests complicated interpretation of the experiments, definite trends in mean particle size vs. stress temperature and exposure time were observed. As mentioned previously, Figure 9 contains plots of autocorrelation functions obtained in room temperature measurements on thermally stressed fuel. The increasingly long decay rate of the correlation function with increasing temperature indicates that the mean particle size is increasing. Size distributions and mean particle diameters obtained from data of this type are shown in Figure 14. Size distributions observed in real-time measurements on the heated fuel are shown in Figure 15. The plots in Figures 14 and 15 represent "chosen fits" of the CONTIN Laplace inversion routine. Similar results were obtained with the other size distribution analysis algorithms.

Three Jet A-1 fuel samples heated to nominal temperatures of 90-110°C (maximum temperatures of 103°C, 122°C, and 124°C, respectively) did not exhibit significant correlation either in real-time or in subsequent room-

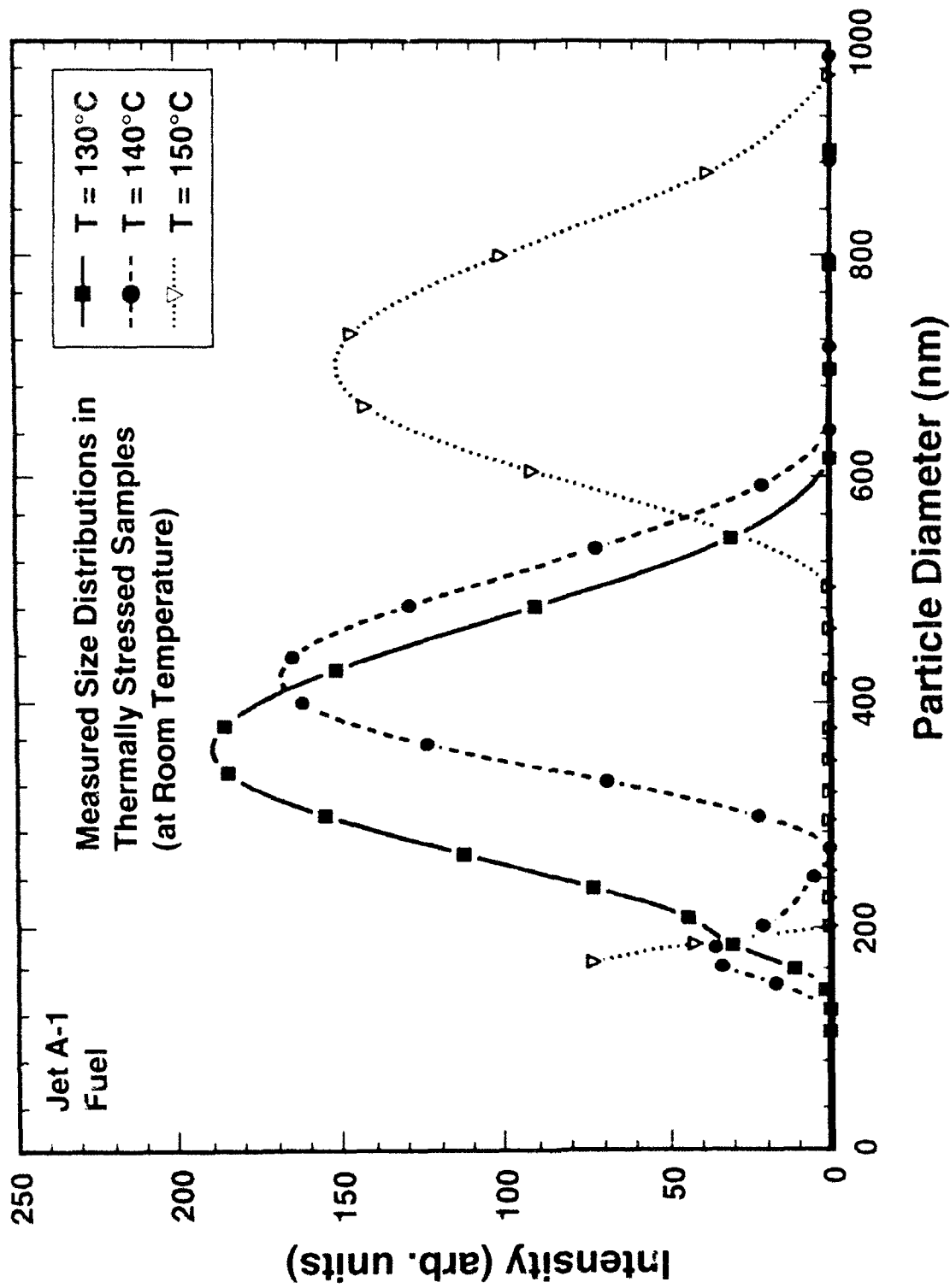


Figure 14. Measured particle size distributions for three Jet A-1 samples heated to different temperatures. PCS was performed at room temperature. Particle size distributions determined using CONTIN analysis routine.

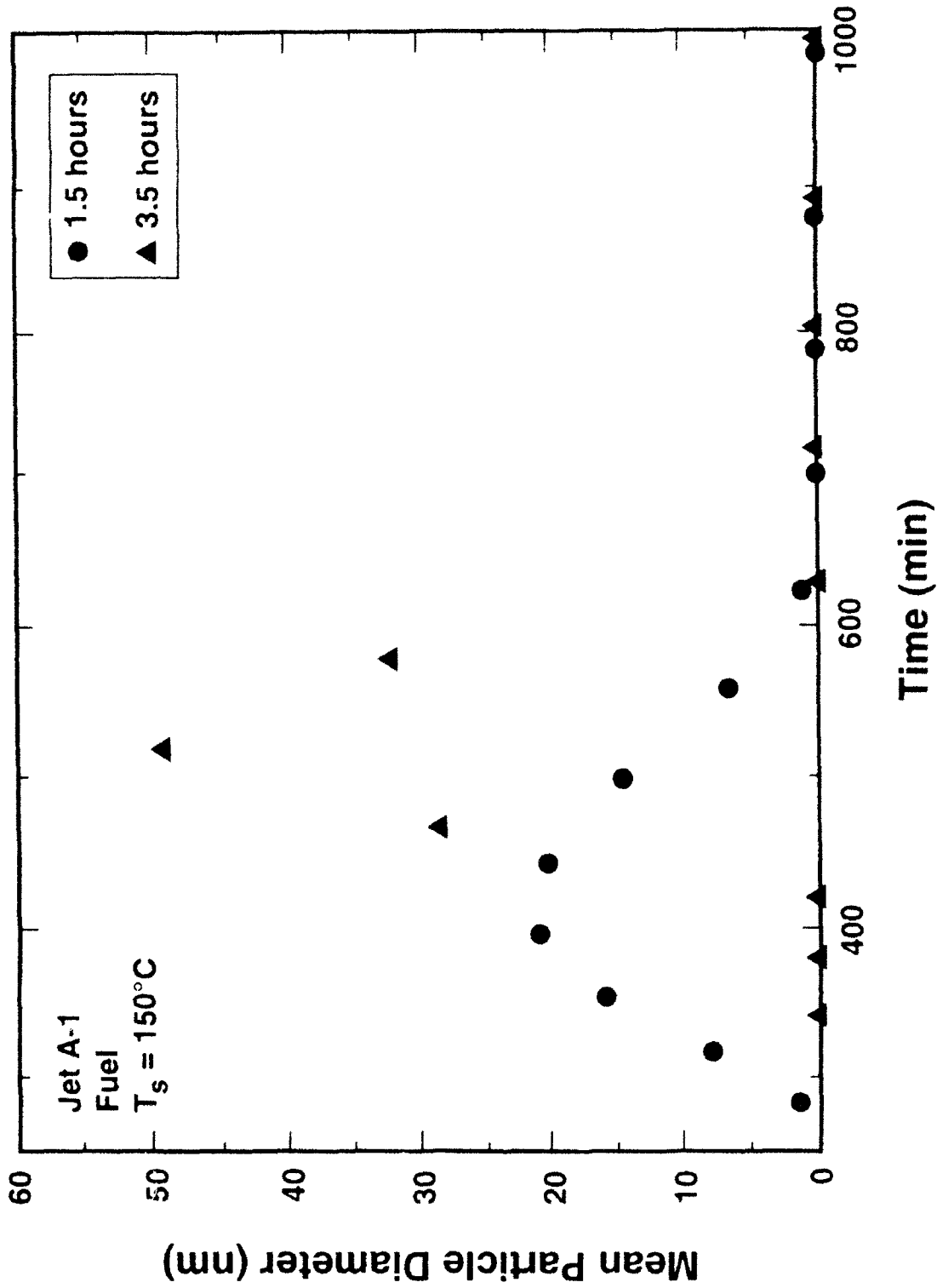


Figure 15. Real-time measurements of particle size distributions during 150 C heating of Jet A-1
 Particle size distributions determined using CONTIN analysis routine

temperature measurements. A similar lack of correlation was seen when a more intense (approximately 300 mW) argon ion laser was used as the optical source. This negative result could arise from effects including (1) a low concentration of scattering particles, (2) a very small mean particle diameter and (3) an ill-defined distribution of particle sizes. Any one or a combination of these effects could result in a scattering signal that, for reasonable analysis times, lies below the detection limit of the present system.

Definite evidence of particle formation was first observed in the sample heated to a nominal temperature of 120°C (maximum temperature near 138°C). Real-time measurements on this sample produced no correlation; however, a weak correlation was obtained after the sample cooled to room temperature (cf. Figure 9). Analysis of this "noisy" signal indicated mean particle diameters in the range of 60-100 nm. Clearly, the timescale for formation of a significant concentration of particles under these conditions is fairly long (i.e., hours).

Compared to the previous sample, results obtained from the sample heated to a center temperature of 130°C (maximum temperature near 164°C) demonstrate that particle formation accelerates rapidly over a fairly narrow temperature range. Evidence of substantial particle generation (an obvious increase in the intensity and the appearance of well-defined correlation in the scattering signal) was seen in the 130°C sample after approximately 1 hour at temperature. The visual appearance of the light scattering as well as fluctuations in the scattering intensity were consistent with particle formation near the surface layer coupled with mass transport into the laser field by means of convective flow. Room-temperature measurements on the cooled sample produced a smooth correlation that corresponds to a mean particle diameter near 350 nm.

PCS results on samples heated to 140°C and 150°C (168°C and 183°C maximum temperatures, respectively) were very similar. As expected, particle formation occurred more rapidly with increasing temperature. Figure 14 shows that the "final" mean particle size (measured at room temperature) increased as a function of stress temperature, as well. Both samples exhibited correlations that suggest the presence of a second, smaller component (100-175 nm diameter) in the size distribution (cf. Figure 14). This apparent bimodal distribution likely indicates slow formation of small particles in the bulk fluid in addition to the generation of large particles near the surface. The mean size of the smaller component is consistent with the 100-nm particles generated in the 138°C surface layer of the 120°C (nominal) sample. Growth in the mean particle diameter as a function of exposure time is indicated in the real-time results given in Figure 15. After heating, the 140°C and 150°C samples exhibited a slight discoloration not observed in the samples tested at lower temperatures. The data indicate that the particle diameters measured at room temperature are larger than those measured at elevated temperatures. This trend was confirmed in tests in

which good temperature uniformity was maintained (see discussion below). This effect may be due to agglomeration occurring as the sample cools, indicating that real-time measurements are required.

For PCS testing in the 3.8-cm-cube test cell, fuel samples were heated to temperatures in the range of 130-160°C and maintained near the nominal value for up to 4 hours. With the improved temperature uniformity in this configuration, clear trends in particle size and scattering intensity are observed. Real-time measurements of mean particle diameter for Jet A-1 fuel heated to 160°C are shown in Figure 16. The mean particle size increases with increasing exposure time at fixed temperature and then stabilizes at a larger value as the fuel sample cools to room temperature. These results clearly illustrate the need for real-time, *in situ* particle measurements. The time-dependent growth in particle diameter can not be determined from posttest analysis alone.

Comparing results from PCS and static light scattering measurements, it is apparent that the fuel samples heated to 150°C and 160°C in the quartz cell exhibit fairly similar behavior. As expected, particle formation occurs more rapidly with increasing temperature. Figure 17 shows the increase in scattering intensity with time for these two stress temperatures. The sample heated to 150°C produced a slow increase in scattering intensity until the fuel reached the setpoint temperature. After this time, the scattering intensity began to increase rapidly. The increased scattering intensity could be due to increased particle size, increased numbers of particles present, or a combination of the two mechanisms. The sample heated to 160°C showed a similar slow increase in scattering intensity up to the setpoint temperature. Upon reaching this temperature, the scattering intensity rose very rapidly at first and then began to drop until the heating was terminated. The scattering intensity then increased as the fuel cooled back to room temperature. A plausible explanation for this behavior is given in Figure 18, which shows the calculated scattering intensity as a function of particle diameter for spherical particles of several reasonable values of refractive index. The program used for these calculations is the simple adaptation of the FORTRAN routine "CALLBH" (Bohren and Huffman, 1983). It is interesting that the scattering intensity exhibits a maximum for particle diameters in the range of 280-340 nm (depending on the refractive index) and drops substantially as particle size increases to 400-450 nm. The mean particle diameters determined by PCS for the 160°C case (cf. Figure 16) indicate that the observed drop in scattering intensity is likely caused by particle diameters achieving critical values in the 280-400 nm range. In contrast, the maximum mean particle diameter in the 150°C sample (approximately 270 nm) never reached the critical value for a drop in scattering intensity. Hence, the scattering intensity continuously increased during the test (cf. Figure 17). Precise correlation between the measured mean hydrodynamic diameters and the

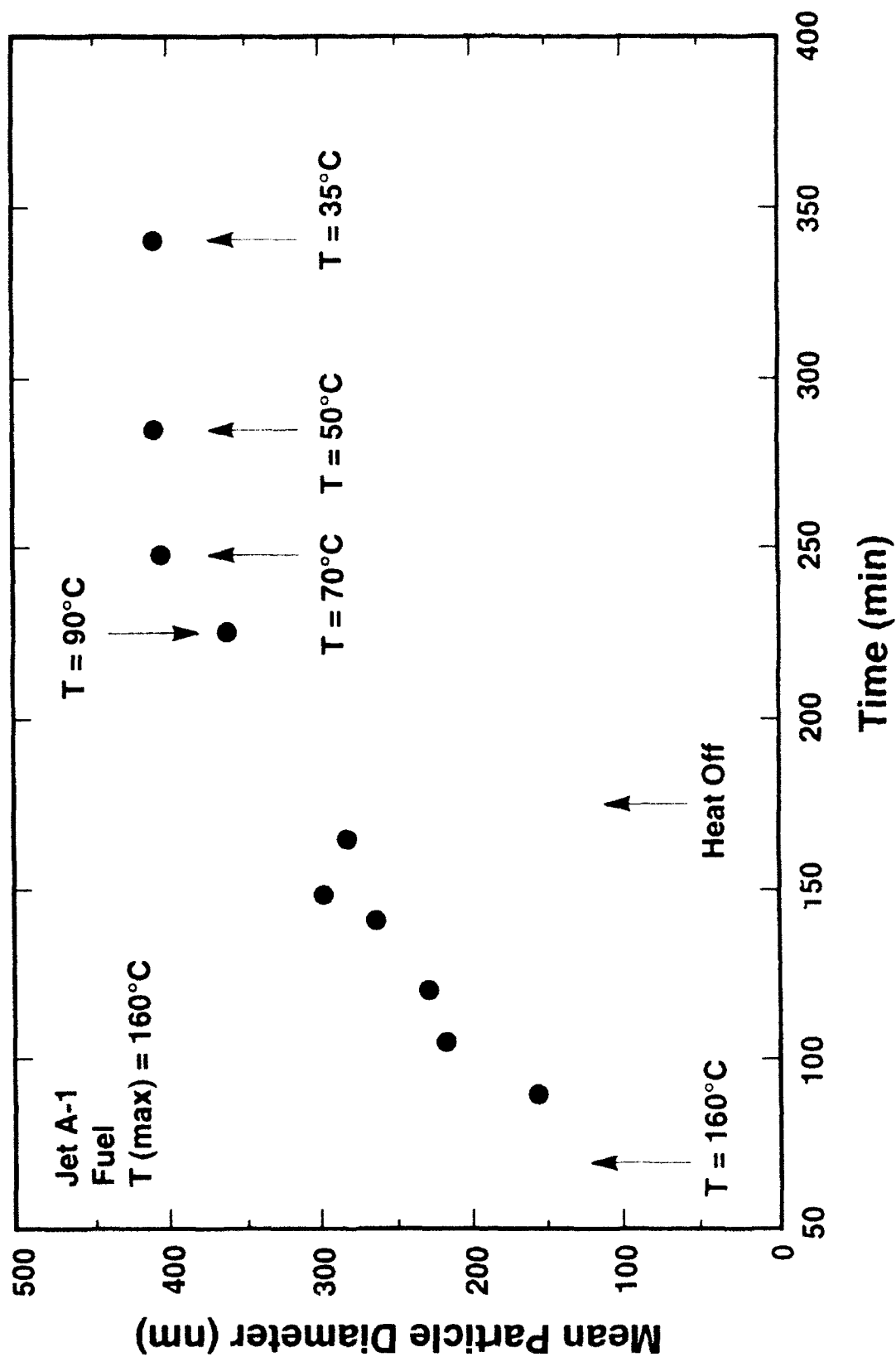


Figure 16 Real-time measurements of mean particle size during 160°C heating of Jet A-1 Particle size determined using CONTIN analysis routine

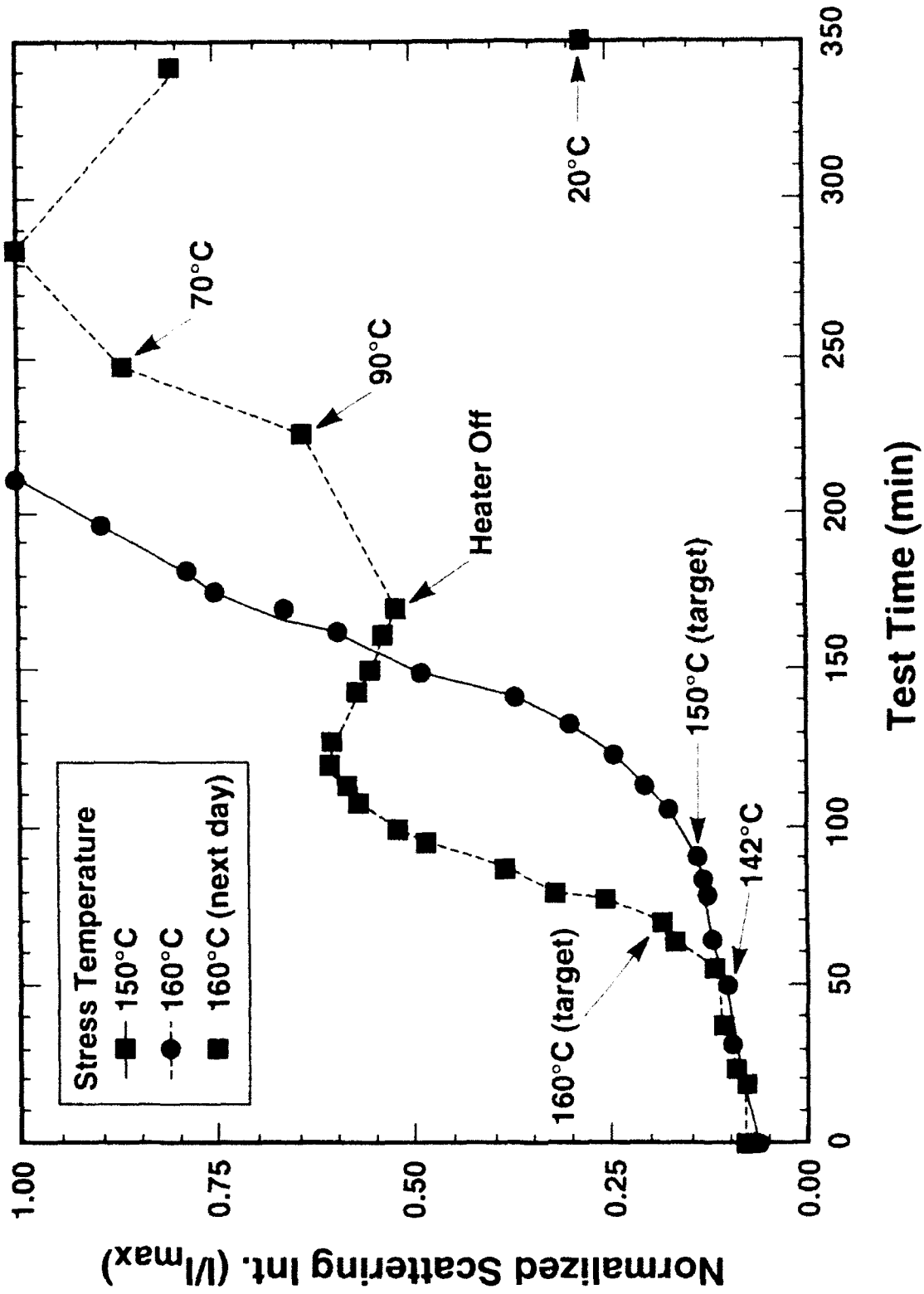


Figure 17. Scattering intensity (normalized to the maximum value) as a function of test time for Jet A-1 samples heated to 150°C and 160°C

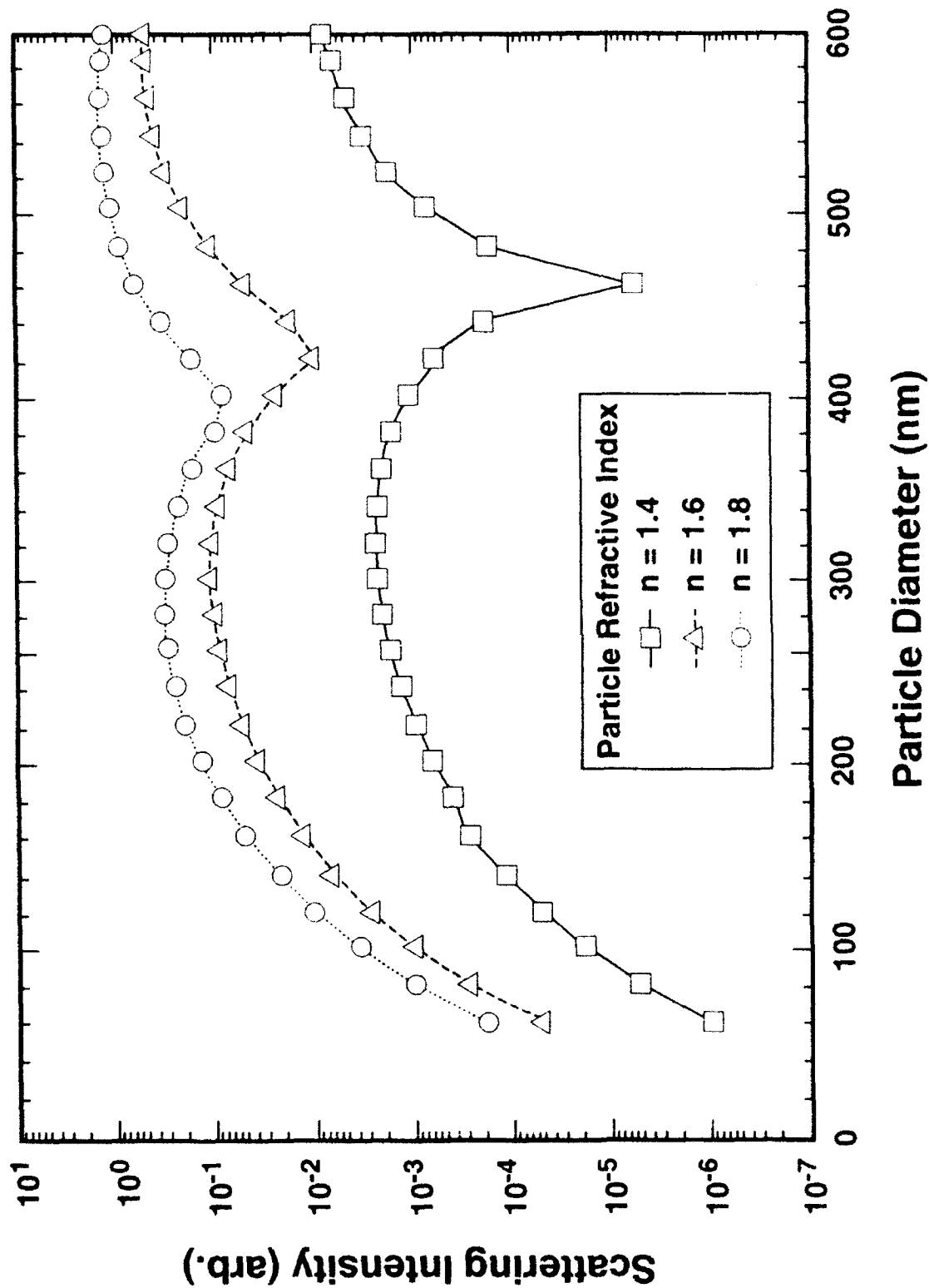


Figure 18. Calculated scattering intensity (at 90° scattering angle) as a function of particle diameter for various particle refractive indices. Illuminating wavelength is 632.8 nm. Computations made using modified version of the program CALLBH (Bohren and Huffman, 1983).

critical diameters shown in Figure 18 should not be expected, since the particle shapes and refractive indices are as yet unknown.

Consistent results are obtained in PCS tests using the quartz cube and cylindrical sample cell when the mean particle diameter is associated with the maximum temperature (i.e., upper surface layer) achieved in the latter device. Figure 19 combines the posttest (room temperature) results for mean particle diameter as a function of exposure temperature. No correlation is observed for stress temperatures below 138°C, either in real-time or in subsequent room-temperature measurements. Above 138°C, the mean particle diameter increases dramatically as a function of exposure temperature. As the exposure temperature is increased to >180°C, very large particles (>700-nm diameter) are formed. Measurements of the scattered light intensity as a function of scattering angle have also been performed on the stressed fuel samples. The particle sizes indicated by these measurements are generally consistent with the PCS results. As an additional posttest analysis procedure, we are now routinely performing an infrared absorption scan of a small portion (0.025-mm path length) of the heated fuel samples. Consistent with previous results obtained in fuels stressed in a mildly oxidative environment (Klavetter et al., 1992), we have observed only minute changes in the absorption spectrum of posttest samples examined to date.

The most recent PCS data indicate that careful attention must be given to the effects of sample preparation on particle formation. In these tests, the quartz cubic test cell has been rigorously cleaned in an ultrasonic bath, and the fuel has been filtered through a 0.2-micron filter. Visual examination of the scattered light intensity prior to heating indicated that the samples were extremely clean, i.e., dust-free. When heated to 150-160°C, these samples exhibited significantly slower particle formation than all of the other samples tested to date. Tests are currently underway to quantify this behavior.

We have also initiated tests to determine the detection sensitivity of the PCS system under "optimal" conditions (i.e., for a monomodal distribution of spherical particles). Monodisperse solutions of 20- and 105-nm diameter spheres in known concentration were prepared by carefully weighing a drop of the aqueous suspension (as supplied by Duke Scientific) into 10 ml of filtered H₂O followed by further dilution in decade increments. For the 105-nm spheres, with a 35 mW HeNe laser as the optical source, solutions containing 8×10^9 particles/cm³ and 8×10^8 particles/cm³ exhibited intense and strong scattering, respectively. Accurate sizing was obtained in both cases. Weak scattering was obtained from a sample containing 8×10^7 particles/cm³; however, fairly accurate sizing (in part limited by dust in the sample) was achieved. These results suggest that the PCS system, as presently configured, can easily discern a relatively simple distribution of particles (about a mean diameter near 100 nm) in the range of 10's of nanograms per ml. The results for 20 nm spheres were consistent with the expected sixth-power dependence of scattering intensity on particle diameter (i.e.,

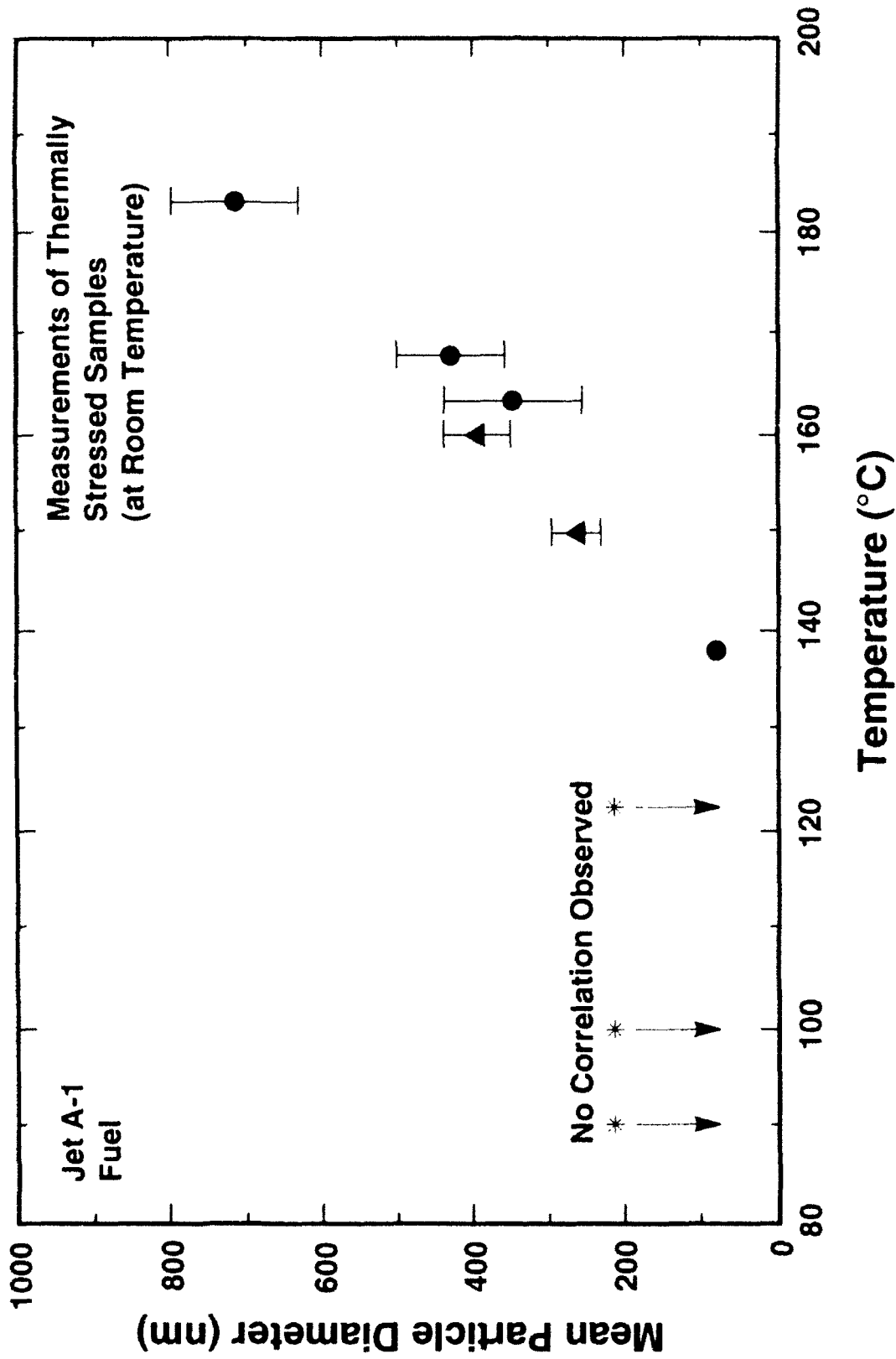


Figure 19. Mean particle diameter (as determined by PCS) versus thermal stress temperature. Solid triangles represent data obtained in quartz sample cell. Solid circles correspond to data obtained in cylindrical test cell. Vertical bars indicate the width (one standard deviation) of the particle size distribution as determined by the CONTIN analysis routine.

much higher concentrations are needed for detection). With guidance from the available Mie scattering program, we intend to examine other factors affecting the detection sensitivity of the PCS system, including different particle sizes, laser wavelength and intensity, scattering angle, and different configurations of focusing and collection optics. More complex distributions of particle sizes will be addressed by tests on carefully controlled mixtures of the "Nanosphere" standards. Quantitative analysis of the PCS detection sensitivity for particles formed in jet fuels should also be possible, given the necessary information regarding particle and medium refractive index as well as particle shape factors. Measurements of this type will be particularly valuable in tests involving the integration of PCS with the Quartz Crystal Microbalance (QCM) mass sensor.

4. PCS Summary and Conclusions

Photon correlation spectroscopy has proved to be a valuable tool for both real-time and posttest analysis of thermally stressed jet fuels. *In situ* measurements have shown that particle formation in Jet A-1 becomes evident at temperatures as low as 120°C, and that relatively large particles (200-800 nm mean hydrodynamic diameter) are formed at temperatures less than 200°C. Particle size increases systematically with increasing stress temperature over the range 135-180°C. Real-time measurements indicate that the mean particle diameter increases with increased exposure time at fixed temperature. Particle diameters measured at room temperature are larger than those measured at elevated temperatures, indicating the need for real-time measurements.

Future experiments will concentrate on the role of sample preparation and oxidation state on particle formation. In addition, the response of new fuels and additives will be compared to the existing data on Jet A-1 and JP-8. We are currently working with Prof. Rob Hoffman, New Mexico State University, to determine a standard test procedure for chemical analysis of the fuel prior to PCS testing, to ensure that the fuel to be tested is consistent from test-to-test. He will also be assisting in interpretation of PCS data, especially in regard to determining particle concentrations and kinetic mechanisms. Plans are underway to integrate and compare the PCS and QCM techniques.

C. SOLIDS CHARACTERIZATION STUDIES

During this past year, we have carried out selective analyses on material deposited during controlled fuel stressing experiments (performed by Tim Edwards at Wright Laboratory, Wright-Patterson AFB) which varied the time that flowing jet fuel was in contact with instrumented stainless steel tubes. The purpose of these studies was to collect data which would help understand the mechanisms of solids formation. The tubes that have been studied were identified as 9/91-2 (Jet A-1 2747, low sulfur, 18-hour run), 9/91-6 (Jet A 2827,

high sulfur, 18-hour run), and 9/91-9 (Jet A 2827, high sulfur, 6-hour run). Temperature profiles were provided to us along with the tubes. Solids deposit (carbon) profiles from similar runs were also provided by Tim Edwards. The data obtained from our study have been correlated with the temperature and carbon profiles. The end of each tube near the fluid inlet was designated as zero inches for the described studies and distance along the tubes measured in the direction of flow. A second study that was carried out during the past year was the measurement of the thickness of material deposited on quartz micro-balances that have been exposed to flowing, heated jet fuel. These measurements were used as an additional calibration of the micro-balances.

1. Heated Tube Studies

In the as-received condition, the tubes were approximately 18 inches long and 1/4-inch diameter. Our first action was to cut the tubes into approximately 6-inch lengths and then cut them lengthwise to expose the interior. All cutting was carried out dry using a slow speed saw. After sectioning, the tubes were photographed using an optical microscope. Analyses of selected areas in the tubes was carried out using scanning electron microscopy (SEM), SEM/energy dispersive analysis (EDA), micro X-ray fluorescence, Auger electron spectroscopy (AES), secondary ion mass spectroscopy (SIMS), and Raman spectroscopy.

Optical photographs of sections at approximately 5 inches from the inlet side of the three tubes are shown in Figures 20a, 20b, and 20c. For comparison, the thick deposit found in an afterburner augmentor is shown in Figure 21. The similarity between these deposits is quite striking. In Figure 20, the commencement of the dark, heavy deposit region is clearly visible and coincides with the change in phase of the fuel from liquid to vapor as previously reported by Edwards (1992). This region is followed by a dark area where the amount of the deposit is noticeably less. It is clear from Figure 20 that the heaviest deposit occurs in the case of high sulfur, 18 hours (20c), followed by high sulfur, 6 hours (20b). The smallest deposit occurs for the low sulfur 18-hour run (20a). In this case, the major deposit in the phase change region appears more as a thick oil or tar than a "solid." These qualitative observations are in good agreement with the quantitative measurements provided by Wright Laboratory of the mass of the carbon deposit as a function of position (see for example Figure 22).

We have carried out micro X-ray fluorescence measurements to determine the sulfur variation as a function of position along the tube. The results for tubes 9/91-6 and 9/91-2 are shown in Figures 23a and 23b, respectively. In these figures, the S X-ray peak intensities are plotted as a function of distance along the tubes. In both cases we find a S peak in the region of the fuel phase change in good agreement with the carbon deposit data (Figure 22). The peak in the S intensity from tube 9/91-2 is about an order of magnitude lower than the peak

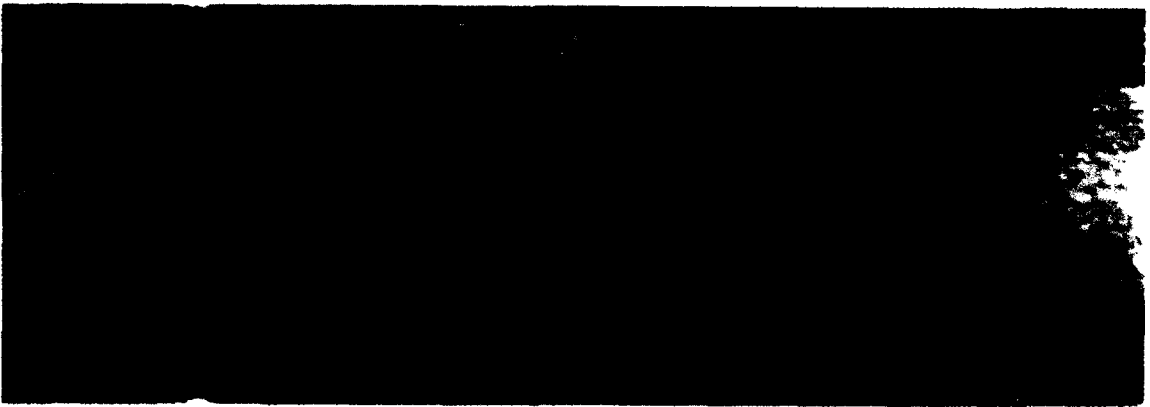
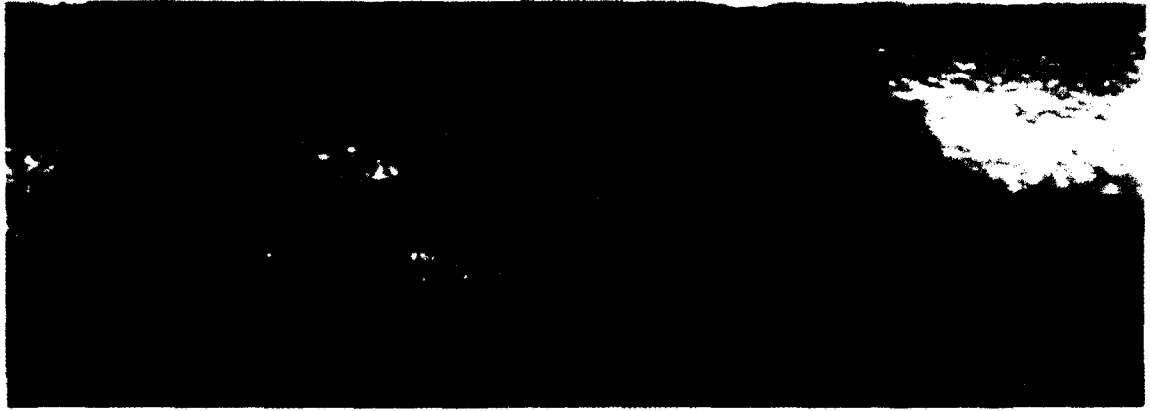


Figure 20. Optical photographs of the phase transition region from a) 9/91-2; b) 9/91-9; and c) 9/91-6



Figure 21. Solids deposit in an afterburner augmenter arm.

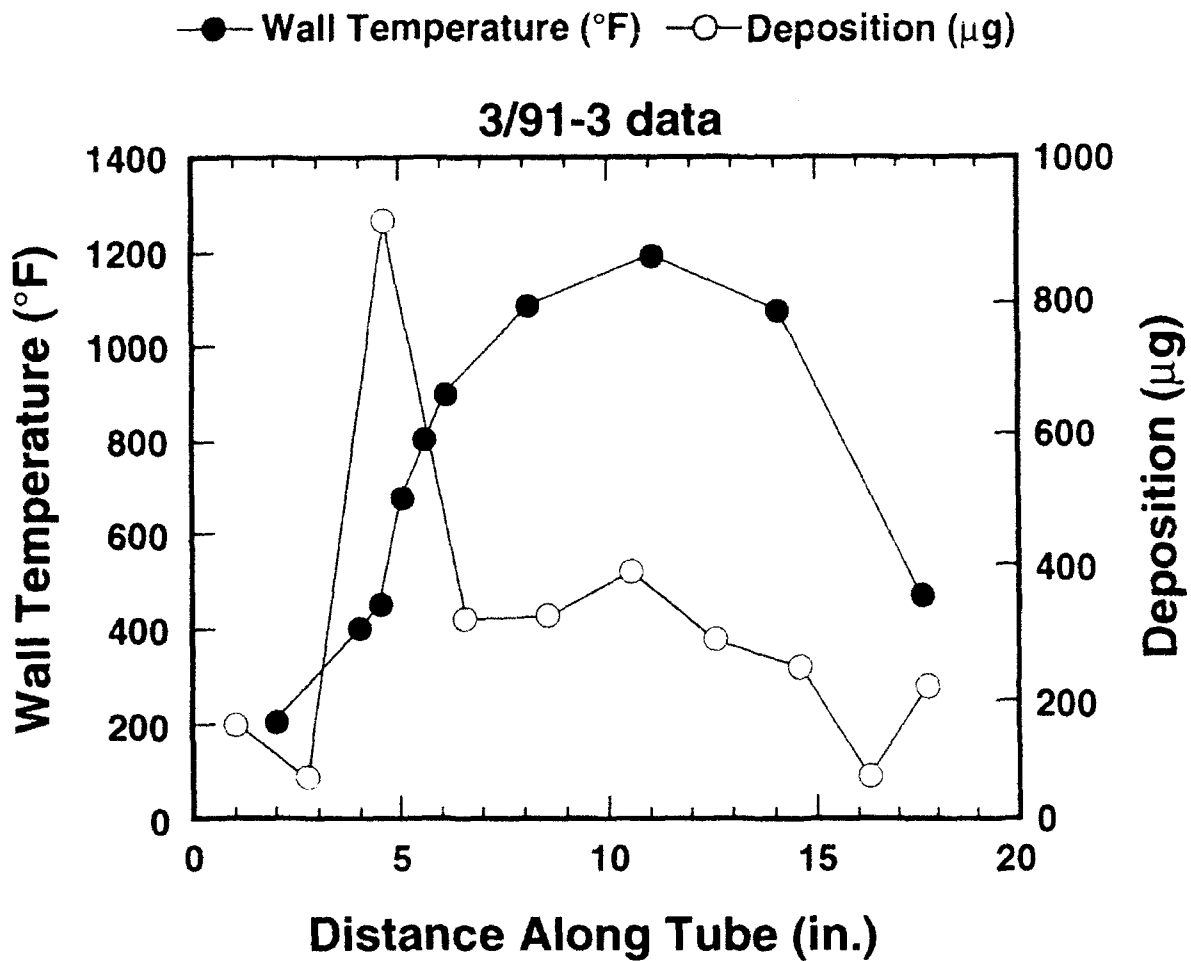


Figure 22. Typical wall temperature and carbon profile along test tube.

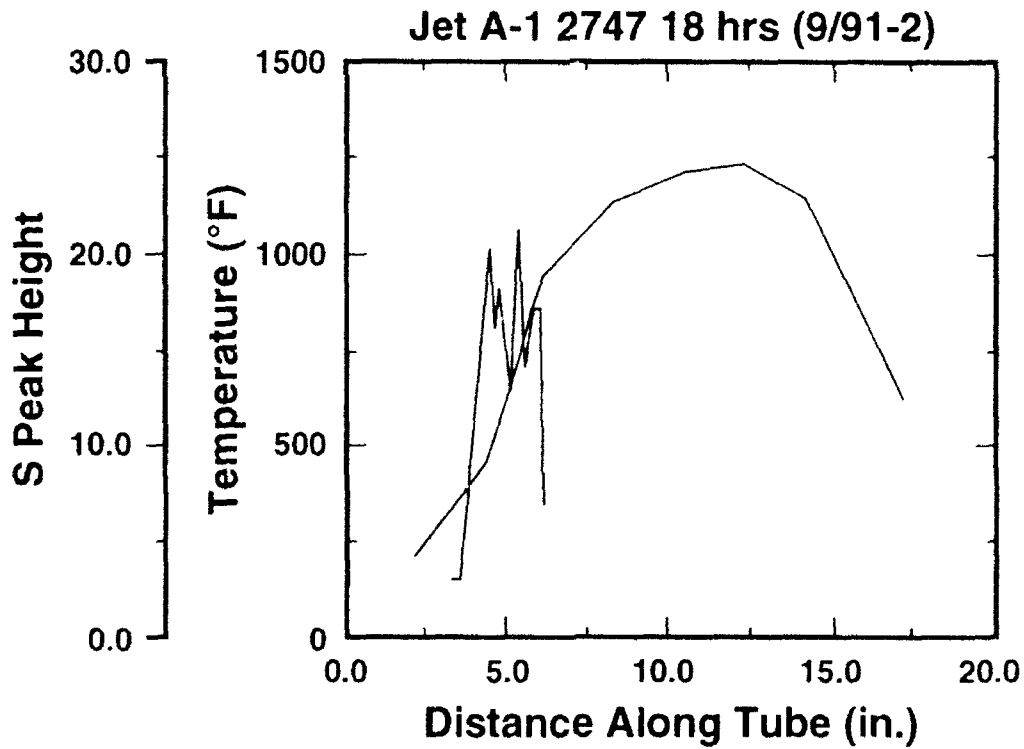
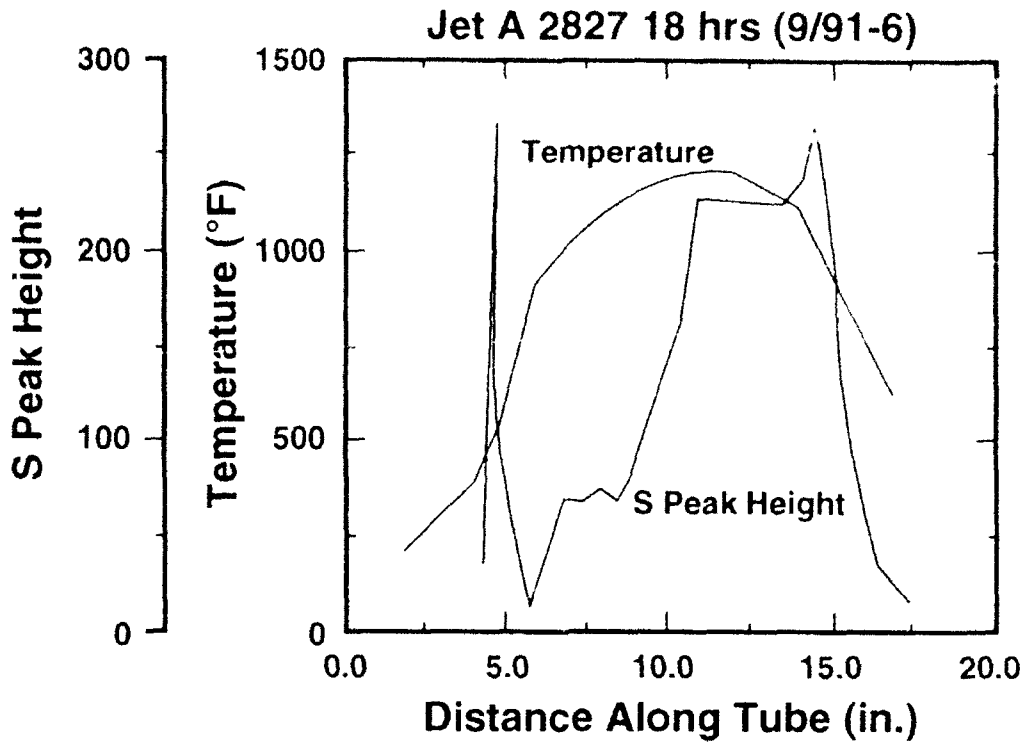


Figure 23. Sulfur peak height plotted as a function of distance along test tubes
 a) 9/91-6 and b) 9-91-2. The wall temperature is shown for comparison.

from tube 9/91-6. As noted above, the deposit in the phase change region of this sample is small. This is confirmed by the SEM and SEM/EDA data shown in Figure 24 where the major peaks are due to the stainless steel tube. No data were obtained in the high temperature region of 9/91-2 due to the low X-ray excited S signal. The intense, broad, S peak observed in the high temperature region of Figure 23a (9/91-6) is due to the limited sampling depth of the X-ray fluorescence technique and not due to a change in the S/C ratio in this area. This is illustrated in Figures 25 and 26. Figure 25 shows SEM and SEM/EDA data of the deposit in the phase change region while Figure 26 shows similar data from the high temperature region. In the phase change region the deposit is not porous (at least on this scale) and the SEM/EDA shows only S (this SEM/EDA system cannot detect C), indicating that the thickness of the deposit is greater than the sampling depth of the SEM/EDA technique. Since the entire thickness of the deposit is not being sampled, the S peak is representative of the total S in the depth sampled and not the total S in the deposit. In the high temperature region (Figure 26) the deposit is porous and the SEM/EDA spectrum shows large signals from the stainless steel tube in addition to the S. In this case we are sampling through the entire deposit and the S peak is representative of the total S in the deposit.

SEM and SEM/EDA data obtained from tube 9/91-9 (high sulfur, 6-hour sample) are shown in Figures 27 and 28. These data indicate the form of the deposits are very similar to those found for the 9/91-6 (high sulfur, 18-hour sample) i.e. in the phase transition region the deposit is solid while the high temperature region the deposit has a low density, filamentary appearance. The visual observations discussed above and the C deposit measurements made at Wright Laboratory indicate fewer deposits in the 6-hour sample than in the 18-hour sample. This is confirmed by the SEM/EDA data in Figure 27 which shows an iron peak from the stainless steel tube showing through the deposit.

The deposits found in the high temperature region from tubes 9/91-6 and 9/91-9 (Figure 26 and Figure 28) have an appearance very similar to carbon films that have been made by vapor phase growth (Wagner et al., 1992). In those cases, the amount of hydrogen present in the films had a dramatic effect on their growth and structure. Similar effects may be present in these films. Experiments to test this theory by measuring the hydrogen content of the carbon in the high temperature region vs. the transition are in progress.

In order to investigate the absolute concentration and variation of S and O in the deposit we have used Auger electron spectroscopy to analyze the near surface region. Figure 29 shows an Auger spectrum obtained from the high temperature region of tube 9/91-6. In addition to C, S and O peaks are observed. Analysis of this data and similar spectra obtained from adjacent areas indicates that the S and C content are on the order of 1-2 atomic percent. Figure 30 shows a plot of the S and O content as a function of position over a 15-mm area of the high

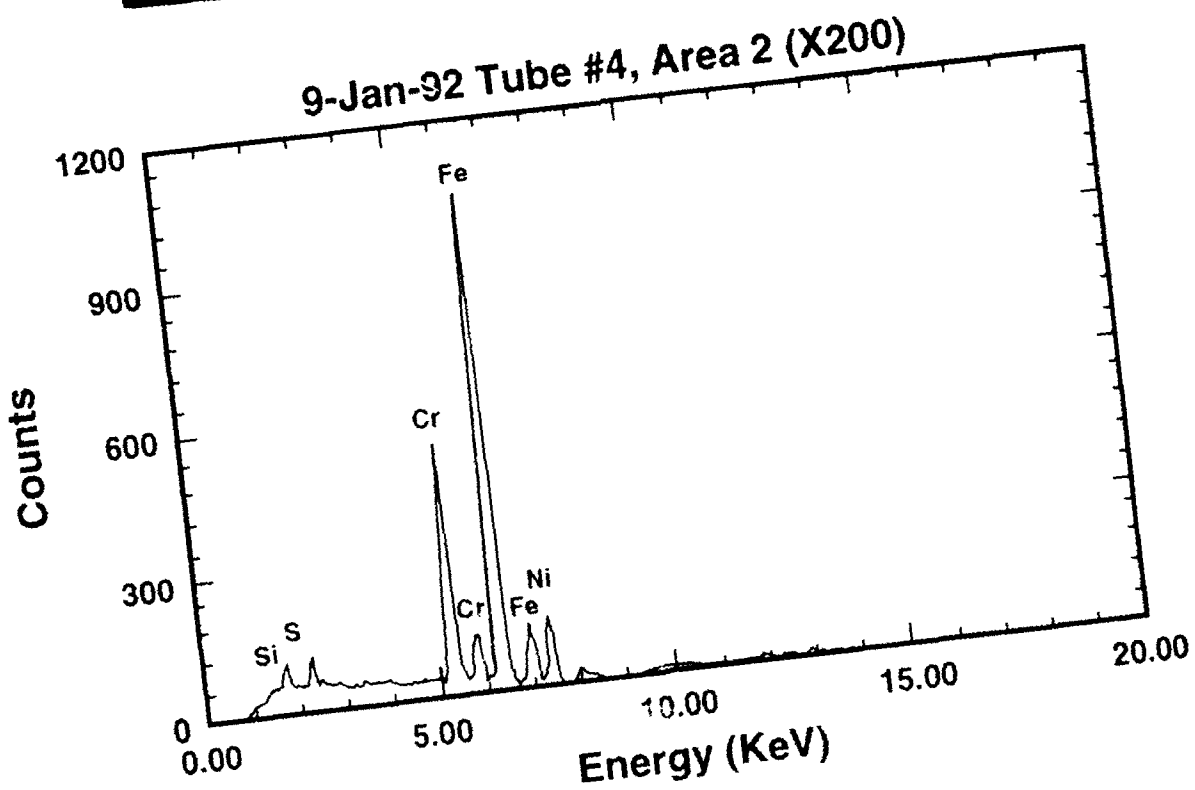
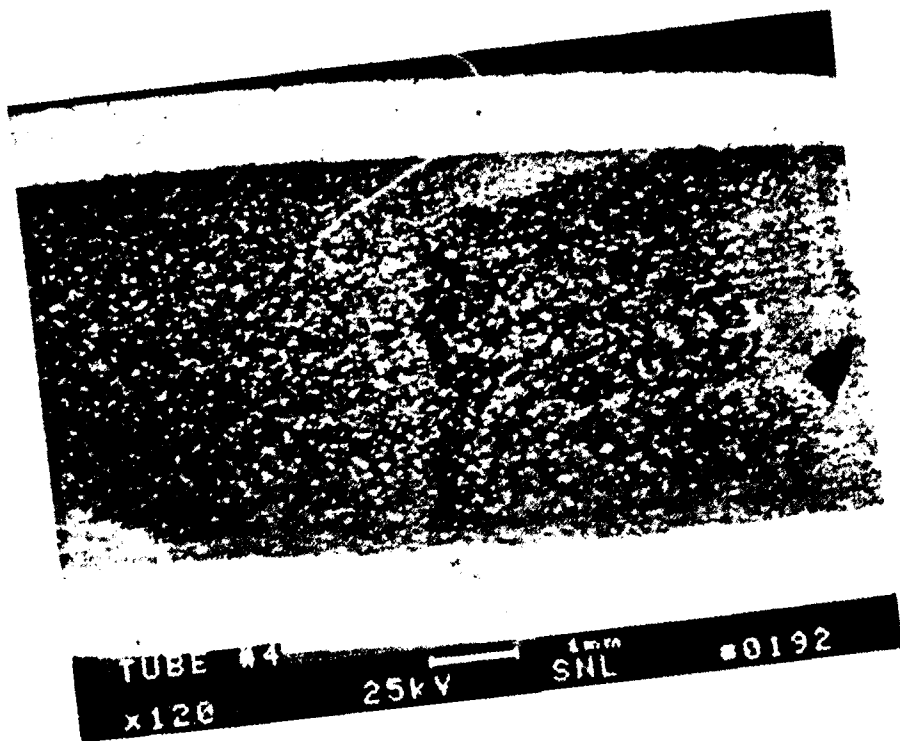


Figure 24. SEM and SEM/EDS spectra from the phase transition region of tube 9/91-2 (low sulfur fuel, 18-hour test).

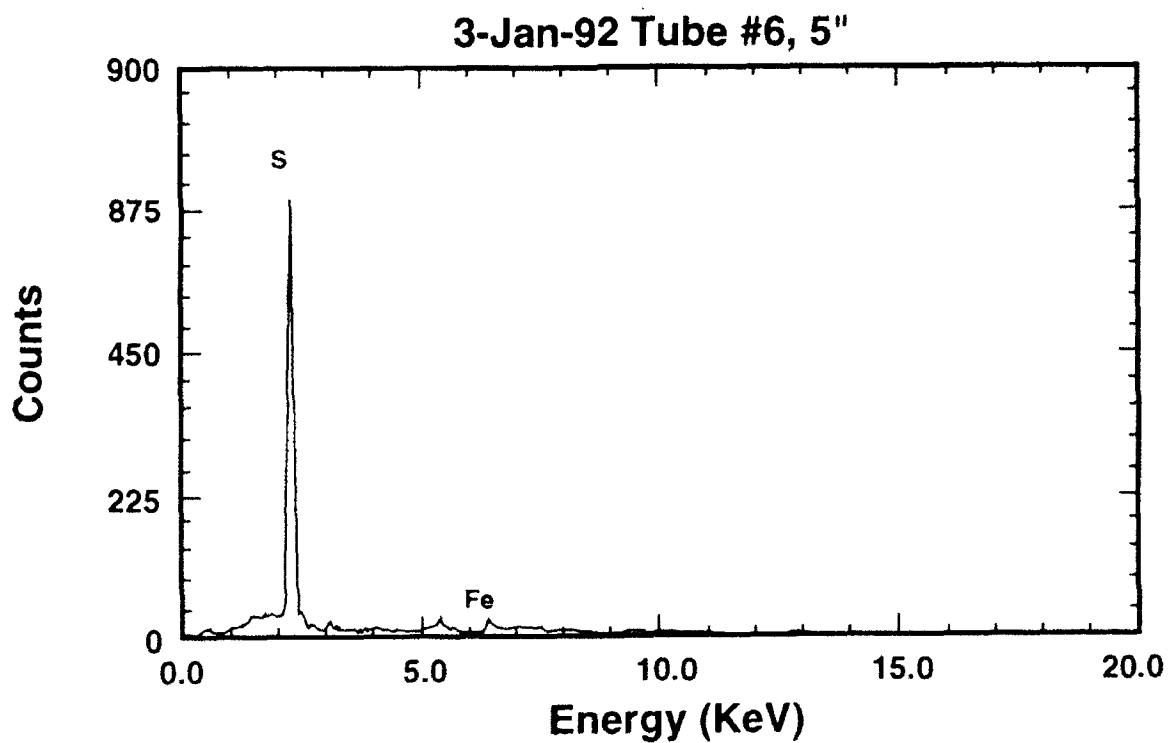
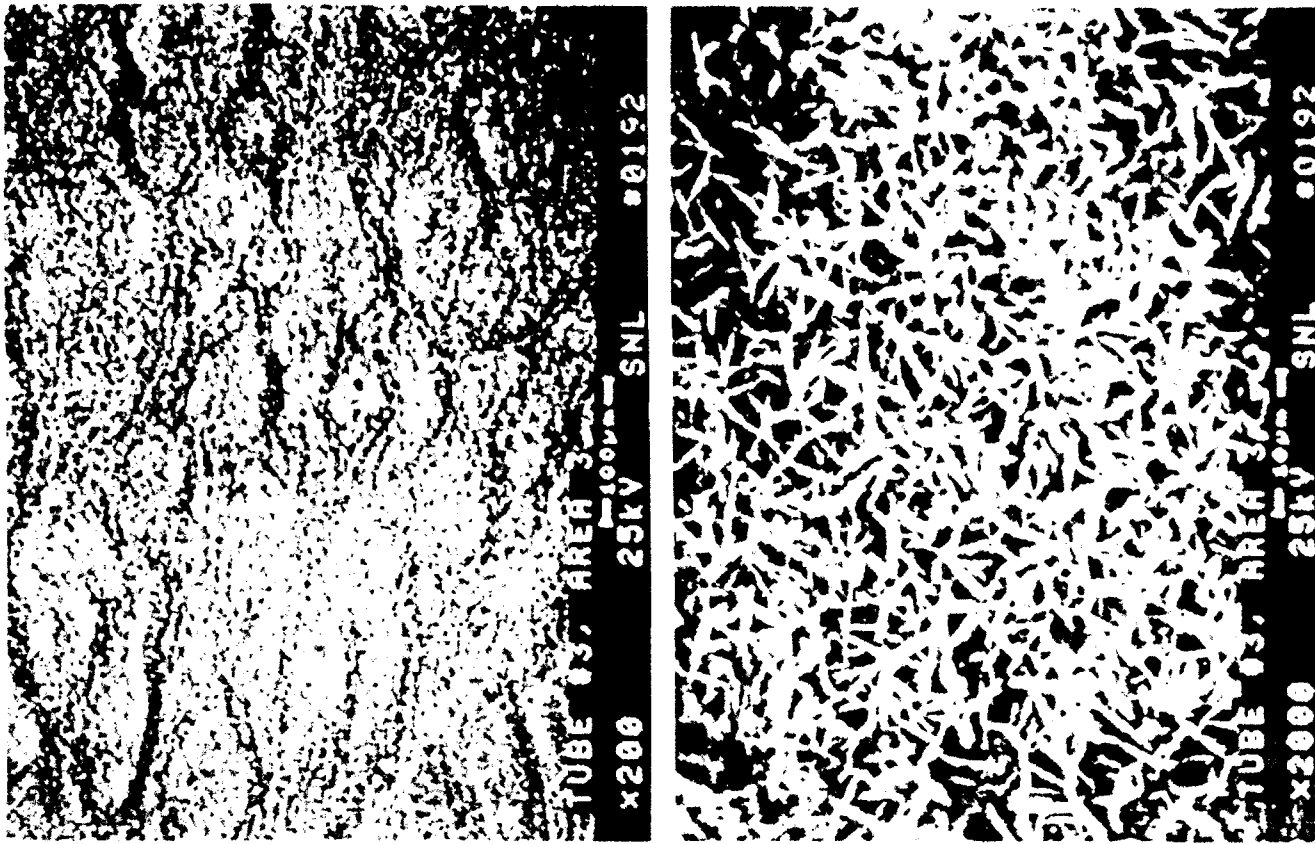


Figure 25. SEM and SEM/EDA spectra from the phase transition region of tube 9/91-6 (high sulfur fuel, 18-hour test).



8-Jan-92 Tube #3, Area 3 (200X)

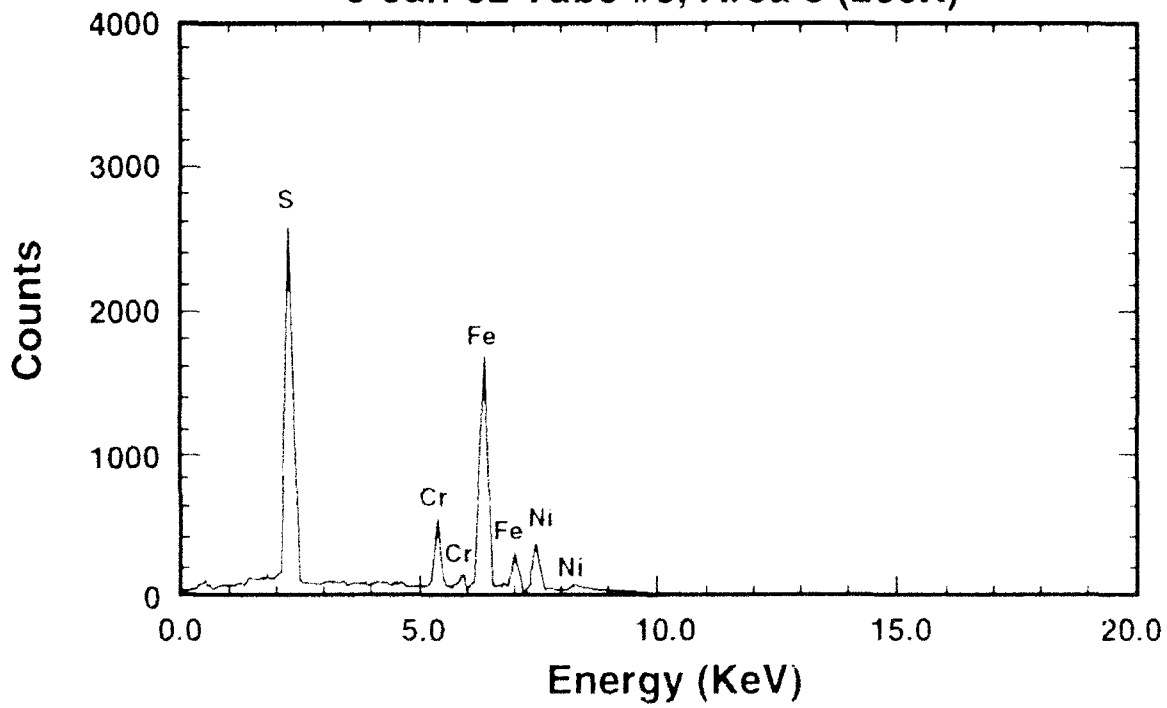
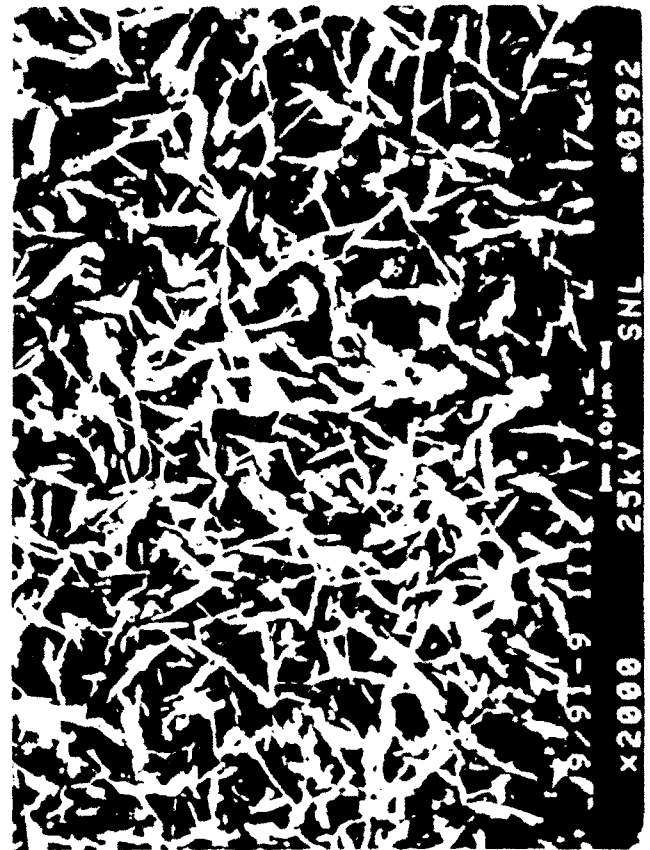
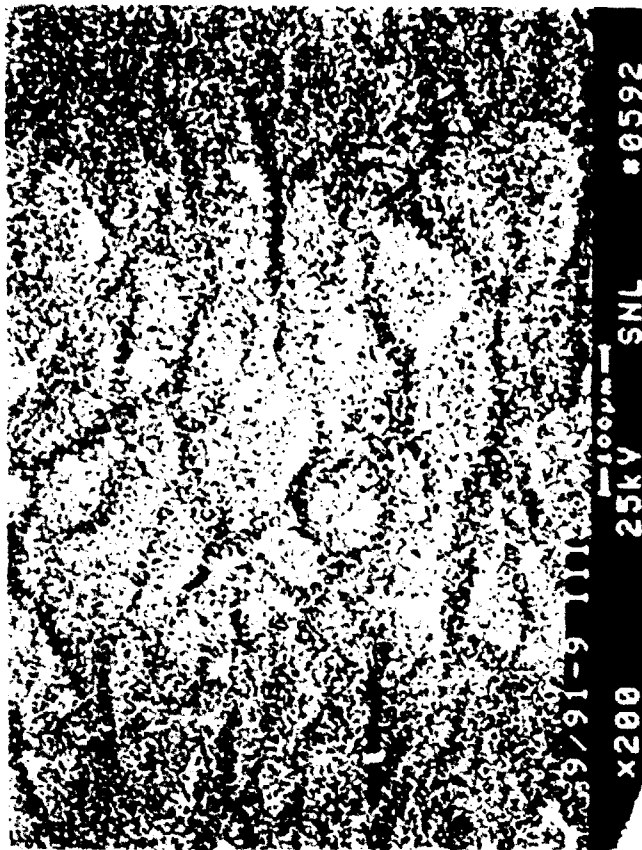


Figure 26 SEM and SEM EDA spectra from the high temperature (1000 F) region of tube 9-11-b (high sulfur fuel, 18-hour test)



18-May-92 9/91-9 III; Area Scan @ 200X

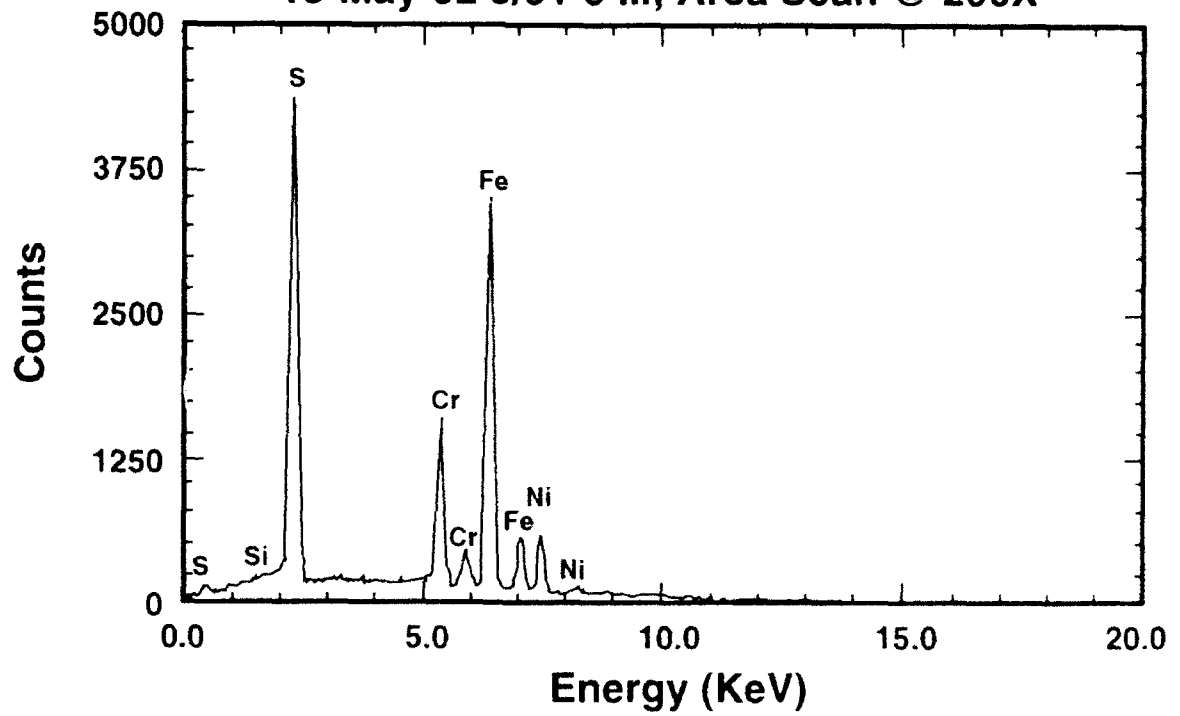


Figure 27. SEM and SEM/EDA spectra from the phase transition region of tube 9/91-9 (high sulfur fuel, 6-hour test).

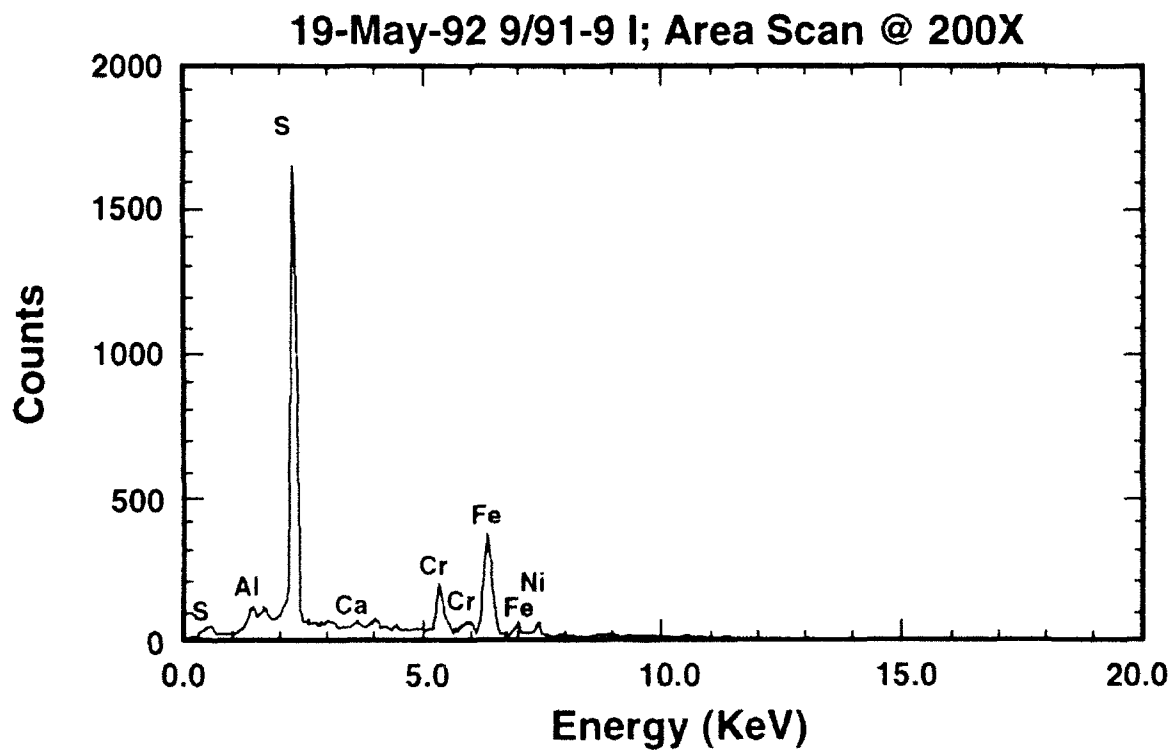
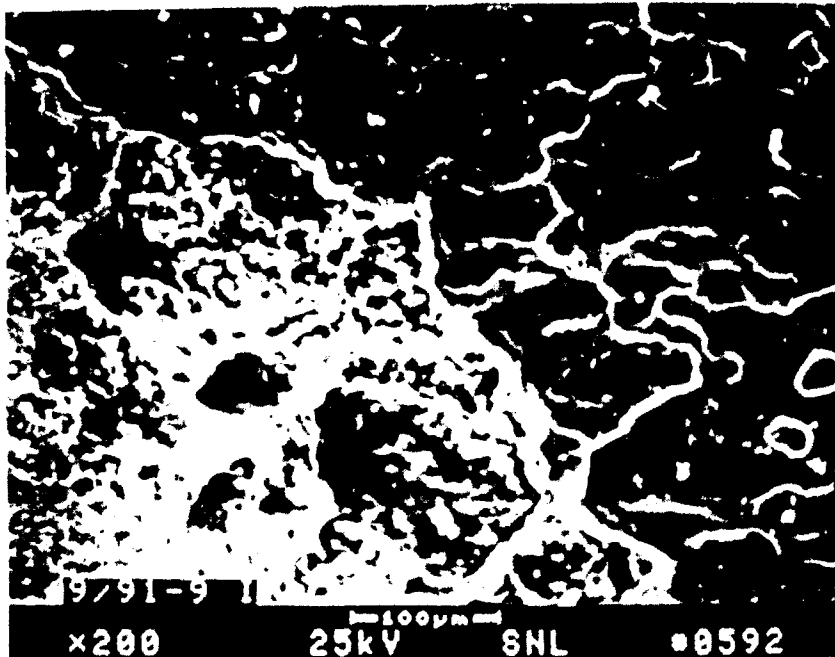


Figure 28. SEM and SEM/EDA spectra from the high temperature (1000°F) region of tube 9/91-9 (high sulfur fuel, 6-hour test).

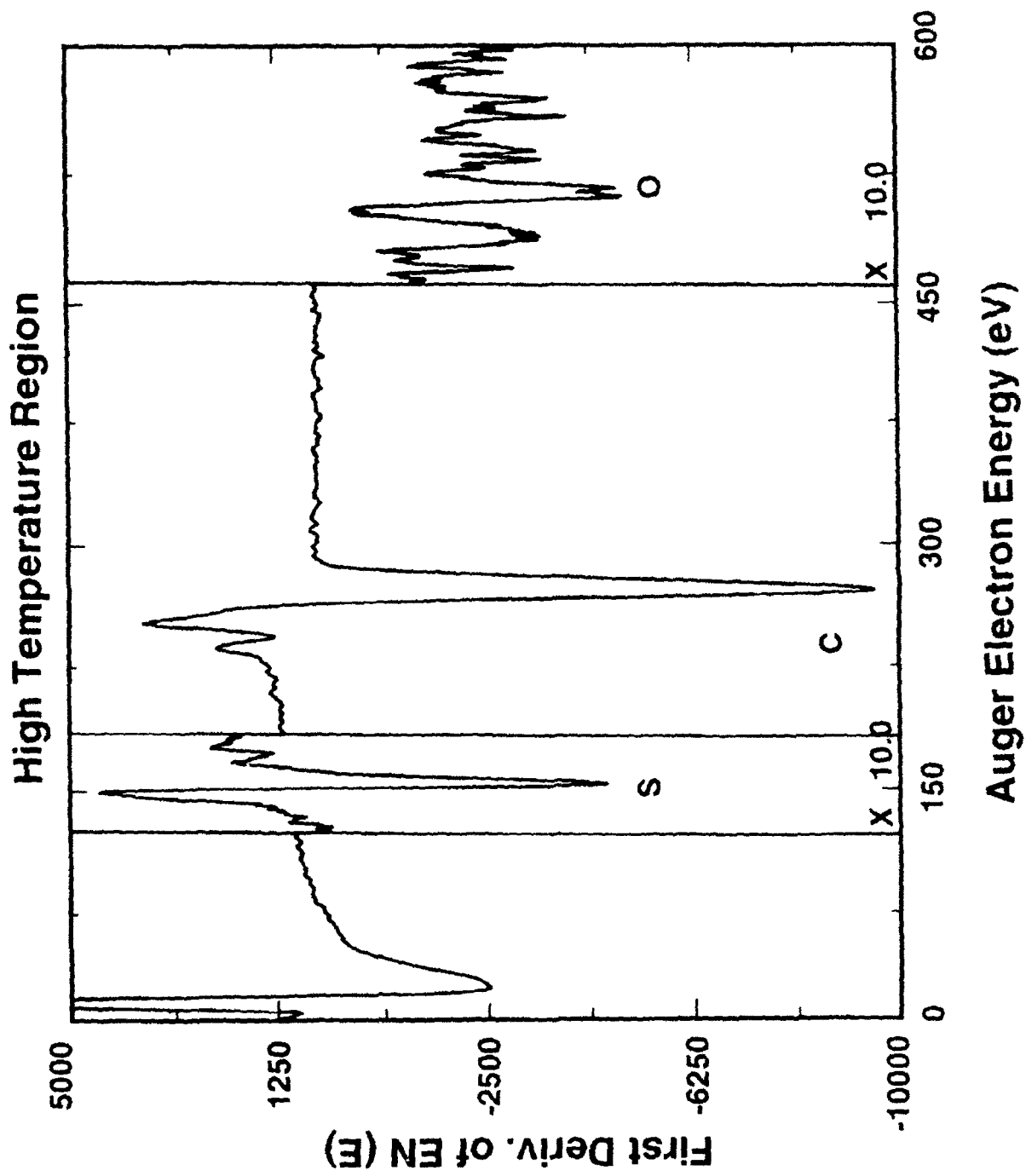


Figure 29 Auger spectrum from the high temperature (1,000-F) region of tube 9/91-6 (high sulfur fuel, 18-hour test) showing the presence of S and O in addition to C

9/91-6 High Temp. Region

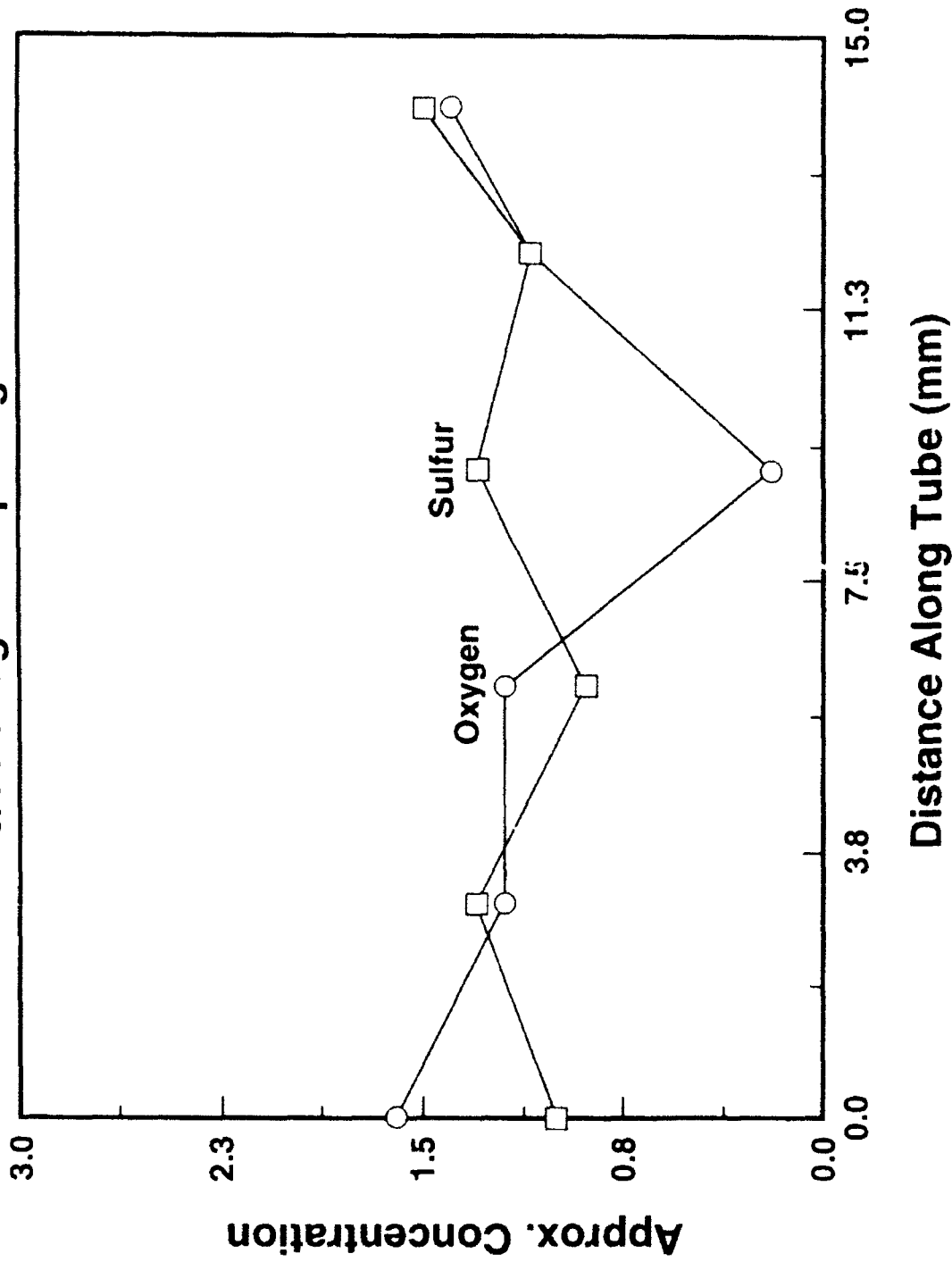


Figure 30. Plot of the S and O content as a function of position in the high temperature (1000°F) region of the 9/91-6 (high sulfur fuel, 18-hour test)

temperature region for tube 9/91-6. No definitive trend in the S and O content is observed as a function of position.

It is clear from the data presented above that distinct differences in the extent and type of the solids deposit exist between the low and high sulfur fuels. While it is tempting to assume that the S plays the major role in controlling the deposit, other factors such as O content cannot be ruled out and this should be an area for further investigation.

Our earlier observations of deposits from afterburner augmenters indicated that surface finish and surface composition play a role in the formation of deposits. For example, surface aspirates such as holes can change the flow and result in increased deposits. An example of such a deposit from an augmentor is shown in Figure 31. We have obtained SEM micrographs of the as-received stainless steel tube (Figures 32a, 32b) used in the fuel stressing experiments. These photomicrographs clearly indicate that surface aspirates exist in these tubes. The role that these features play in the formation of the deposits is the subject of our current studies.

We also performed Raman and fluorescence analyses of tubes 9/91-2 and 9/91-6 and began analysis of tube 9/91-9. The temperature profiles of the heated tubes, provided by Wright Laboratory, are shown in Figure 33. Spectra were obtained by focusing a blue (457.9nm) or green (514.5nm) laser beam onto a portion of the tube and analyzing the scattered light for its wavelength components. The resulting spectra include features from both Raman and fluorescent interactions. Both types of features are shown in Figure 34, in a spectrum obtained from tube 9/91-2 using blue excitation. The broad, dominant feature peaking at 550nm to 575nm is due to fluorescence from partially decomposed fuel molecules. Fluorescence results from the absorption of photons (e.g., from a laser source) by electrons in the material followed by re-emission. Less intense, narrow bands due to Raman interactions with charcoal-like residues of jet fuel occur on the rising slope of the fluorescence band between 475nm and 500nm. In the Raman effect photons interact with vibrational modes of materials, resulting in inelastically scattered (frequency shifted) wavelength components. In Figure 35, we show a spectrum, obtained using green excitation, from the same area of tube 9/91-2. Figure 35 is plotted in Raman spectral format, with the laser wavelength at 0cm^{-1} and the x axis in units of frequency shift from the laser wavelength. Background fluorescence was removed from this spectrum by a fitting procedure. The Raman bands near 1350cm^{-1} and 1600cm^{-1} are due to charcoal-like jet fuel residues composed of elemental carbon. Blue excitation maximizes the fluorescence intensity and provides the most complete fluorescence profile. Green excitation generally increases the Raman-to-fluorescence intensity ratio.

The fluorescence observed from these tube surfaces is believed to be due to partially-decomposed jet fuel residues. The fluorescence intensity should increase in regions where pyrolysis results in incomplete decomposition of the fuel and decrease where

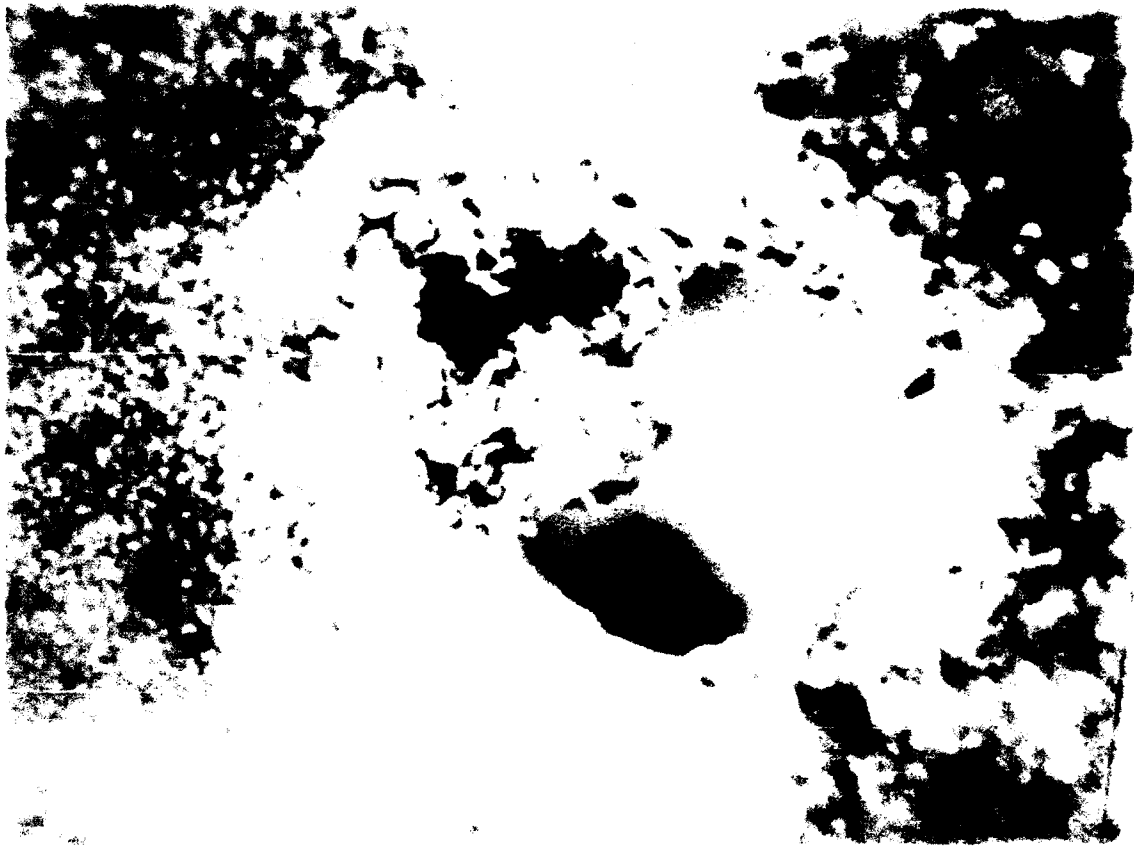


Figure 31. Photograph of the deposit around an asperity in an afterburner augments.



Figure 32. SEM photographs of aspirates on the surface of the stainless steel tubes used in the present tests. The aspirates are Cr and Si rich.



Jet A 2827 and Jet A-1 2747 Temperature Profiles

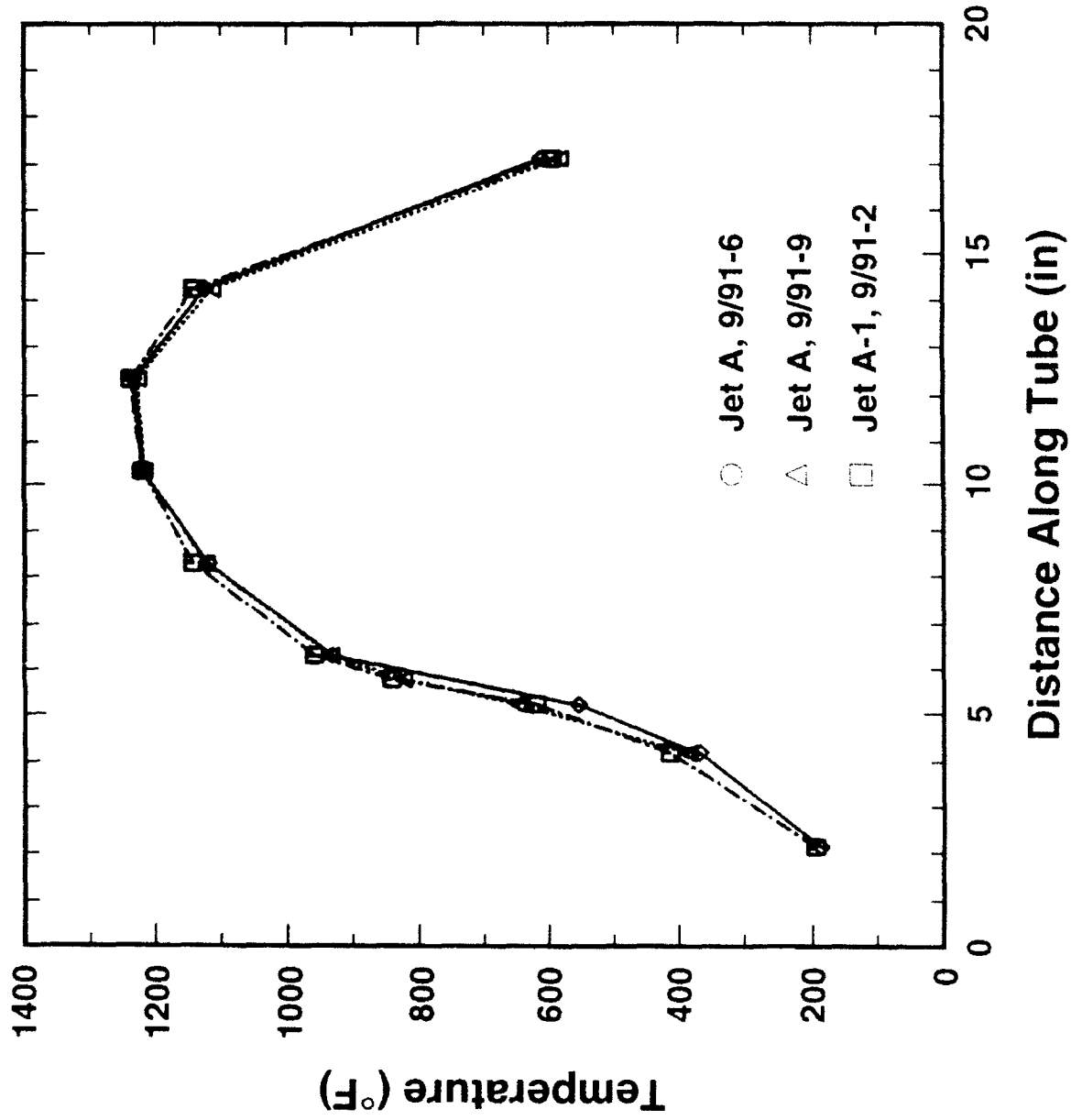


Figure 33 Steady-state temperature profiles for tubes 9/91-2, 9/91-6, and 9/91-9 as provided by WPAFB

Tube 9/91-2, Side A, 4" along tube, Fluorescence Spectrum

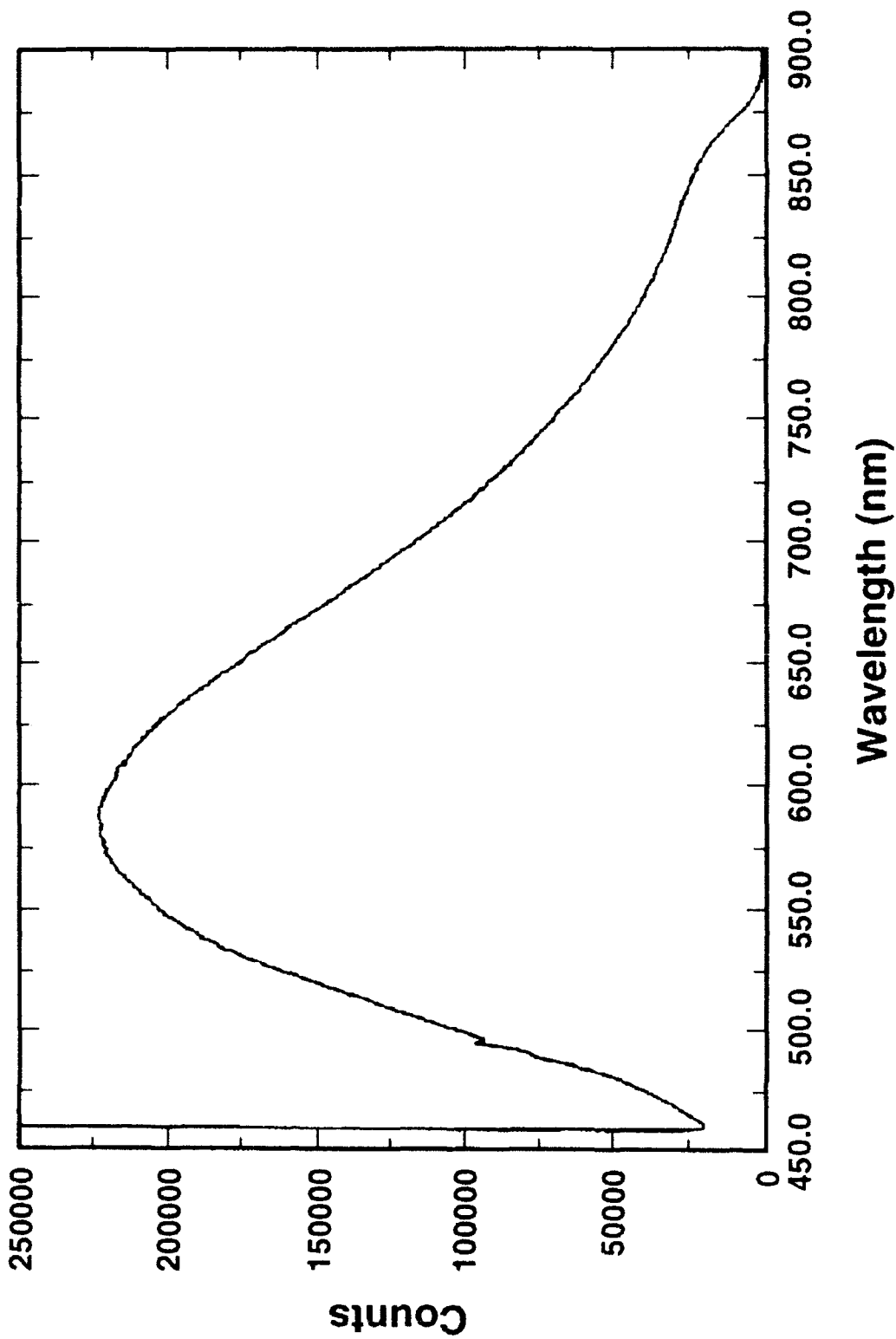


Figure 34. Blue-excited (457.9 nm) fluorescence spectrum, including Raman bands, at 4" along Side A of tube 9/91-2

Tube 9/91-2, Side A, 4" along tube, Raman Spectra

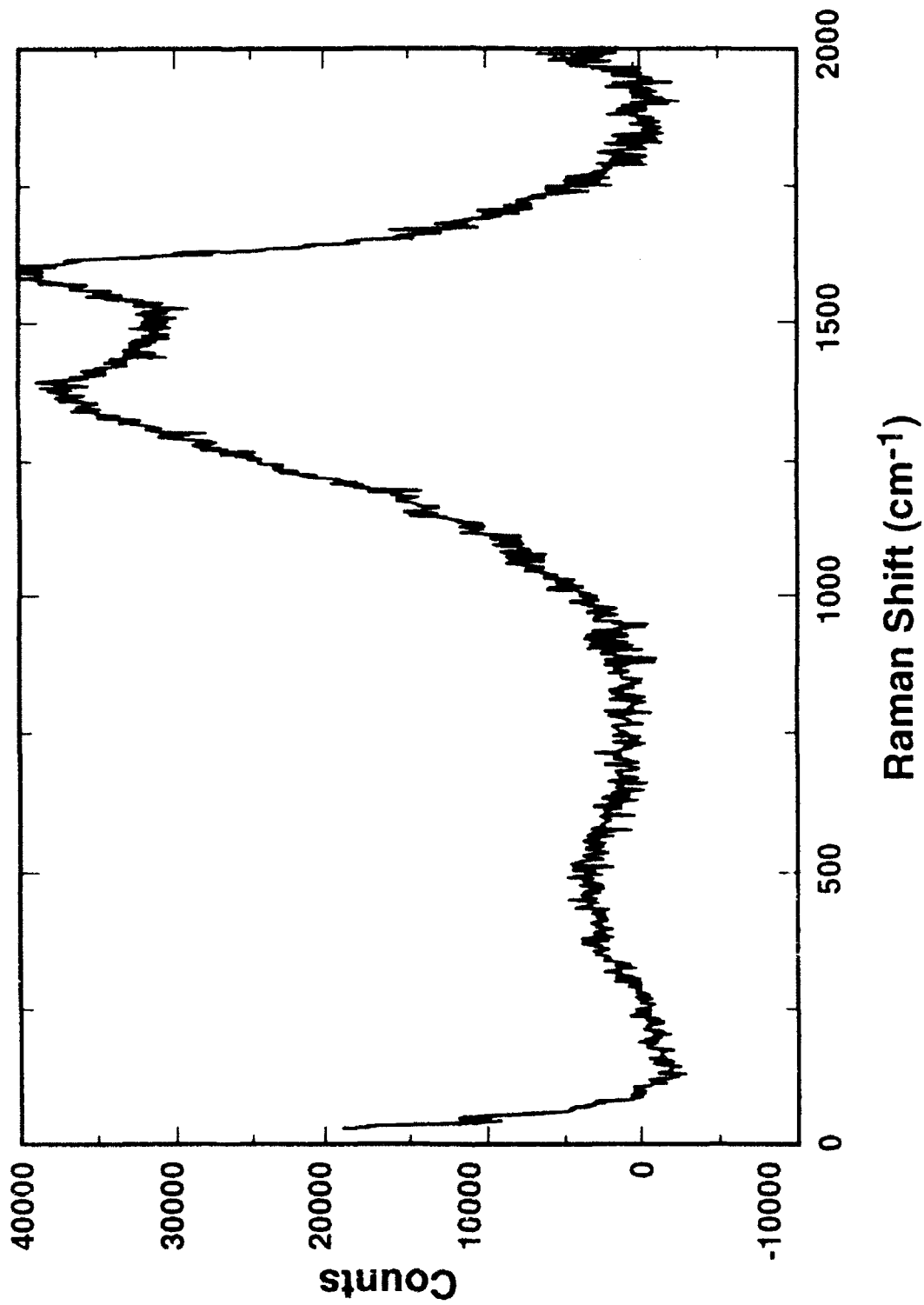


Figure 35. Green-excited (514.5 nm) Raman-format spectrum, with background fluorescence removed, at 4" along Side A of tube 9/91-2

temperatures are high enough to more completely convert the fuel to elemental carbon. Elemental carbon is not fluorescent, but its Raman bands narrow and change in relative intensity as a function of temperature. Thus, high fluorescence intensities indicate regions of relatively low temperature where pyrolysis results in incomplete decomposition, and carbon Raman bands provide a temperature scale (when compared to carbon deposits of known temperature history) for regions where temperatures were high enough to complete the decomposition of the jet fuel.

Qualitatively the variations in fluorescence intensity are similar for tubes 9/91-2 and 9/91-6 and for tube 9/91-9 as far as it has been analyzed. Blue-excited fluorescence spectra for tube 9/91-2 are shown in Figures 36 and 37 and for tube 9/91-6 in Figures 38 and 39. Green-excited spectra for the 2-to-6 inch positions of tube 9/91-9 are shown in Figure 40. Spectra are shown for Side A. Green-excited spectra from both sides of tubes 9/91-2 and 9/91-6 show the same trends. The fluorescence intensities at the 2-inch position are relatively low. Fluorescence intensities increase and peak at the 4- or 5-inch position before dropping to relatively low values by the 6-inch position. This maximum in fluorescence intensity corresponds to a peak in the plot of mass deposited versus distance along tube 3/91-3 (Figure 41). Comparing the temperature, fluorescence, and mass-deposited profiles (Figures 33, 36, 38, 40 and 41), we conclude that pyrolysis becomes significant at 4 to 5 inches along the tube, where the temperature reaches approximately 400°F (204°C). Pyrolysis at this temperature is not sufficient to carbonize all the jet fuel molecules undergoing decomposition, resulting in the deposition of partially-decomposed, fluorescent materials. Further along the tube, at about 6 inches or 600°F (316°C), pyrolysis results in much more complete carbonization of the jet fuel residues that are deposited on the wall of the tube, and the intensity of the fluorescence decreases.

Since the steady-state temperature remains above 600°F for the rest of the length of the tubes (see Figure 33), the expectation is that the fluorescence intensity should be low over the remaining length of the tubes. However, as shown in Figures 37 and 39, a maximum in the fluorescence intensity occurs at approximately 8 inches along the tubes, and the fluorescence intensity is increasing at 17 inches, near the end of the tubes. These regions of enhanced fluorescence suggest that low-temperature pyrolysis occurred in regions other than 4 to 5 inches along the tube and at other than steady-state conditions. Most likely, the regions of enhanced fluorescence at 8 and 17 inches along the tubes represent deposition that occurred during cool-down after a heating cycle while fuel was still flowing down the tubes.

The fluorescence traces from locations at 8 inches or more along the tube have a fluorescence band peaking at 700nm to 750nm in addition to one peaking at 550nm to 575nm. The presence of two fluorescence bands suggests the presence of more than one species of fuel residue. There is the possibility that this additional fluorescence band represents very late stage deposition of a slightly decomposed fuel residue, but thus far no definite conclusion can be made.

Tube 9/91-2, I, Side A (0"-6" along tube, 457.9 nm)

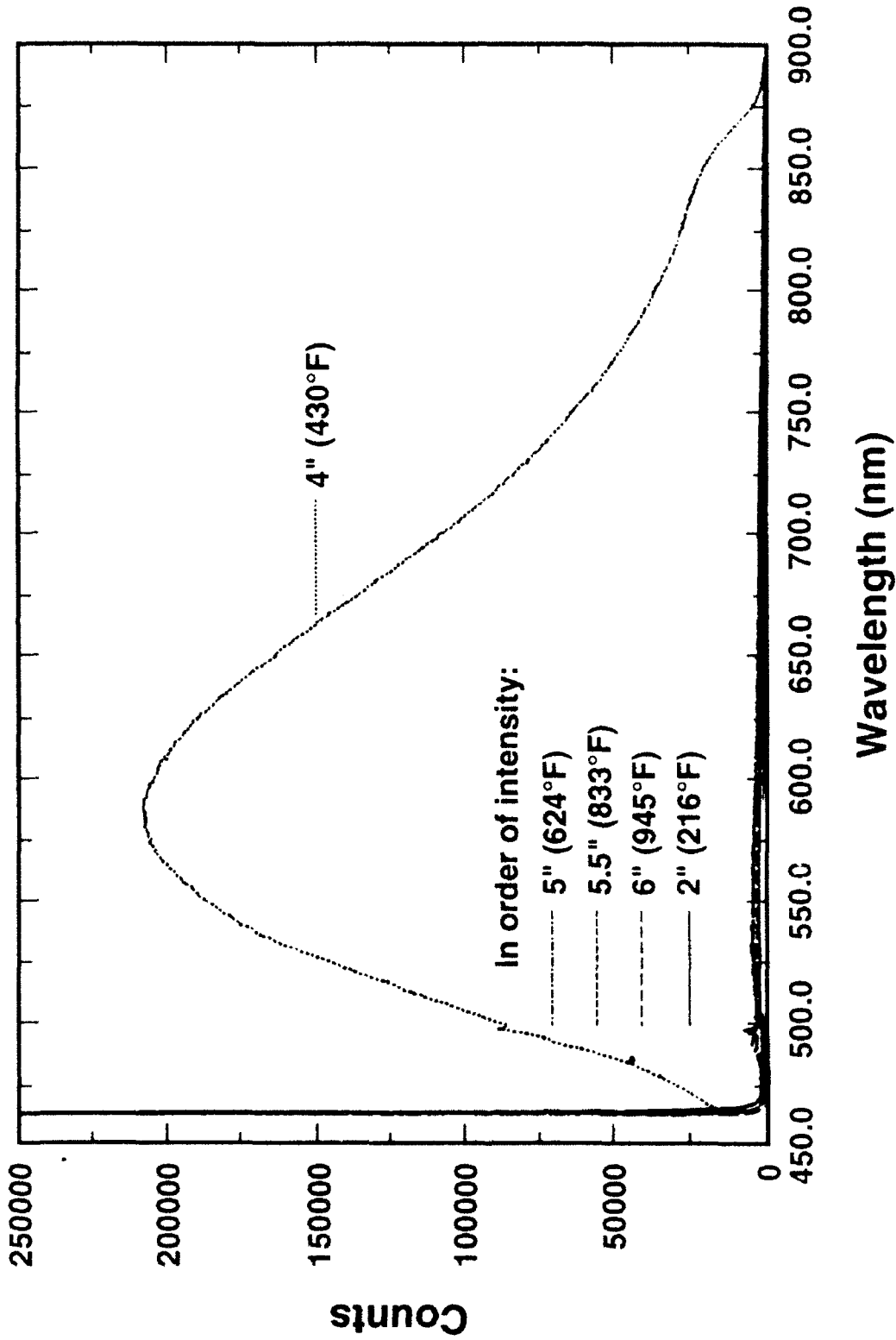


Figure 36 Blue-excited (457.9 nm) fluorescence spectra, including Raman bands, at 0" to 6" along Side A of tube 9/91-2

Tube 9/91-2, II & III, Side A (6"-18" along tube, 457.9 nm)

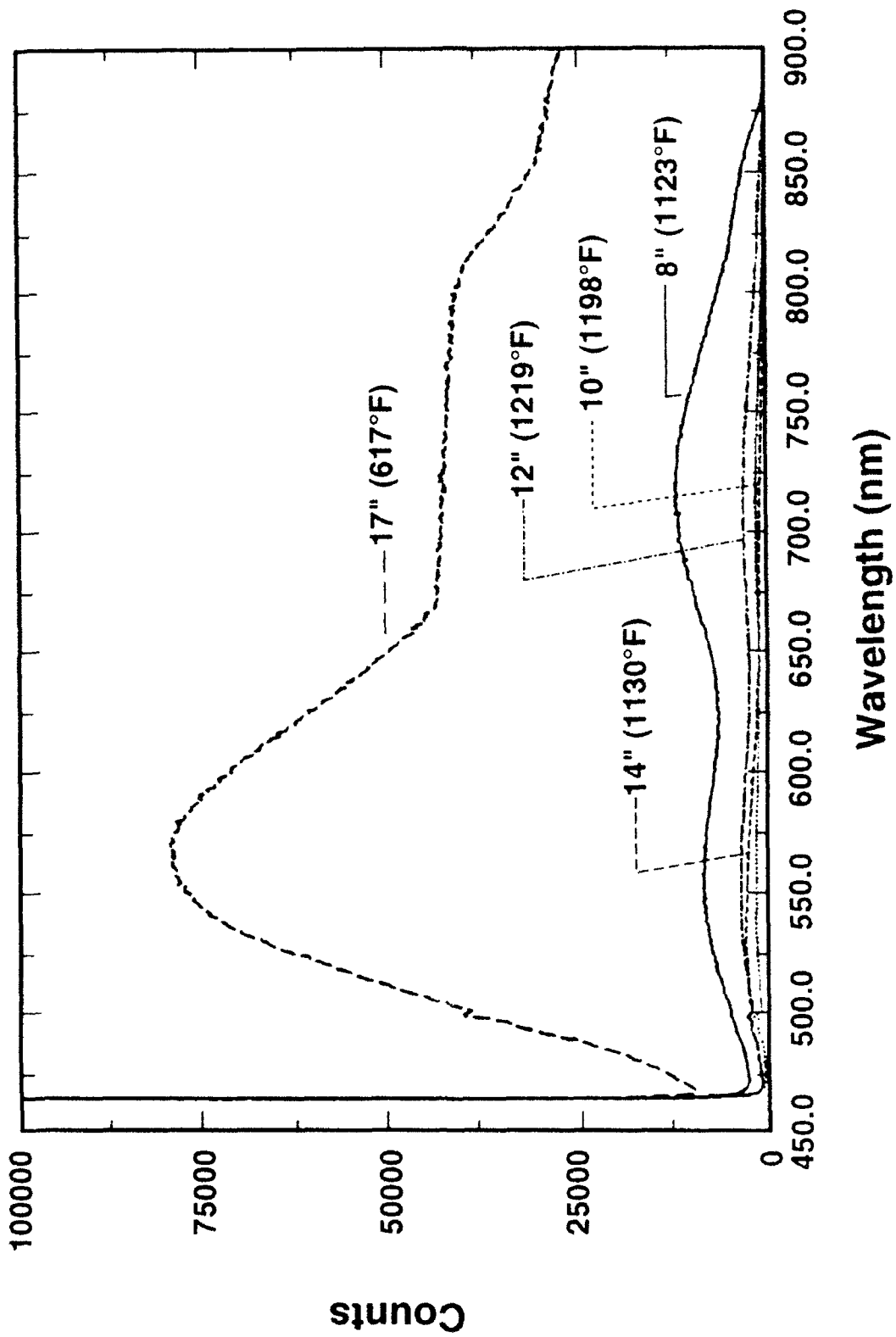


Figure 37 Blue-excited (457.9 nm) fluorescence spectra including Raman bands at 6" to 18" along Side A of tube 9/91-2

Tube 9/91-2, I, Side A (0"-6" along tube, 457.9 nm)

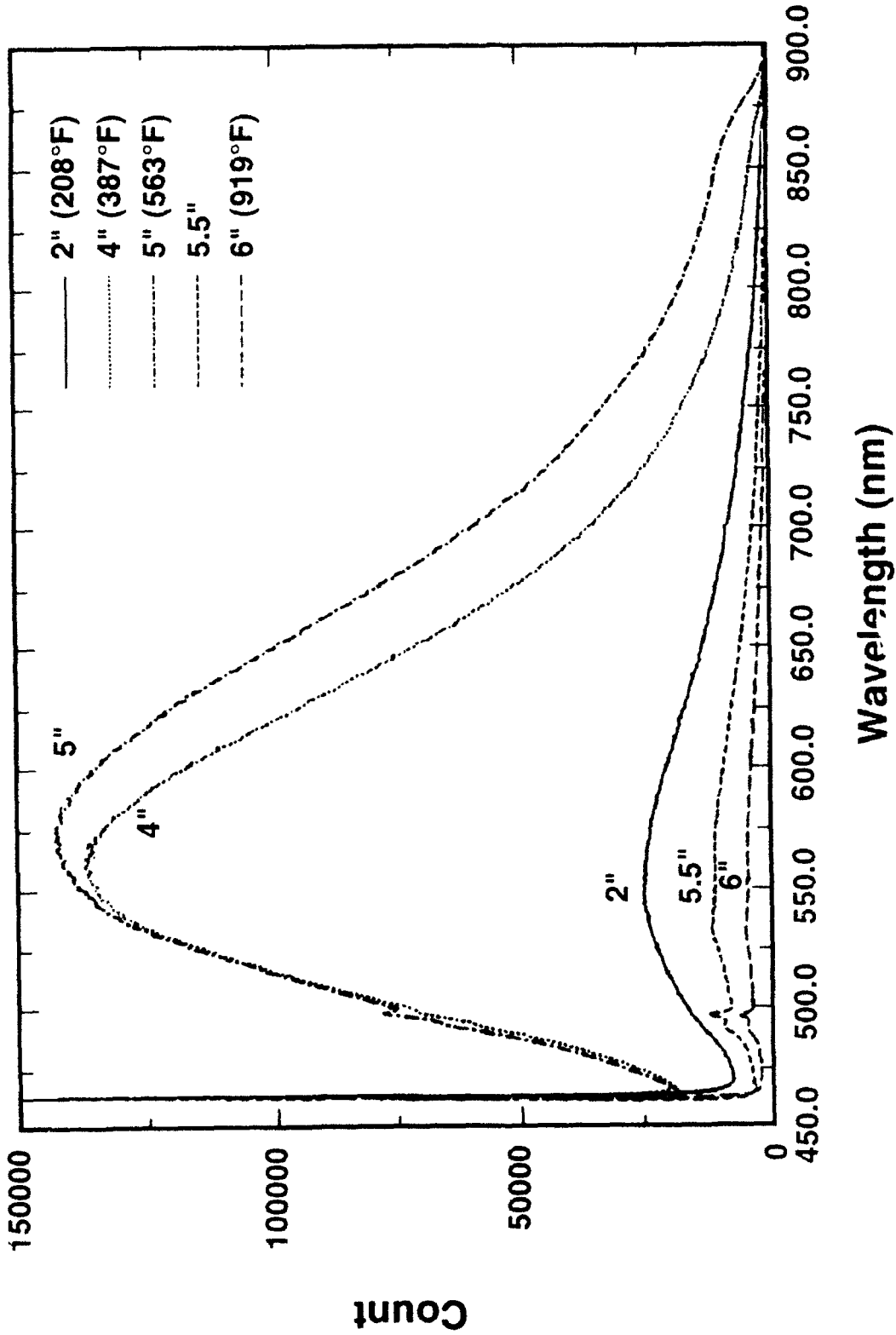


Figure 38. Blue-excited (457.9 nm) fluorescence spectra, including Raman bands, at 0" to 6" along Side A of tube 9:91-6.

Tube 9/91-6, Side A, II (6"-12") and III (12"-18"), 457.9nm

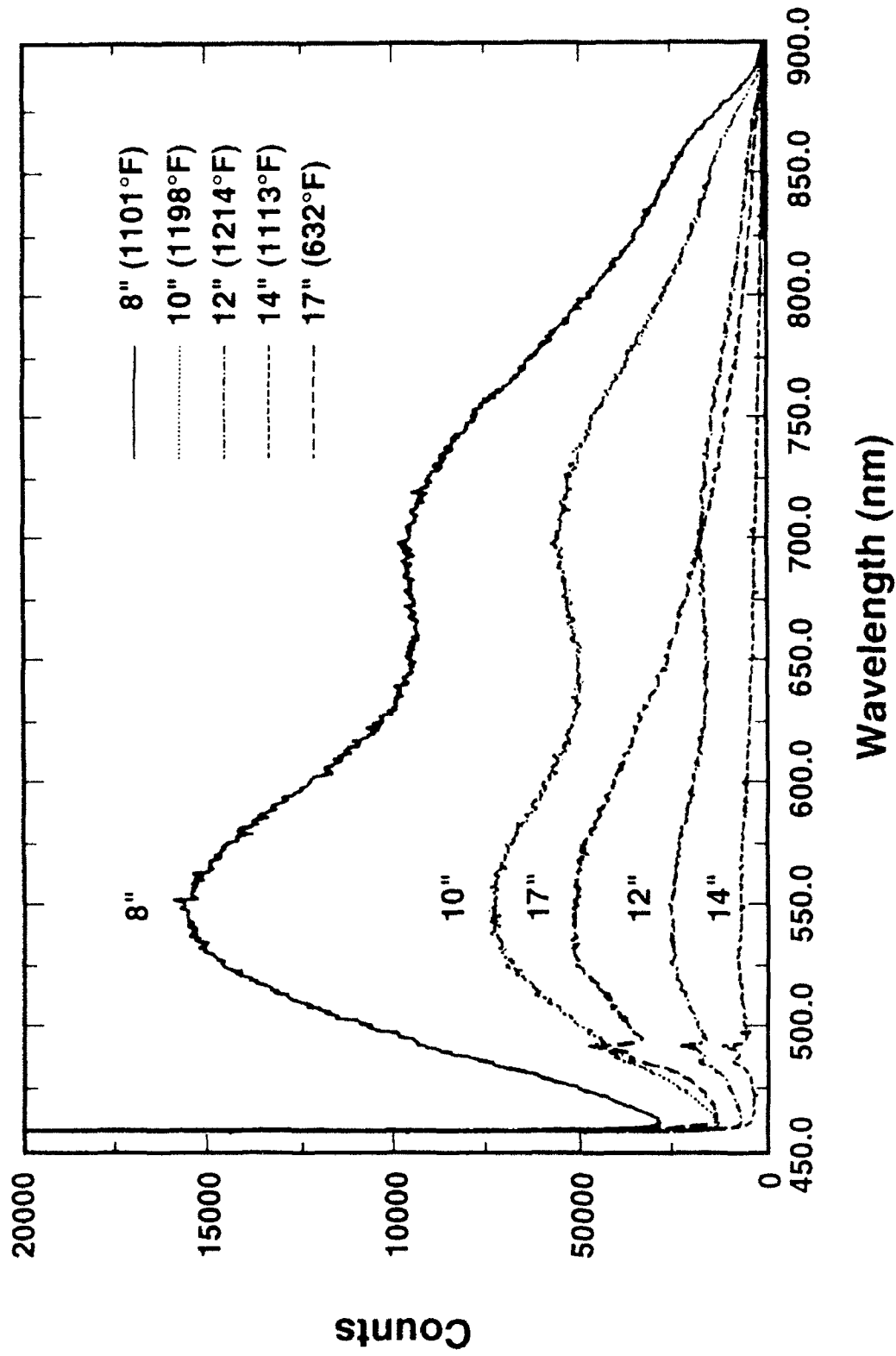


Figure 39. Blue-excited (457.9 nm) fluorescence spectra, including Raman bands, at 6" to 18" along Side A of tube 9/91-6

Tube 9/91-9, Side A (0"-6") along tube, 514.5nm)

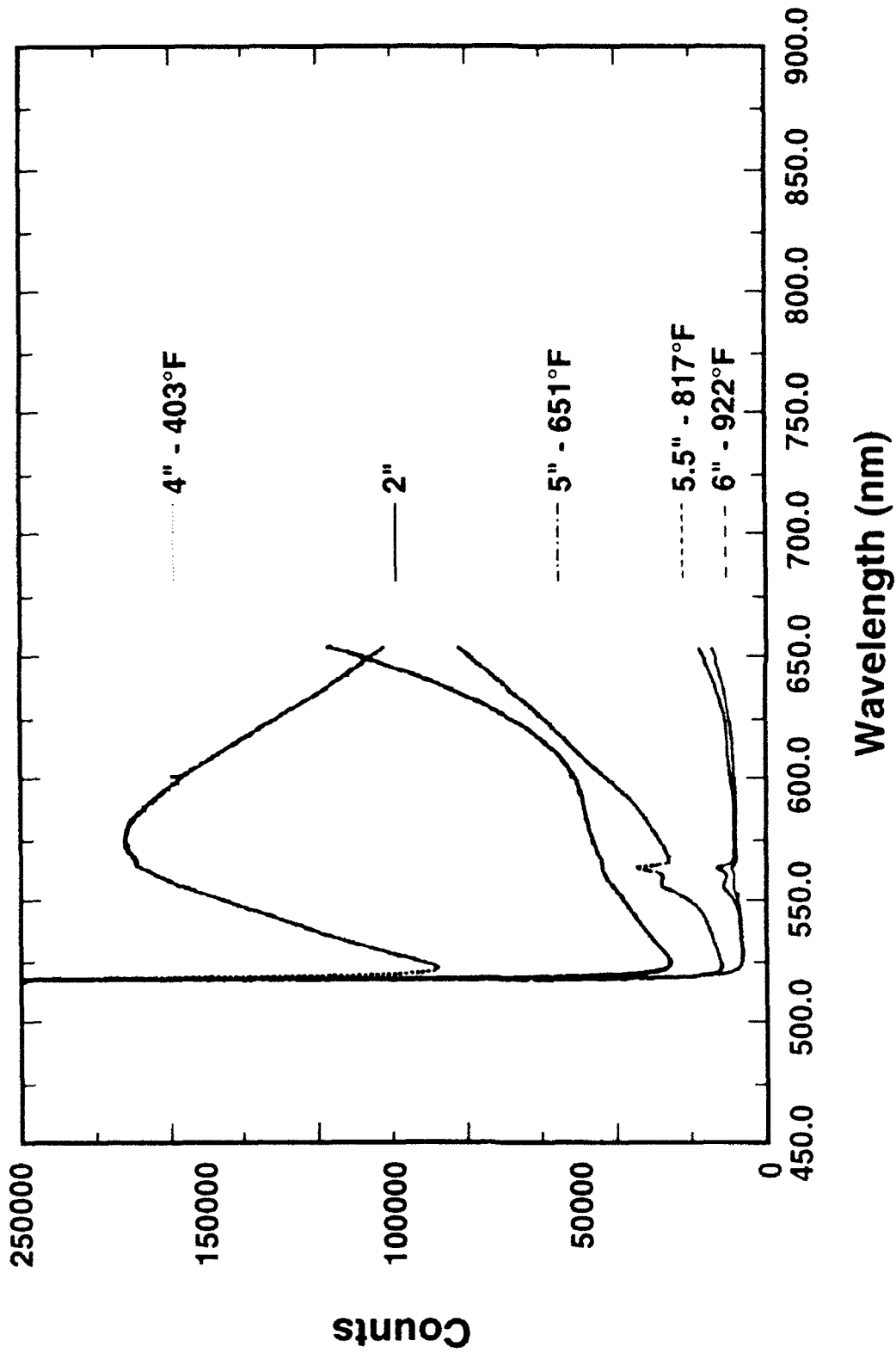


Figure 40 Green-excited (514.5 nm) fluorescence spectra, including Raman bands, at 0" to 6" along Side A of tube 9:91-9

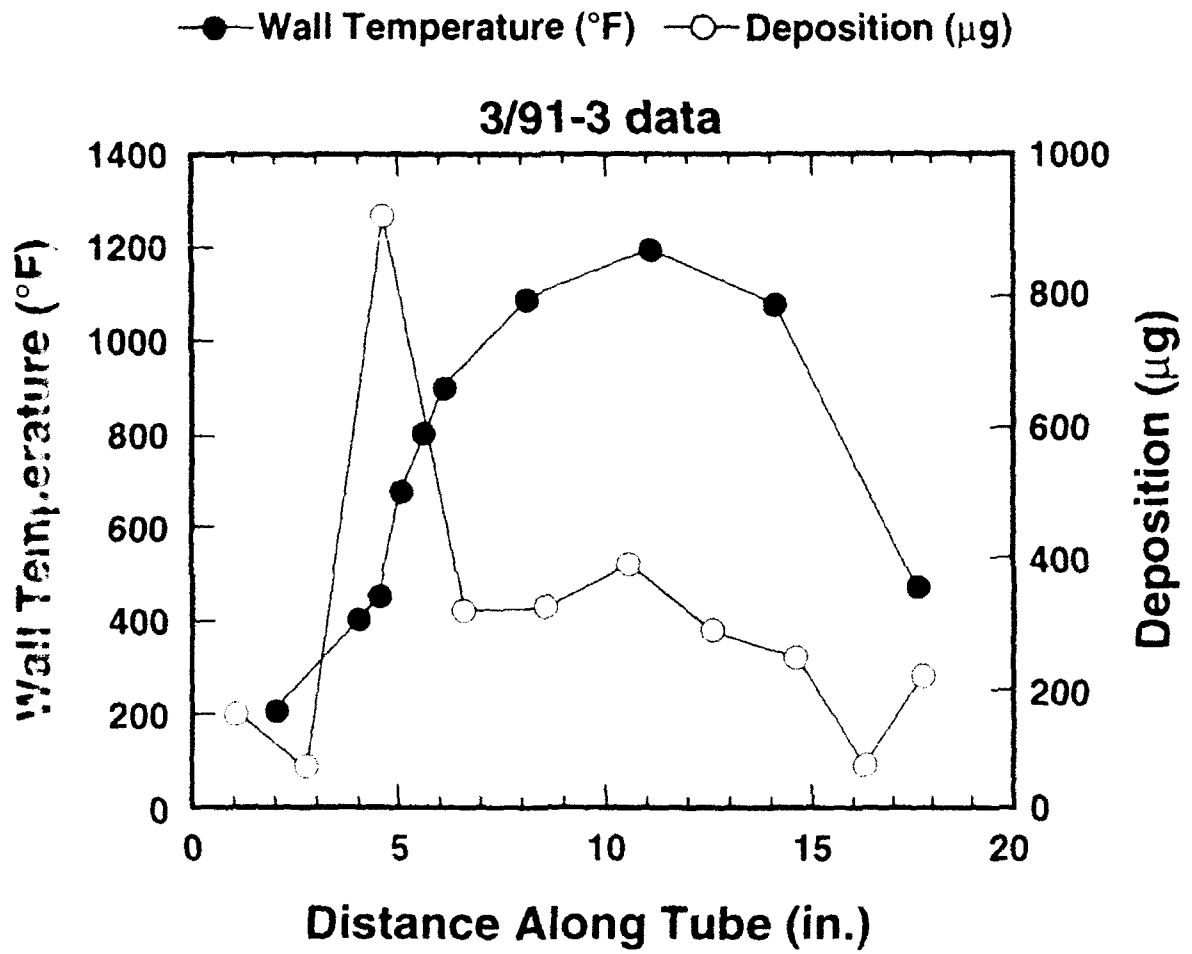


Figure 41. Steady-state wall temperatures (°F) and deposition masses (μg) as a function of distance along tube 9/91-3, as provided by WPAFB.

Raman bands from carbon residues suggest a deposition scenario similar to that derived from the fluorescence data. Green-excited spectra of the carbon Raman band region are shown for tube 9/91-2 in Figures 42 and 43 and for tube 9/91-6 in Figures 44 and 45. Green-excited Raman spectra of the two-to-six-inch region of tube 9/91-9 are shown in Figure 46. The intensities of the carbon Raman bands have been scaled to facilitate their comparison. High noise levels in certain spectra are the result of scaling up low-intensity data or because the Raman bands were originally imposed on a high level of fluorescence (see Figures 36-40).

As with the fluorescence data, the trends in the Raman spectra obtained at 0 to 6 inches along the tubes (Figures 42, 44 and 46) are qualitatively the same for 9/91-2 (both sides), 9/91-6 (both sides) and 9/91-9 (only Side A analyzed to date). At 2 inches along the tubes, the carbon Raman bands (1100cm^{-1} to 1700cm^{-1}) are of low intensity and diffuse. By 4 inches along the tube, the carbon Raman bands have increased in intensity and have begun to display the two band pattern (-1350cm^{-1} and -1600cm^{-1}) characteristic of elemental (glassy or graphitic) carbon. From 4 to 6 inches along the tubes, the carbon Raman bands narrow and become more distinct, consistent with increasing steady-state temperatures.

At 8 inches along the tubes, the steady-state temperatures (-1100°F or 593°C) would dictate still narrower, more distinct carbon Raman bands. However, the carbon Raman bands observed at 8 inches along the tubes (Figures 43 and 45) are relatively broad and resemble those produced by residues deposited at 4 inches along the tubes, where the steady-state temperatures were -400°F . At 10 and 12 inches along the tubes, the carbon Raman bands are considerably narrower than at 8 inches and are more consistent with steady-state temperatures in the 1100°F to 1200°F range. At 14 inches along tube 9/91-2 and at 17 inches along both tubes 9/91-2 and 9/91-6, the carbon Raman bands are broad again and more consistent with material deposited near 400°F than at the steady-state temperatures measured for these locations.

The Raman spectra suggest the same deposition scenario derived from the fluorescence data. Steady-state low-temperature pyrolysis becomes significant, depositing low-temperature carbon, at about 4 inches along the tubes. Transient low-temperature pyrolysis events, presumably occurring during the cool-down after a heating cycle while fuel is still flowing through the tubes, occur at approximately 8 and 17 inches along the tubes. Maxima in the plot of deposition mass versus distance along tube 9/91-3 (Figure 41) also occur near 4, 8 and 17 inches. Because the carbon deposits are highly opaque to visible light, the blue and green excitation wavelengths sample only top layer of deposits, corresponding to the last deposition event. The Raman data from these tubes cannot be used as calibration points to associate carbon Raman band characteristics with temperature because the last deposition event may have occurred at other than the measured steady-state temperature.

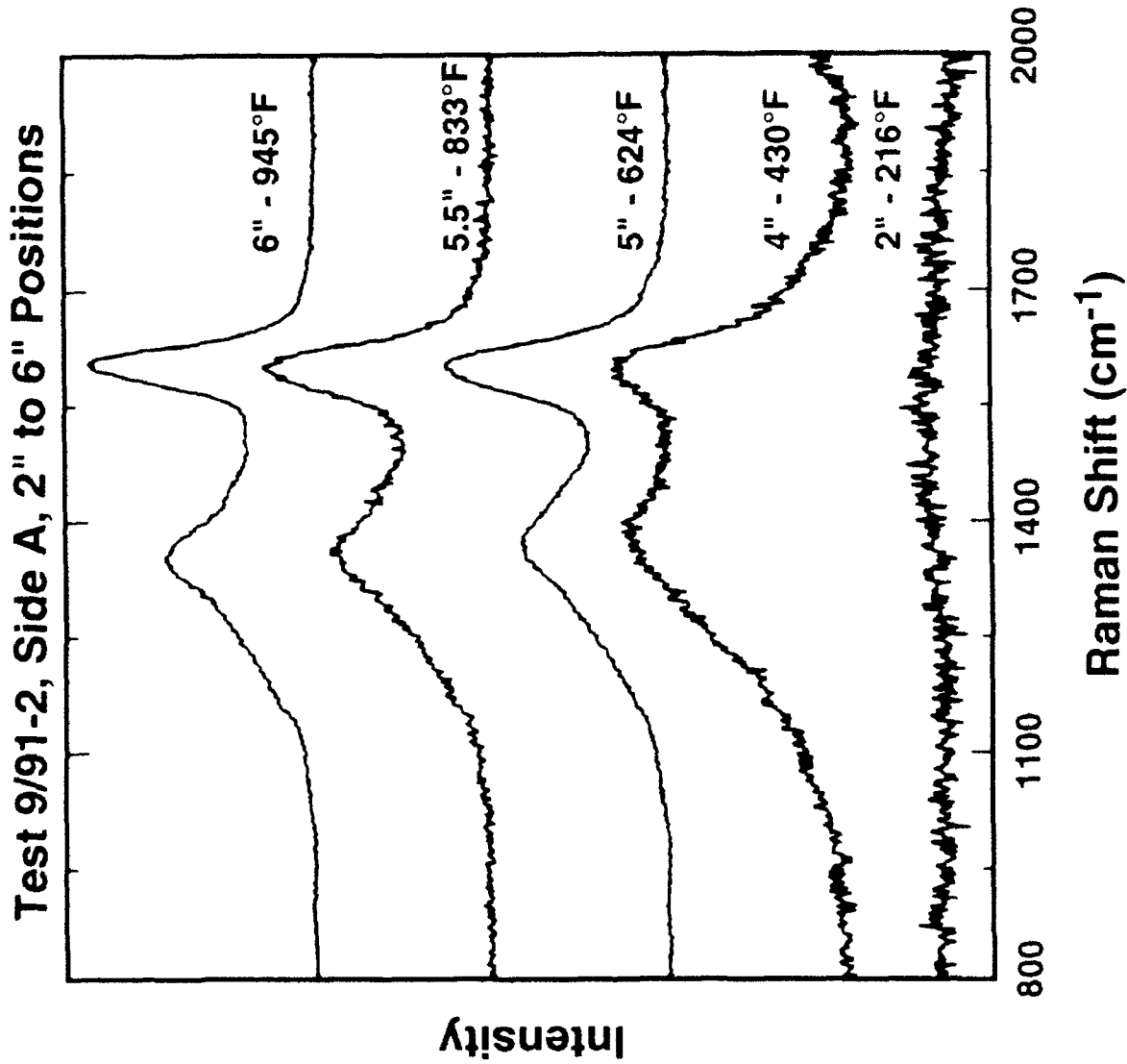


Figure 42 Green-excited (514.5 nm) Raman-formal spectra with background fluorescence removed, at 0" to 6" along Side A of tube 9/91-2

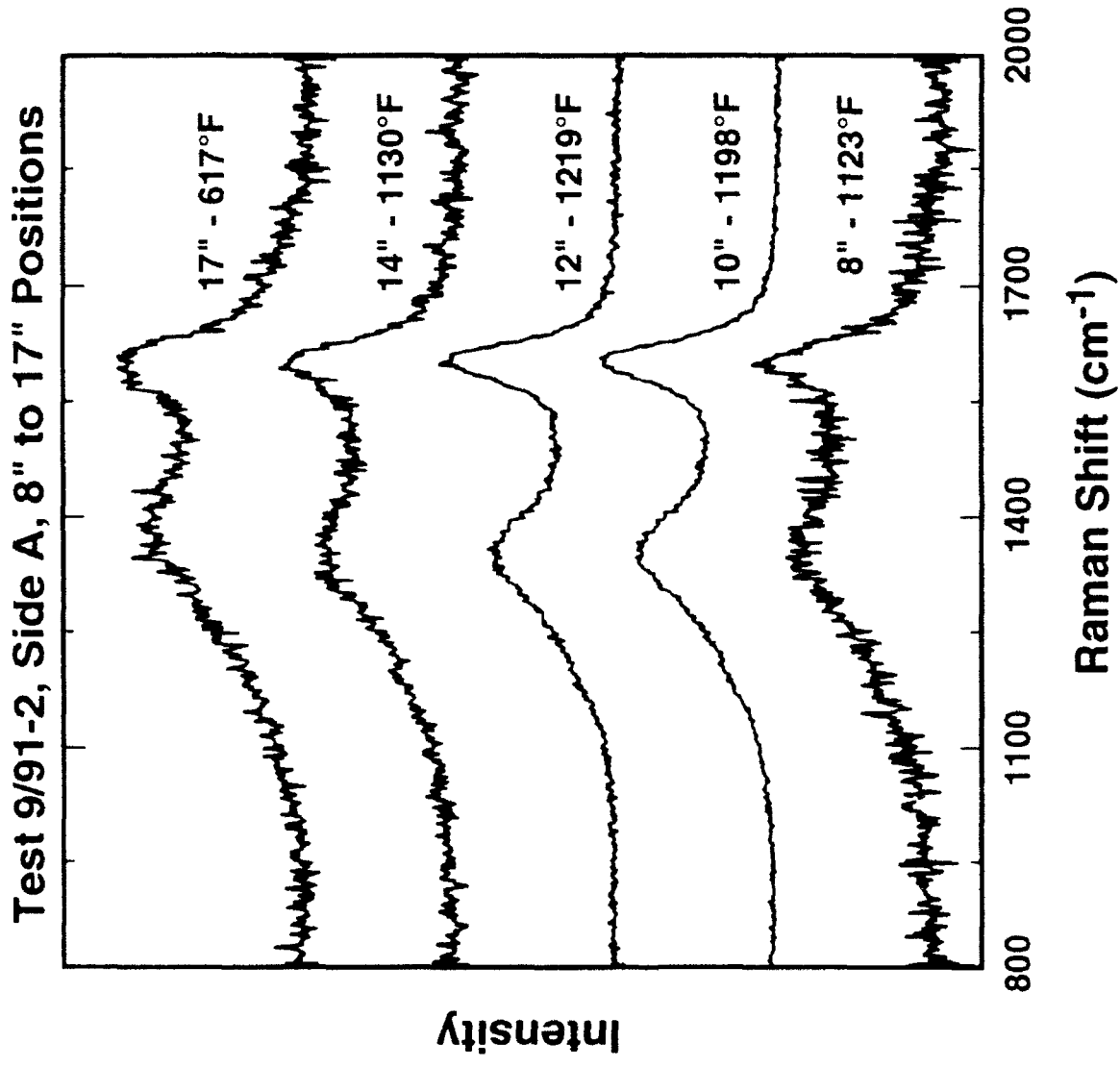


Figure 43. Green-excited (514.5 nm) Raman-format spectra, with background fluorescence removed, at 6" to 18" along Side A of tube 9/91-2.

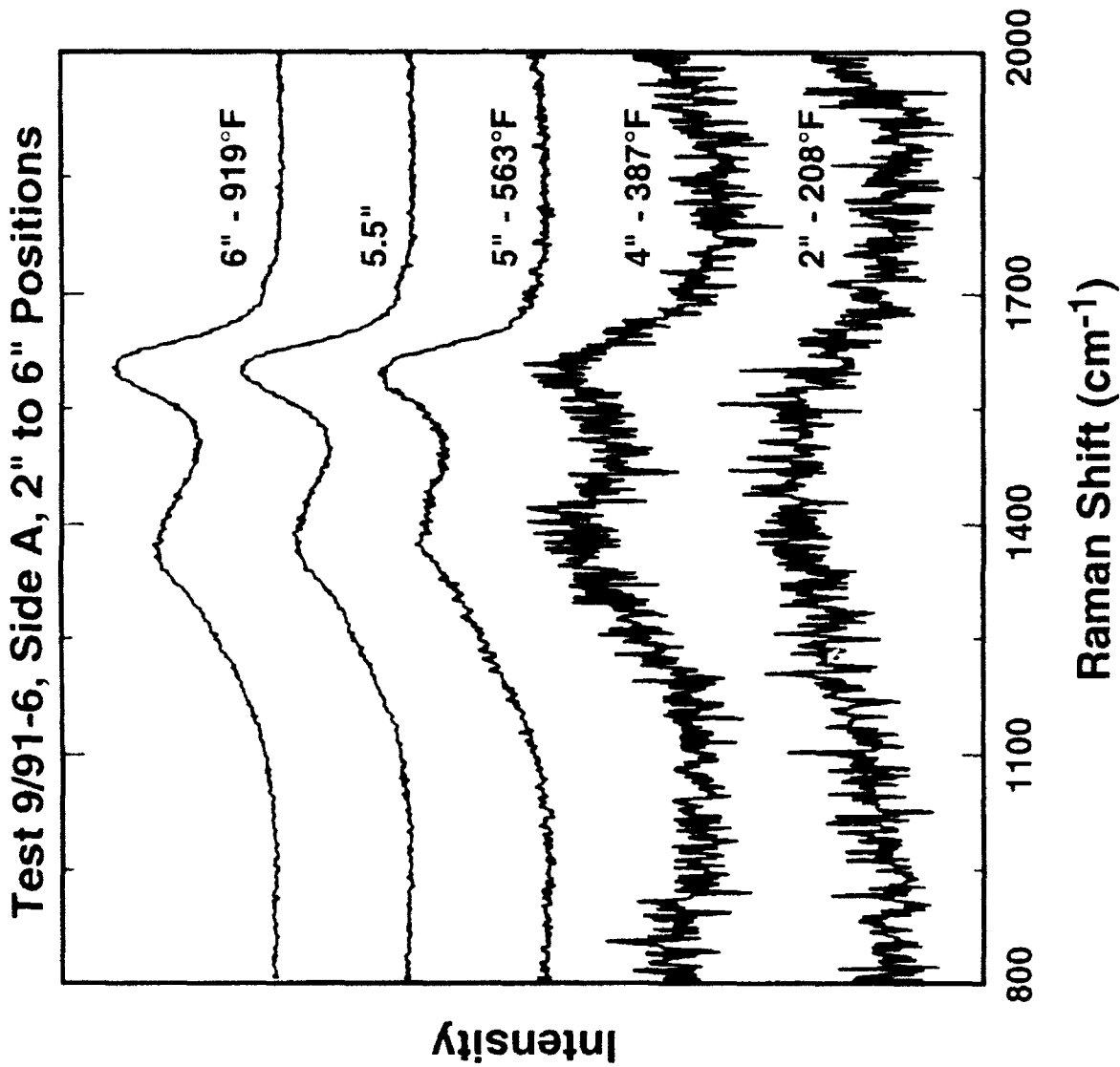


Figure 44. Green-excited (514.5 nm) Raman-format spectra, with background fluorescence removed, at 0" to 6" along Side A of tube 9/91-6.

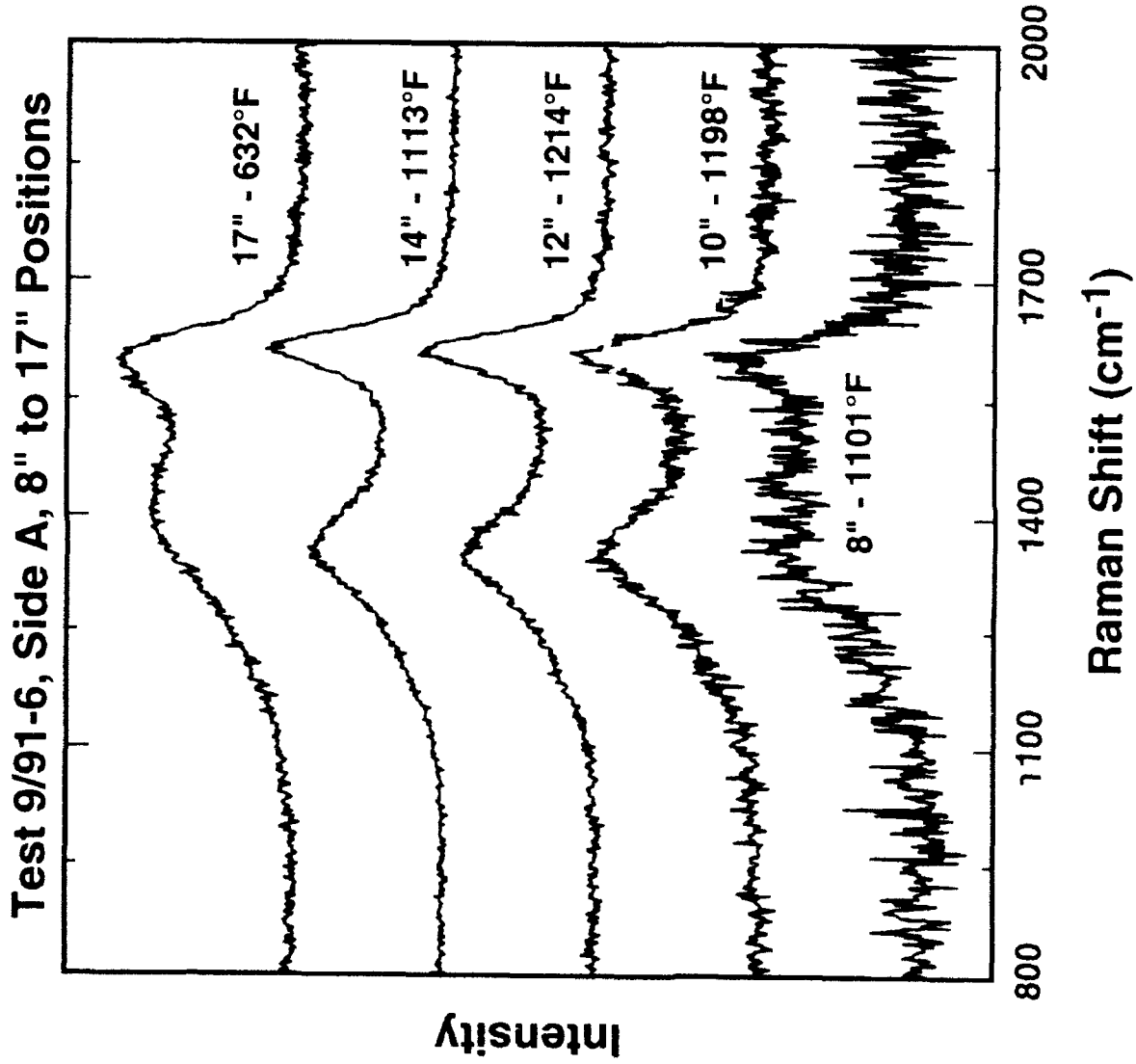


Figure 45 Green-excited (514.5 nm) Raman-format spectra, with background fluorescence removed, at 6" to 18" along Side A of tube 9/91-6

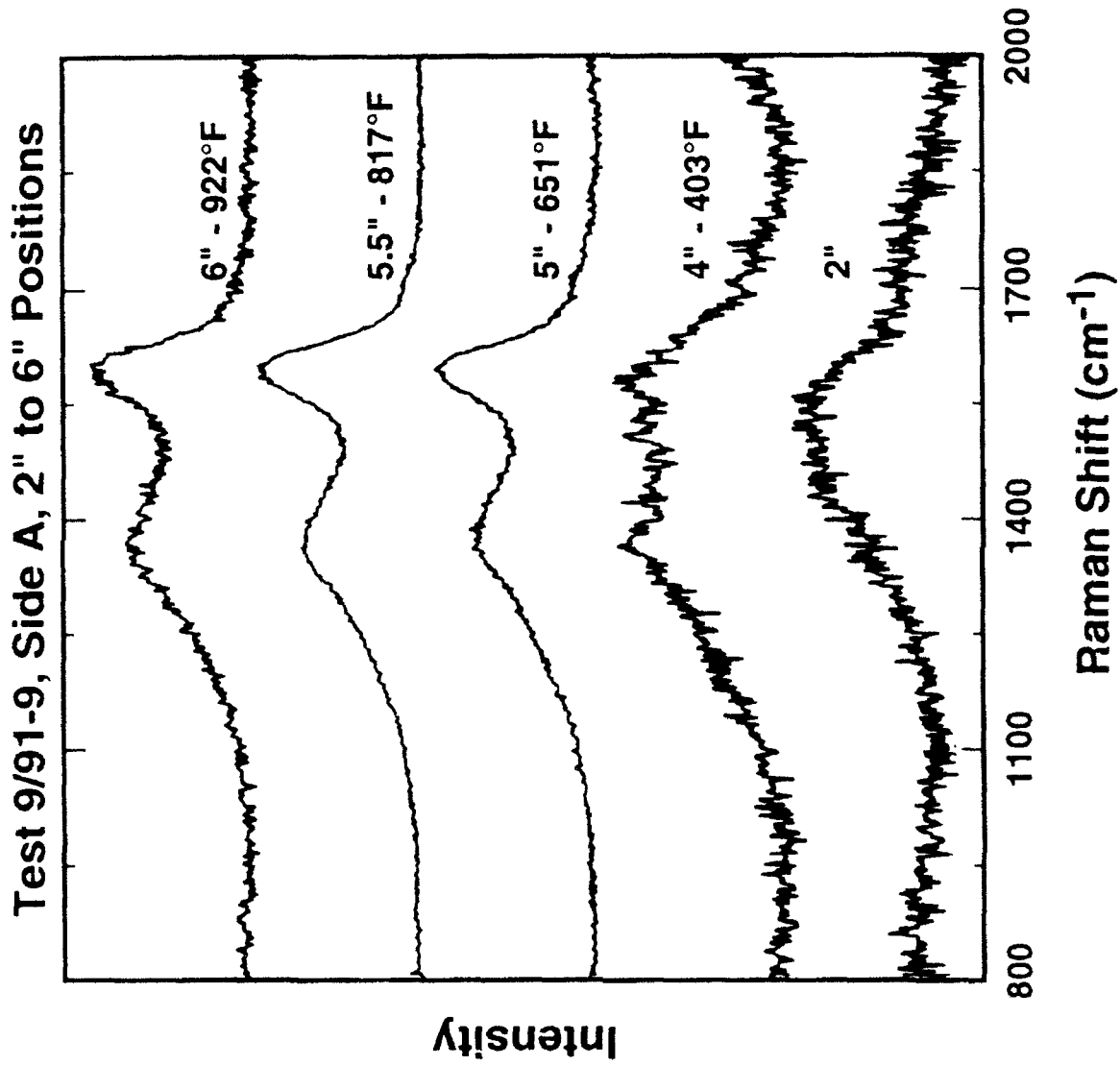


Figure 46. Green-excited (514.5 nm) Raman-format spectra, with background fluorescence removed, at 0" to 6" along Side A of tube 9/91-9.

A Raman band near 669cm^{-1} occurs in spectra obtained at locations near 2 and 8 inches along the tubes (see Figure 47). This Raman band is believed to be due to spinel-like materials formed by oxidation of the metal surface of the tube. In order for visible light to sample the metal surface, the opaque carbon deposits at these locations must be very thin or intermittent. This is not surprising for the 2-inch location, since the steady-state temperature is too low for pyrolysis to result in heavy carbon deposits. Low levels of carbon deposition at the 8-inch location are probably due to a "shadowing" effect. Surface concentrations of fuel vapor are strongly depleted by the pyrolysis occurring at 4 to 6 inches along the tubes, so that even though the temperature is relatively high at 8 inches along the tubes, there is little fuel available to pyrolyze and deposit. Deposits at the 8-inch location may come primarily from transient effects during cool-down. Further along the tubes the surface concentration of fuel vapor is replenished by diffusion or turbulence, and the amount of deposition increases.

While the trends from the low-sulfur (Jet A-1) and high-sulfur fuels are qualitatively similar, some differences can be noted. The pyrolysis zones from the tubes fed with high-sulfur fuel tend to be wider (compare, e.g., Figures 36 and 38). Also, there appears to be more evidence for Raman-active sulfur-containing species in the spectra from the tubes fed with high-sulfur fuel. Figure 48 shows the Raman spectrum from the 2-inch location of Side A of tube 9/91-6. In addition to a diffuse carbon Raman band(s), the spectrum includes a Raman band at 288cm^{-1} , which occurs only in this spectrum, and a Raman band at 436cm^{-1} , which occurs in spectra from locations on tube 9/91-6 at which low-temperature pyrolysis occurred. The 288cm^{-1} band is near the most intense Raman band (252cm^{-1}) of dithionite, $\text{S}_2\text{O}_4^{2-}$. The 436cm^{-1} band may be due to thiosulfate-like species ($\text{S}_2\text{O}_3^{2-}$) or species with carbon-sulfur bonds.

In Figure 49, we compare Raman spectra from the 12-inch location, Side A, of tubes 9/91-2 and 9/91-6. This is the best location to compare spectra from different tubes, because the steady-state temperatures are nearly identical, because Sides A and B give consistent spectra for both tubes at this location, and because there is no evidence in the results from either tube for a low-temperature pyrolysis zone at this location. The Raman spectra in Figure 49 are nearly indistinguishable, providing evidence that the carbon Raman band shapes are reproducible functions of steady-state temperature and that the sulfur content of the fuel does not necessarily have a large effect on the carbon Raman band shape.

Deposition of jet fuel residues in tubes 9/91-2 and 9/91-6 (and in tube 9/91-9 as far as it has been analyzed) occurs qualitatively in the same manner. Low-temperature pyrolysis, resulting in heavy accumulations of carbon and partially decomposed jet fuel, occurs at approximately 4 inches along the tubes during steady-state operation. The measured temperature at 4 inches along the tubes during steady-state operation is approximately 400°F . Raman and fluorescence data suggest that additional low-temperature pyrolysis occurs near 8 and 17 inches along the tubes. Because the steady-state temperatures at 8 and 17 inches along the tubes were well above 400°F ,

Test 9/91-6, Side A, 8" Position

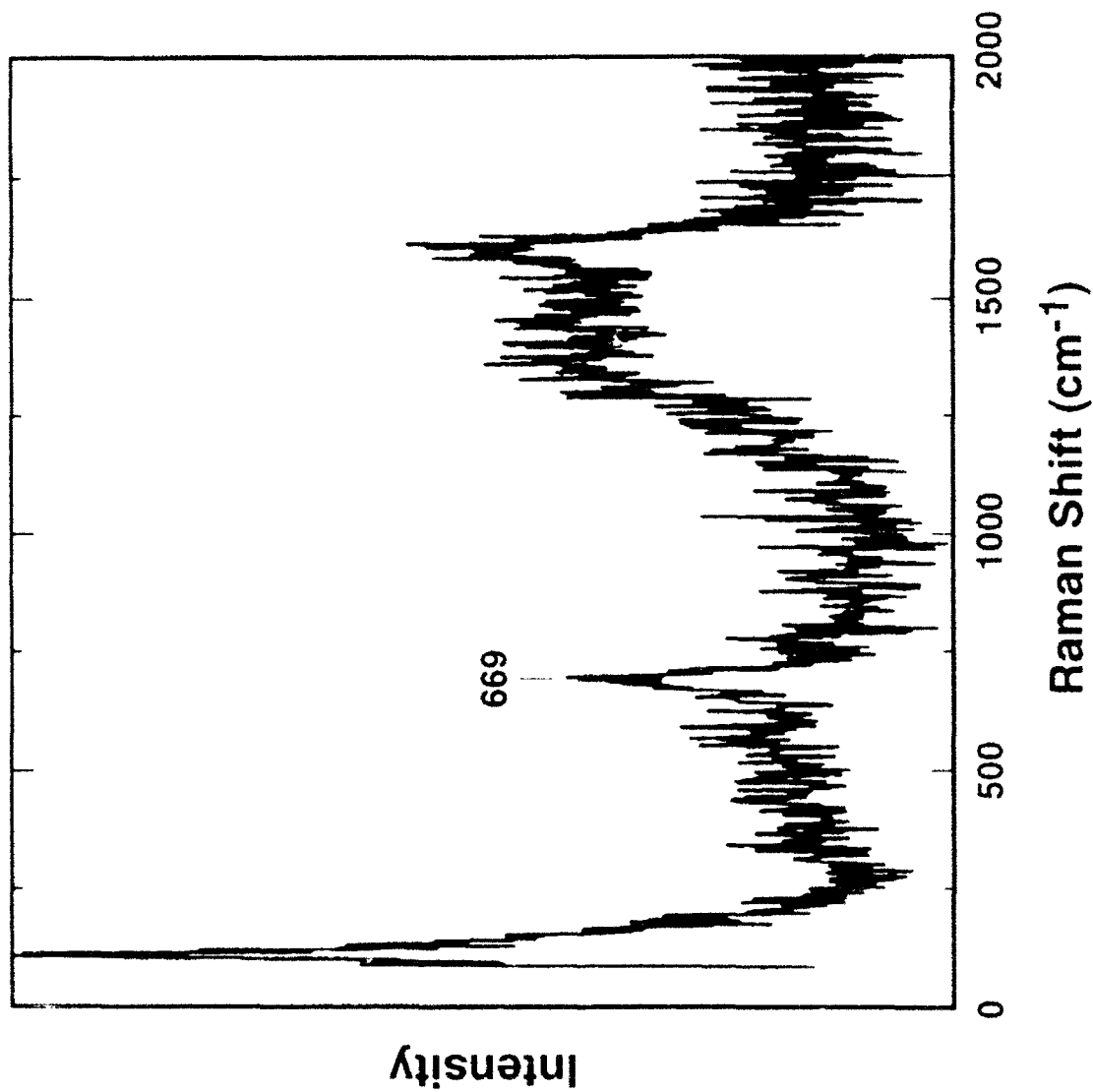


Figure 47 Green-excited (514.5 nm) Raman-format spectrum, with background fluorescence removed at 8" along Side A of tube 9/91-6, showing a Raman band due to the oxidized tube wall at 669 cm^{-1} , in addition to carbon Raman bands at 1100 cm^{-1} to 1700 cm^{-1}

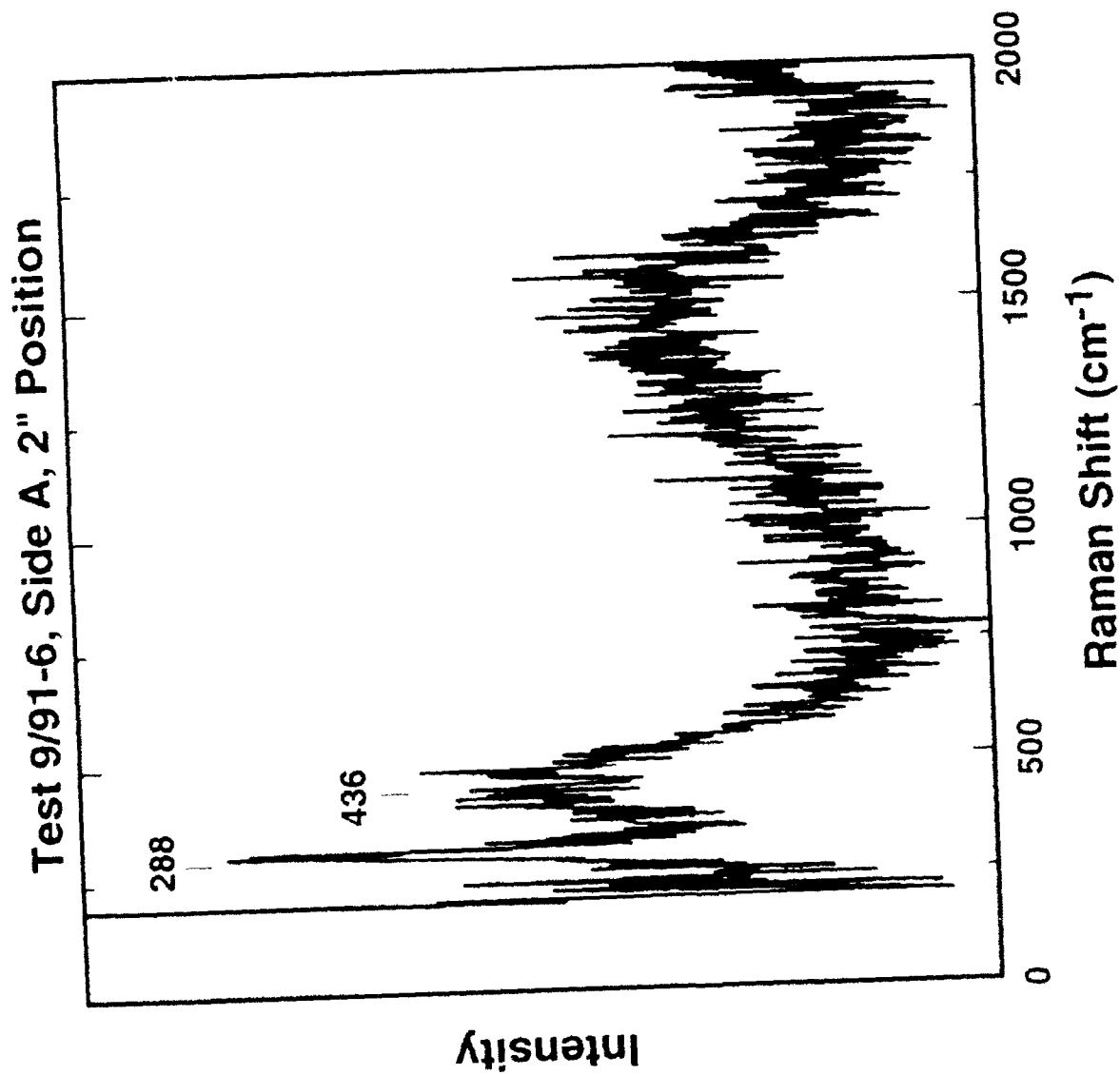


Figure 48. Green-excited (514.5 nm) Raman-format spectrum, with background fluorescence removed, at 2" along Side A of tube 9/91-6, showing a Raman band due to sulfur-containing species at 288 cm⁻¹ and 436 cm⁻¹, in addition to carbon Raman bands at 1100 cm⁻¹ to 1700 cm⁻¹.

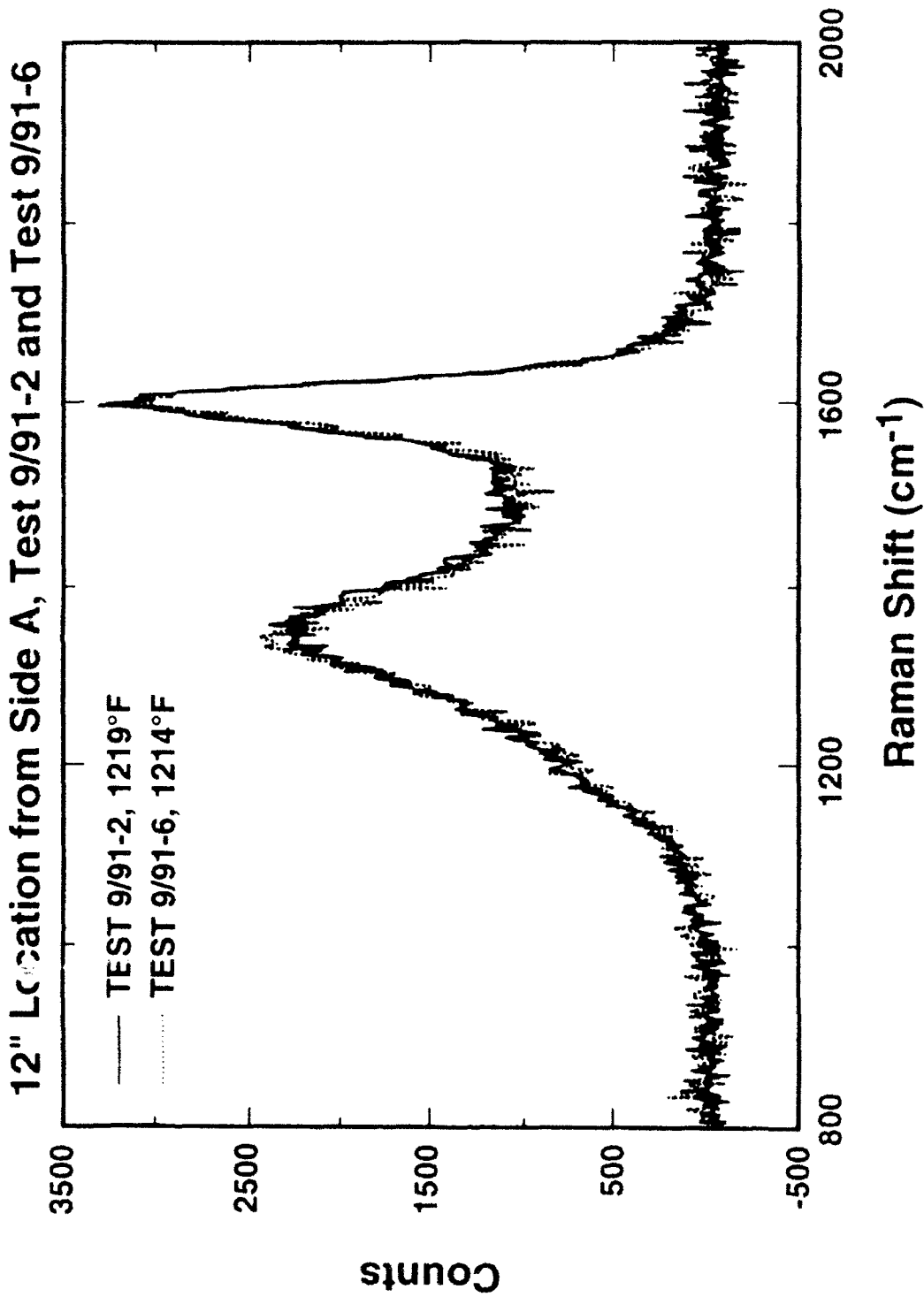


Figure 49. Green-excited (514.5 nm) Raman-format spectra, with background fluorescence removed, at 12" along Side A of tubes 9/91-2 and 9/91-6, comparing carbon Raman bands deposited from a low-sulfur fuel (9/91-2) and a high-sulfur fuel (9/91-6)

the pyrolysis events at these locations are believed to include transient effects, for example, deposition of fuel residues during cool-down after a heating cycle. At the 8-inch location deposition appears to have occurred primarily during transient events. Because of these transient effects, the carbon Raman band shapes do not reflect the measured steady-state temperatures at all locations along the tubes, and these tests cannot be used to calibrate Raman band signatures to temperature. Dr. Tim Edwards of WPAFB is carrying out tests in which the fuel is replaced by an inert gas during cool-down, thereby minimizing transient effects. While the deposition behavior of the low-sulfur (9/91-2) and high-sulfur (9/91-6, 9/91-9) fuels is qualitatively similar, some differences were noted. The low-temperature pyrolysis zones tend to be broader, distance-wise, in the tubes exposed to high-sulfur fuel, and there is more evidence for sulfur-containing residues in the tubes exposed to high-sulfur fuel. Carbon Raman bands from low-sulfur and high-sulfur fuels, at least in locations with the same steady-state temperatures and with no evidence of transient effects, are nearly indistinguishable.

We plan to continue the analysis of tube 9/91-9 to see if it follows the deposition patterns observed in tubes 9/91-2 and 9/91-6. Tubes in which transient deposition effects have been minimized will be analyzed, when received, in order to correlate Raman band signatures to steady-state temperatures. We also plan to investigate further the source of the multiple fluorescence bands.

2. Measurement of Materials Deposited on Quartz Crystal Microbalances

Quartz crystal microbalances offer the possibility of measuring the amount of the deposition on line. One concern is the absolute calibration of the microbalances. By using an external method for determining the amount of material on a microbalance, a cross check of the calibration can be obtained.

The deposits collected on three quartz micro-balances have been depth profiled using Auger electron spectroscopy and inert gas ion sputtering. Depth profiles obtained from two of these oscillators, identified as JA1FOF (10-16-91) 1-1/2 hours at 170°C and JA1COF (10-10-91) 4 hours at 170°C are shown in Figure 50. It is clear from this figure that the amount of carbon deposited on the 4-hour sample is greater than that deposited on the 1 1/2-hour sample. The fact that a carbon layer of uniform intensity is not found in the surface region of either sample (i.e. the carbon signal starts decaying at the surface) is most easily explained by a noncontinuous carbon layer; i.e., it has holes. The depth profile from the third sample, identified as JP-8 (12-23-91) 200°C, is shown in Figure 51. Note that in this case a uniform carbon layer that extends some distance into the sample is found.

In order to calibrate the depth scale, the usual method is to compare the sputter time to reach the interface of the unknown sample with the time to reach the

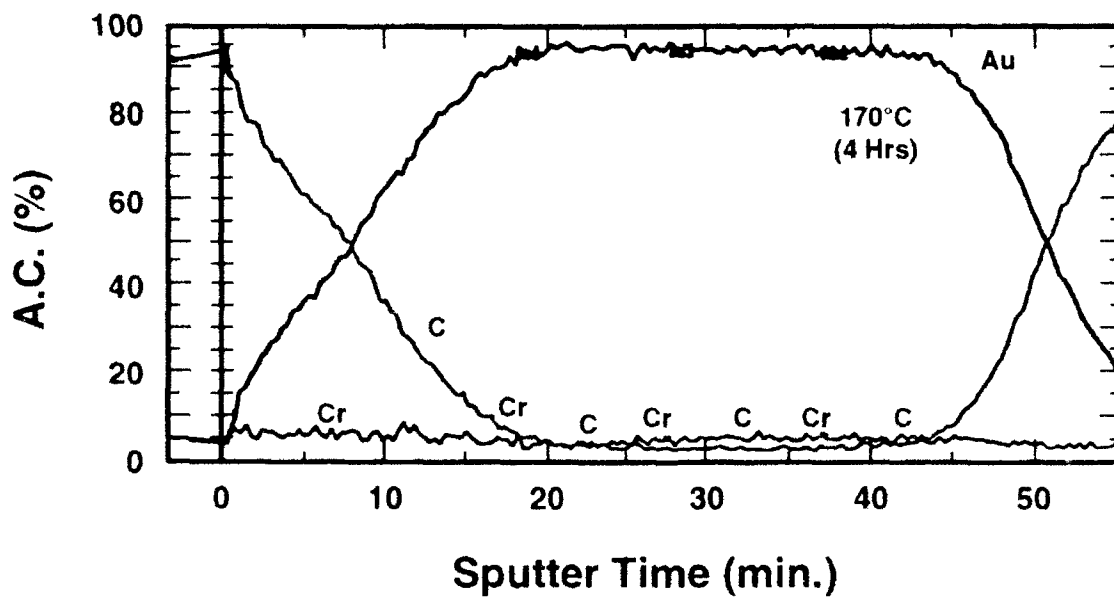
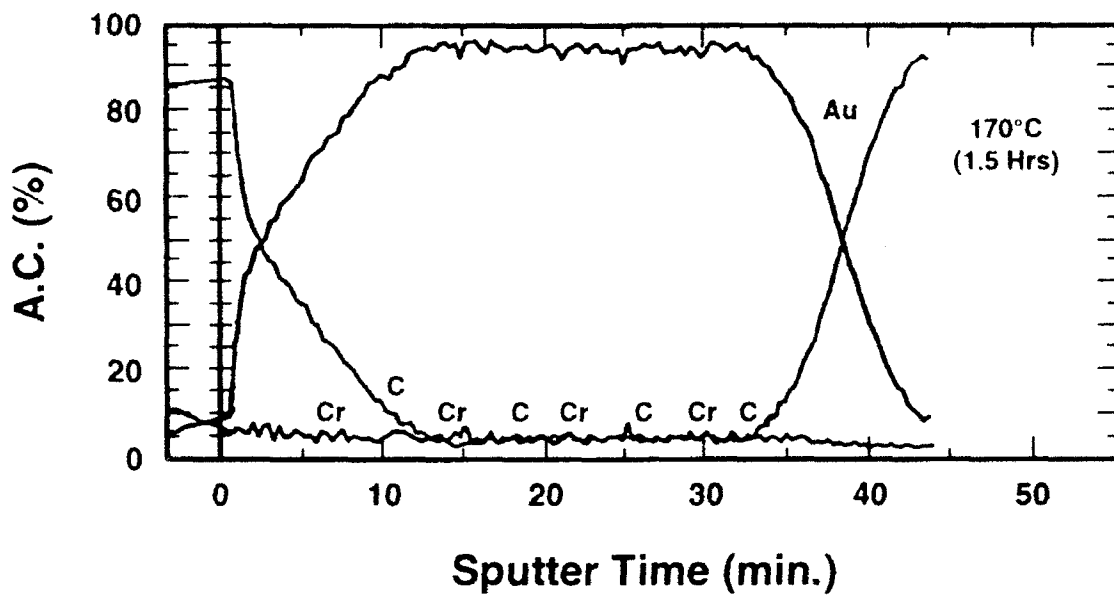


Figure 50. Auger depth profiles of deposits on quartz microbalances after 1-1/2 hour and 4 hours, respectively.

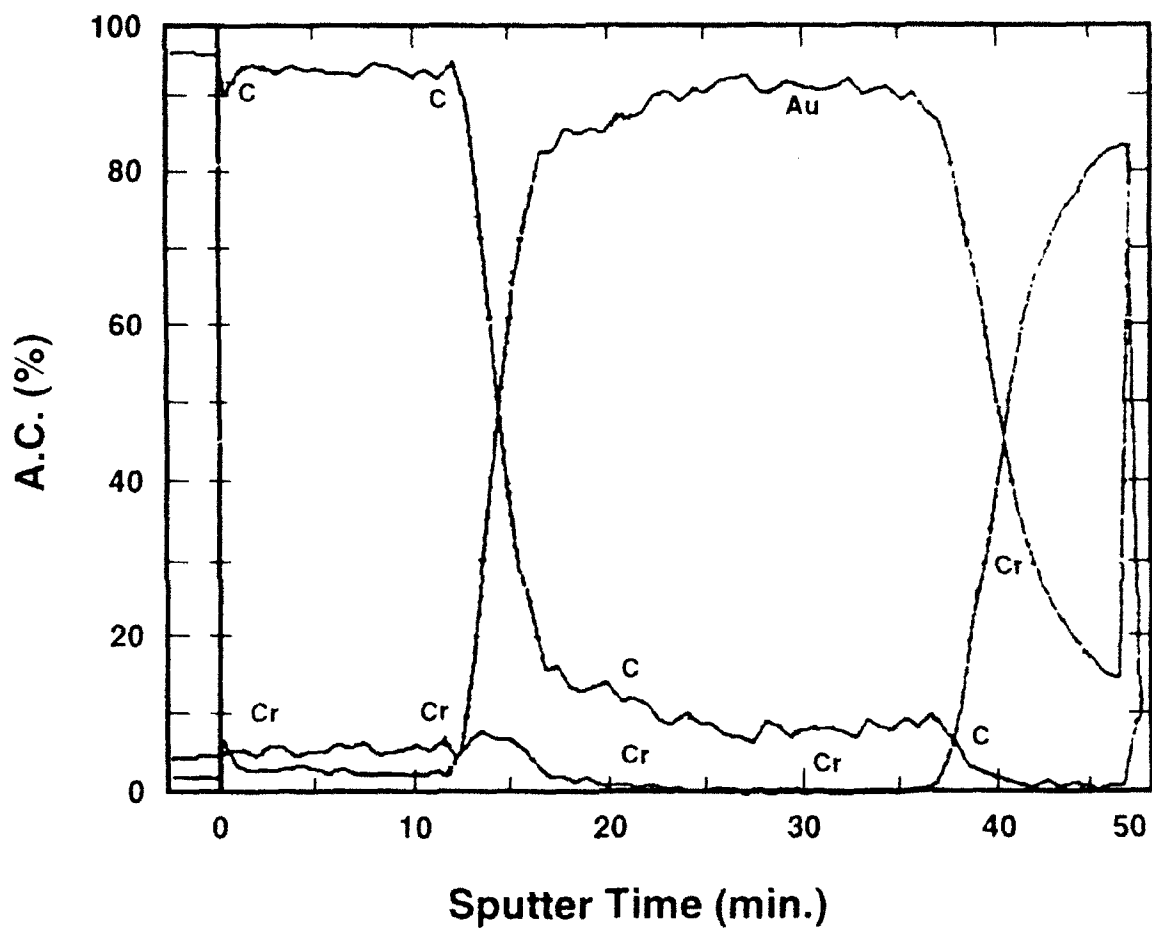


Figure 51. Auger depth profiles of the deposit on a quartz microbalance for JP-8 at 200°C.

interface of a known thickness SiO₂ sample. To determine the sputter rate difference between SiO₂ and a hydrocarbon layer, we have deposited and cured a 550 Å layer of photoresist. The comparisons of these data are shown in Figure 52. From these data we find that the hydrocarbon layer sputters at a rate of 1.3 times faster than the SiO₂ layer. Because of the availability of the SiO₂ material, all unknown sputter rates were compared to the SiO₂ and then corrected by multiplying by the 1.3 factor.

Since the carbon profiles from the quartz micro-balances shown in Figure 51 were not uniform, an "equivalent thickness" was calculated by measuring the area under the carbon profile. The results for the three samples are 650 Å, 1200 Å, and 2000 Å, respectively. These results are compared with values of 500 Å, 1300 Å, and 1700 Å, respectively, that are calculated from the measured deposition rates from the QCM tests. In those calculations, a value of 1 g/cm³ was assumed for the deposited solids. This agreement is considered a validation of the QCM data.

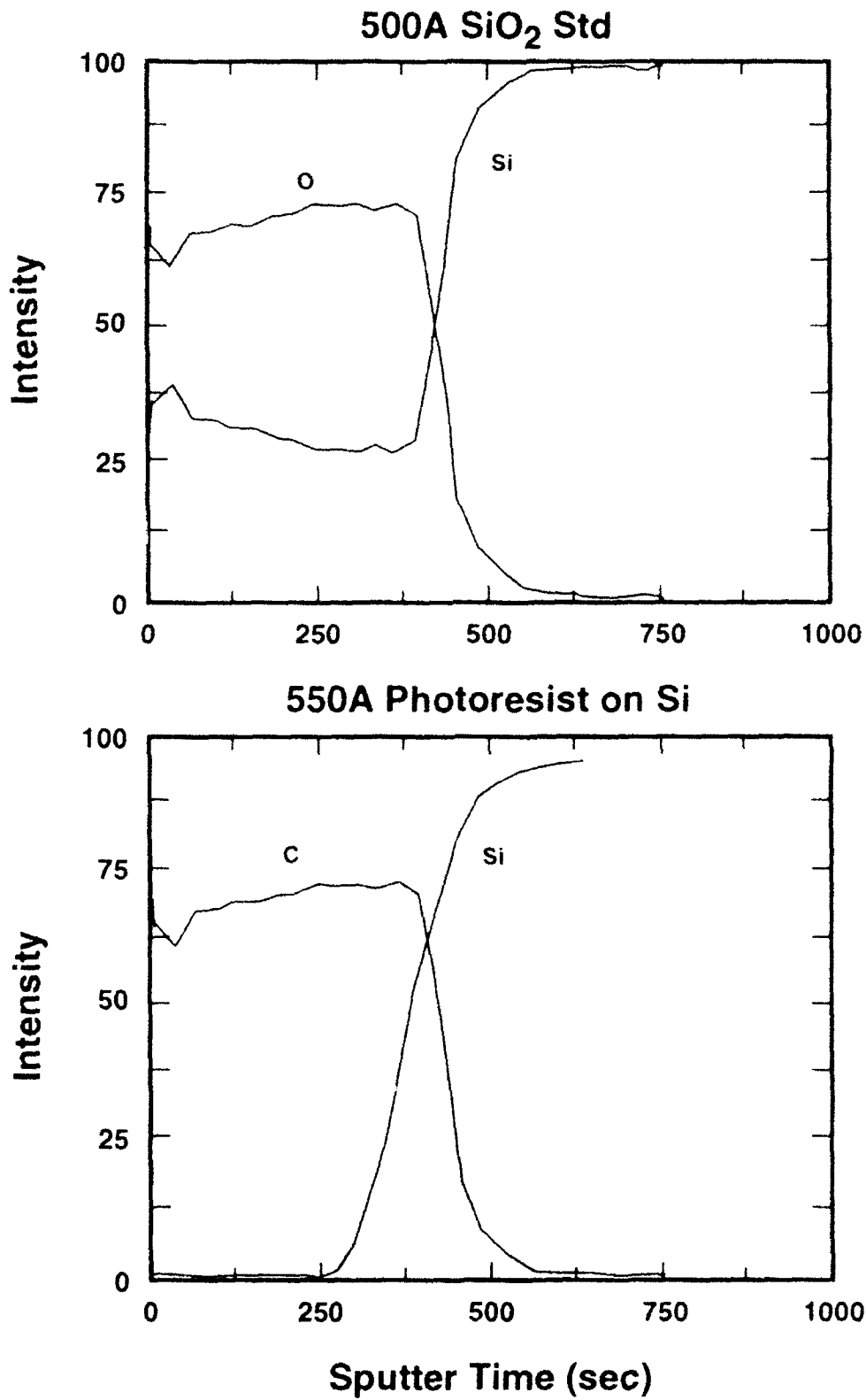


Figure 52. Auger depth profiles for 500 Å SiO₂ standard and 550 Å photoresist standard

3. CONCLUSIONS

The work performed during the past year focused on continued development and testing of the Quartz Crystal Microbalance system for monitoring *in situ* mass deposition and the Photon Correlation Spectroscopy system for *in situ* monitoring of the formation and growth of particles during fuel thermal stressing. Solids characterization studies also were performed to support the QCM tests and to look at heated tubes provided by Wright Laboratory in continuing efforts to understand mechanisms and characteristics of solids deposition. Specific conclusions are detailed below.

1. QCM System

The QCM system was improved in both flexibility and cost. The current system can operate at elevated pressures and temperatures and can be assembled for several thousand dollars. Technology transfer of this technique to program participants has been initiated.

The QCM data on deposition rates has been confirmed by independent testing using ion-beam sputtering and Auger electron spectroscopy to measure the actual depth of solid deposits on the quartz wafers and comparing these values to values from the QCM data.

Both JP-8 and Jet A fuels have been tested over a temperature range of approximately 160°C to 200°C. Activation energy values have been determined. Additionally, viscosity values were measured as a function of temperature and validated by comparison with literature values.

2. Photon Correlation Spectroscopy System

The PCS system was improved by establishing temperature uniformity with the test cell and improving system software.

Calibration and validation tests using particle standards were completed.

Mie scattering capability was added to the system to allow determination of particle diameters larger than approximately 300 nm.

Tests performed on jet fuel samples showed that:

- Filtering prior to stressing can significantly affect fuel thermal stability;
- Particle diameters measured at room temperature are larger than those measured at elevated temperatures, showing the need for real-time measurements;
- Particle formation appears to accelerate over a narrow temperature range;
- Mean particle sizes increase monotonically with temperature and time; and

- Particles are formed at temperatures as low as 120°C, considerably cooler than had previously been hypothesized.

3. Solid Characterization Studies

Tests on the heated tubes supplied by Wright Laboratory showed that:

- The sulfur distribution as a function of position along the test tubes correlates with the carbon distribution;
- In the temperature region around 1000°F (528°C), the sulfur and oxygen content of the deposits for the high-sulfur fuel are on the order of 1%;
- For a given fuel, varying the time of the experiment varies the amount of the deposit but does not vary the appearance (solid in the phase transition region, vapor phase growth in the high temperature region);
- The vapor phase growth occurs for the high-sulfur fuel at temperatures of approximately 1000°F;
- For a given time and temperature, the low-sulfur fuel has significantly less material deposited and the form of the deposit is different;
- Qualitatively similar patterns of deposition of jet fuel were found to be present on the different tubes;
- Variation of carbon Raman band signatures with steady-state temperature was observed, confirming that this technique can be used to determine the maximum temperature at which carbon was deposited;
- Sulfur-containing deposits were identified; and
- The method of cool-down can significantly affect deposit formation.

Future work in the program will focus on 1) continued development of the QCM system for flowing systems to determine the feasibility of using the sensor as an in-line diagnostic device in an aviation fuel system, 2) data collection using both the QCM and PCS systems, and 3) subsequent model development for the physico-chemical phenomena associated with fuel thermal degradation and deposition.

BIBLIOGRAPHY

- Berne, B. J. and Pecora, R., Dynamic Light Scattering with Applications to Chemistry, Biology and Physics, (Wiley, New York), Chapter 5, 1976.
- Bohren, C. F. and Huffman, D. R., Absorption and Scattering of Light by Small Particles, (Wiley-Interscience, New York, 1983), pp. 477-482.
- Bolshakov, G. F., "The Physico-Chemical Principles of the Formation of Deposits in Jet Fuels," Wright-Patterson AFB Report, AD-781 164, April 1974.
- Bott, S. E., "Submicron Particle Sizing by Photon Correlation Spectroscopy: Use of Multiple Angle Detection," in Particle Size Distribution - Assessment and Characterization, ACS Symposium Series 332, T. Provder, Ed., 1987, pp. 74-88.
- CRC (Coordinating Research Council, Inc.), Handbook of Aviation Fuel Properties, Report No. 530, 1988.
- Edwards, T., "Deposition During Vaporization of Jet Fuel in a Heated Tube," AIAA 92-0687, 1992.
- Hazlett, R. N., Thermal Oxidation Stability of Aviation Turbine Fuels, (ASTM PCN 31-001092-12, Philadelphia PA, 1991), pp. 55-57.
- Klavetter, E., Trott, W., O'Hern, T., and Martin, S., Advanced Thermally Stable, Jet Fuels Development Program Annual Report, Volume 1-Model and Experiment System Development, WL-TR-91-2099, January 1992, p. 35.
- Oliver, C. J., "Correlation Techniques," in Photon Correlation and Light Beating Spectroscopy, H. Z. Cummins and E. R. Pike, Eds. (Plenum, New York, 1974), pp. 151-223.
- Parsley, M., 1991, The Hallcrest Handbook of Thermochromic Liquid Crystal Technology, Hallcrest Products Inc., Glenview, Illinois.
- Russo, P., Guo, K., and Delong, L., "A New Look at Distribution Analysis of Dynamic Light Scattering Data, Using Only a Microcomputer," Society of Plastics Engineers, 46th Annual Technical Conference Proceedings, 1988, pp. 983-985.
- Trott, W. M., O'Hern, T. J., and Klavetter, E. A., "In Situ Measurement of Particle Formation in Heated Jet Fuels - A New Application of Photon Correlation Spectroscopy," Proceedings of American Chemical Society Division of Petroleum Chemistry, Symposium on Structure of Jet Fuels, April 1992, 442-450.

Wagner, W., Rauch, F., Haubner, R., and Lux, B., Thin Solid Films, **207**, 1992, p. 24.

Weiner, B. B., "Particle Sizing Using Photon Correlation Spectroscopy," in Modern Methods of Particle Size Analysis, H. G. Barth, Ed. (Wiley, New York, 1984), pp. 93-116.